ISSN: 2322-4924

Ministry of Science, Research and Technology

Damghan University

Astronomical Society of Iran

IJAA

Iranian Journal of Astronomy and Astrophysics

Volume 3, Number 2, 2016

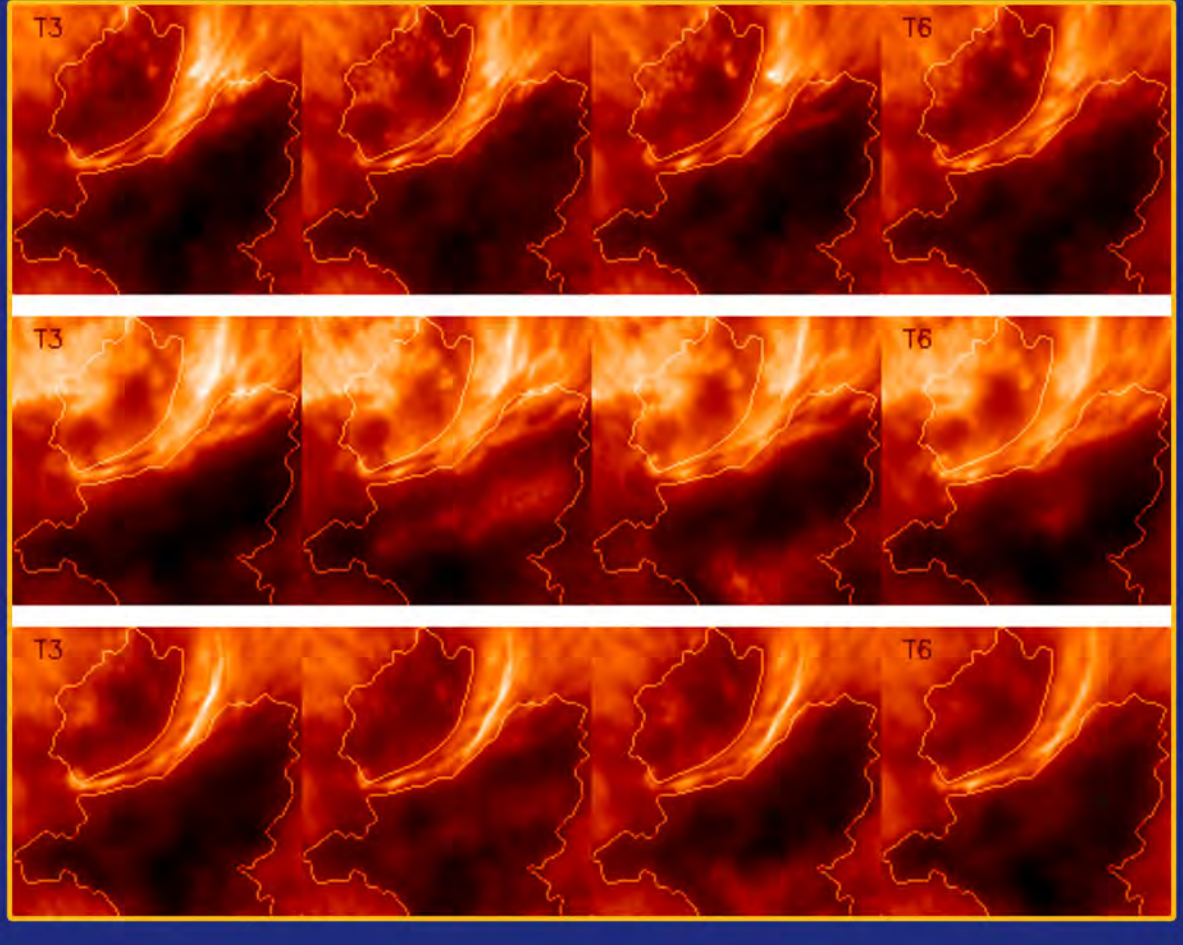

Successive intensity filtergrams of the Ca II 854.2 nm line (sunspot umbra; NOAA 11471) recorded with CRISP at SST. Top: near red-wing, Middle: line core, Bottom: near blue-wing.
(H. Hamedivafa et al, IJAA, 3, 1, 2016)

Ministry of Science, Research and Technology

Damghan University

Astronomical Society of Iran

Iranian Journal of Astronomy and Astrophysics (IJAA)

Vol. 3, No. 2, 2016

This journal is the collaborative results of Damghan University and the Astronomical Society of Iran, and it is published twice per year.

Head office: Damghan University, Damghan, Iran
Postal Code: 36716-41167
Tel-fax: +98-23-35220236
Online submission: http://ijaa.du.ac.ir/
E-mail: ijaa@du.ac.ir

Iranian Journal of Astronomy and Astrophysics
(IJAA)

Vol. 3, No. 2, 2016

Astronomical Society of Iran
Damghan University

Iranian Journal of Astronomy and Astrophysics

(IJAA)

Astronomical Society of Iran
Damghan University

Contents

Volume 3, Number 2, 2016

Iranian Journal of Astronomy and Astrophysics
Vol. 3, No. 2, Autumn 2016

Iranian Journal of Astronomy and Astrophysics

Spin and Isospin Asymmetry, Equation of State and Neutron Stars

Mohsen Bigdeli · Nariman Roohi · Mina Zamani
Department of Physics, University of Zanjan, P.O. Box 45195-313, Zanjan, Iran

Abstract. In the present work, we have obtained the equation of state for neutron star matter considering the influence of the ferromagnetic and antiferromagnetic spin state. We have also investigated the structure of neutron stars. According to our results, the spin asymmetry stiffens the equation of state and leads to high mass for the neutron star.

Keywords: Neutron stars, Spin asymmetry, Equation of state

1 Introduction

Neutron stars are hyper-dense and magnetized laboratories for investigating strange phenomena in the nuclear and particle physics. Pulsars and magnetars are two kinds of neutron stars with strong surface magnetic field. Actually the exact origin of this magnetic field is not yet known. In the interior of magnetars, the magnetic field strength may be even larger according to virial theorem [6] and such strong field may cause spin asymmetry. The occurrence of such strange phenomena can affect the equation of state (EOS) of neutron star matter. Theoretically, the equation of state has been applied to determine the maximum mass of a neutron star which should be in agreement with the precise observations. The accurate measurement of neutron star mass $M = 1.97 \pm 0.04 M_{\odot}$ in the system PSR J1614-2230 was one of the most important development in observational data [9]. This precise measurement is based on Shapiro delay in neutron star-white dwarf binary [12]. Another well-measured massive neutron star is PSR J0348+0432, with mass about $M = 2.01 \pm 0.04 M_{\odot}$ [1]. Next, there is an evidence that the black widow pulsar PSR B1957+20 might have even larger masses approximately $M_{PSR} = 2.4 M_{\odot}$ [17]; however, one have to consider the uncertainties in this mass estimation. Finally, the largest mass $2.1 M_{\odot} \leq M_{NS} \leq 2.7 M_{\odot}$ has been given for the gamma-ray black widow pulsar PSR J1311-3430 by simple heated light curve fits [16]. These massive neutron stars require the equation of state of the system to be rather stiff. Therefore, theoretical approaches should confirm these observational data.

Recently, several studies used different theoretical approaches showed the stiff EOS for the neutron star matter. Gandolfi et al. [10] have used quantum Monte Carlo techniques and calculated the equation of state of neutron star matter with realistic two- and three-nucleon interactions. Their calculation resulted $M_{max} < 2.2 M_{\odot}$ for neutron star mass. They have also used Auxiliary Field Diffusion Monte Carlo technique by incorporating semi-phenomenological Hamiltonian including a realistic two-body interaction and many-body forces [11]. They found the maximum mass of neutron star lies in the range 2.2-2.5 times of solar mass. Some other attempts by Partha Roy Chowdhury showed the rotating star mass is around $(1.93\text{-}1.95) M_{\odot}$ [7] . They have applied a pure nucleonic equation of state for neutron star matter. Shen et al. [14] have constructed a new equation of state for a wide range of temperatures, densities and proton fractions to be used in astrophysical

simulations of neutron stars. They have predicted that the maximum mass of neutron star is about $2.77M_{\odot}$ with a radius of about 13.3 km. Sun et al. [15] have investigated neutron star structure using EOS which has provided by density dependent relativistic Hartree-Fock theory. Their results showed that maximum mass of neutron stars lies in the range $(2.45-2.49)M_{\odot}$. More recently, we gained $M_{NS}=1.991M_{\odot}$ by applying the Lowest Order Constrained Variational (LOCV) method and using UV_{14}+TNI potential [4].

In this article, we investigate some physical properties of polarized neutron star matter using the LOCV method and the AV_{18} potential. This modern equation of state is derived from an accurate many-body calculation and is based on the cluster expansion of the energy functional. Moreover, we obtain the particles abundance, equation of state and the structure of neutron stars. Finally, we compare our results by experimental data.

2 Formalism

We assume the neutron star matter as a charge neutral infinite system that is a mixture of leptons and interacting nucleons. The energy density of this system can be obtained as follows,

$$\varepsilon=\varepsilon_N+\varepsilon_l, \tag{1}$$

where $\varepsilon_N(\varepsilon_l)$ is the energy density of nucleons (leptons). In the following, we determine these energy densities in more details.

2.1 Energy density of leptons

The energy density of leptons, which are considered as noninteracting Fermi gas, is given by,

$$\varepsilon_{lep} \;=\; \sum_{l=e,\ \mu}\ \sum_{k\le k_l^F}(m_l^2c^4+\hbar^2c^2k^2)^{1/2}\ . \tag{2}$$

In this equation, $k_l^F=(6\pi^2\rho_l/\nu)^{1/3}$ is Fermi momentum of leptons and ν is degeneracy. For fully spin polarized matter, degeneracy is $\nu=1$.

2.2 Energy density of spin polarized nucleon matter

The nucleonic part of neutron star matter is composed of neutrons and protons with densities ρ_n and ρ_p, respectively. The total number density of the system is

$$\begin{aligned}\rho &= \rho_p+\rho_n,\\ &= (\rho_p^{(\uparrow)}+\rho_p^{(\downarrow)})+(\rho_n^{(\uparrow)}+\rho_n^{(\downarrow)}).\end{aligned} \tag{3}$$

The labels $(\uparrow)$ and $(\downarrow)$ are used for spin-up and spin-down nucleons, respectively. The following parameters can be used to identify a given spin-polarized state for the asymmetric nuclear matter,

$$\delta_p=\frac{\rho_p^{(\uparrow)}-\rho_p^{(\downarrow)}}{\rho_p},\quad \delta_n=\frac{\rho_n^{(\uparrow)}-\rho_n^{(\downarrow)}}{\rho_n} \tag{4}$$

δ_p and δ_n are proton and neutron spin asymmetry parameters, respectively. In the fully ferromagnetic (FM) polarized nuclear matter, spin of all neutrons and protons are parallel,

$\delta_n = \delta_p = 1.0$, and in the antiferromagnetic (AFM) spin state, we have $\delta_n = \pm 1.0, \delta_p = \mp 1.0$. The asymmetry parameter which describes the isospin asymmetry of the system is defined as,

$$\beta = \frac{\rho_n - \rho_p}{\rho} = 1 - 2x_p \tag{5}$$

where $x_p = \rho_p/\rho$ is the proton fraction. Pure neutron matter is totally an asymmetric nuclear matter with $x_p = 0$, while for the symmetric nuclear matter $x_p = 1/2$. The energy density of spin-polarized asymmetrical nuclear matter, ε_{nucl} can be determined as,

$$\varepsilon_N = \rho(E + m), \tag{6}$$

where $m = 938.92$ MeV is the nucleon mass and E is the total energy per nucleon which is calculated by using the LOCV method as follows.

We adopt a trial many-body wave function of the form

$$\psi = \mathcal{F}\phi, \tag{7}$$

where ϕ is the uncorrelated ground state wave function of A independent nucleons (simply the Slater determinant of the plane waves) and $\mathcal{F} = \mathcal{F}(1 \cdots A)$ is an appropriate A-body correlation operator which can be replaced by a Jastrow form i.e.,

$$\mathcal{F} = \mathcal{S} \prod_{i>j} f(ij), \tag{8}$$

in which $\mathcal{S}$ is a symmetrizing operator. Now, we consider the cluster expansion of the energy functional up to the two-body term [8],

$$E_{nuc}([f]) = \frac{1}{A} \frac{\langle \psi | H | \psi \rangle}{\langle \psi | \psi \rangle} = E_1 + E_2 \cdot \tag{9}$$

The one-body term E_1 for an asymmetrical nuclear matter is

$$E_1 = \sum_{\tau=n,p} \sum_{\sigma=\uparrow,\downarrow} \sum_{k \le k_F{}_\tau^\sigma} \frac{\hbar^2 k^2}{2m_\tau}, \tag{10}$$

where $k_F{}_\tau^\sigma = (6\pi^2 \rho_\tau^\sigma)^{1/3}$ is the fermi momentum of each component of spin-polarized asymmetric nuclear matter. The two-body energy E_2 is

$$E_2 \quad = \quad \frac{1}{2A} \sum_{ij} \langle ij \, | \nu(12) | \, ij - ji \rangle, \tag{11}$$

where

$$\nu(12) = -\frac{\hbar^2}{2m} [f(12), [\nabla_{12}^2, f(12)]] + f(12) V(12) f(12). \tag{12}$$

Here, $f(12)$ and $V(12)$ are the two-body correlation and potential. In our calculations, we use the AV_{18} two-body potentials [20]. Now, we minimize the two-body energy, Eq. (11), with respect to the variations in the correlation functions $f^{(k)}$, but subject to the normalization constraint [13, 2],

$$\frac{1}{A} \sum_{ij} \langle ij \, | h^2_{S_z,T_z} - f^2(12) | \, ij \rangle_a = 0, \tag{13}$$

where in the case of spin polarized asymmetrical nuclear matter, the Pauli function $h_{S_z,T_z}(r)$ is as follows,

$$h_{S_z,T_z}(r) = \begin{cases} \left[1 - 9\left(\frac{J_1^2(k_{F_\tau}^{(\sigma)}r)}{k_{F_\tau}^{(\sigma)}r}\right)^2\right]^{-1/2} & S_z = \pm 1, T_z = \pm 1 \\ 1 & otherwise \end{cases} \quad (14)$$

From the minimization of the two-body cluster energy, we get a set of coupled and uncoupled Euler-Lagrange differential equations [5]. We can calculate the correlation functions by numerically solving these differential equations and then, using these correlation functions, the two body energy is obtained. Finally, we can compute the energy of the system.

2.3 URCA processes

Now, we investigate direct URCA processes in the spin polarized neutron star matter. In fully polarized ferromagnetic spin state, the nature of chemical equilibrium is mainly dominated by the following weak interaction processes,

$$\begin{aligned} n(\uparrow) &\rightarrow p(\uparrow) + l(\uparrow) + \bar{\nu}_l(\downarrow) \\ p(\uparrow) + l(\uparrow) &\rightarrow n(\uparrow) + \nu_l(\downarrow) \end{aligned} \quad (15)$$

Here, ν_l stands for the leptons neutrinos which leave the system without delay. In this case, the β-equilibrium conditions and charge neutrality of neutron star matter impose the following coupled constraints on our calculations,

$$\begin{aligned} \mu_e(\uparrow) = \mu_\mu(\uparrow) &= \mu_n(\uparrow) - \mu_p(\uparrow) \\ &= 4(1-2x_p)S_2(\rho, \delta_n = \delta_p = 1) + 8(1-2x_p)^3 S_4(\rho, \delta_n = \delta_p = 1) \end{aligned} \quad (16)$$

$$\rho_p(\uparrow) = \rho_e(\uparrow) + \rho_\mu(\uparrow) \quad (17)$$

where S_2 and S_4 are given by [3],

$$\begin{aligned} S_2(\rho, \delta_n, \delta_p) &= \frac{1}{2}\left(\frac{\partial^2 E(\rho, \delta_n, \delta_p)}{\partial \beta^2}\right)_{\beta=0} \\ S_4(\rho, \delta_n, \delta_p) &= \frac{1}{24}\left(\frac{\partial^4 E(\rho, \delta_n, \delta_p)}{\partial \beta^4}\right)_{\beta=0}. \end{aligned} \quad (18)$$

Similarly, The β-equilibrium and the charge neutrality conditions for fully anti-ferromagnetic spin polarized are,

$$\begin{aligned} \mu_e(\downarrow) = \mu_\mu(\downarrow) &= \mu_n(\downarrow) - \mu_p(\uparrow) \\ &= 4(1-2x_p)S_2(\rho, \delta_n = -\delta_p = 1) + 8(1-2x_p)^3 S_4(\rho, \delta_n = -\delta_p = 1) \end{aligned} \quad (19)$$

$$\rho_p(\uparrow) = \rho_e(\downarrow) + \rho_\mu(\downarrow). \quad (20)$$

We find the abundance of the particles by solving the coupled equations of charge neutrality and β-equilibrium conditions. Finally, we calculate the total energy and the equation of state of the neutron star matter.

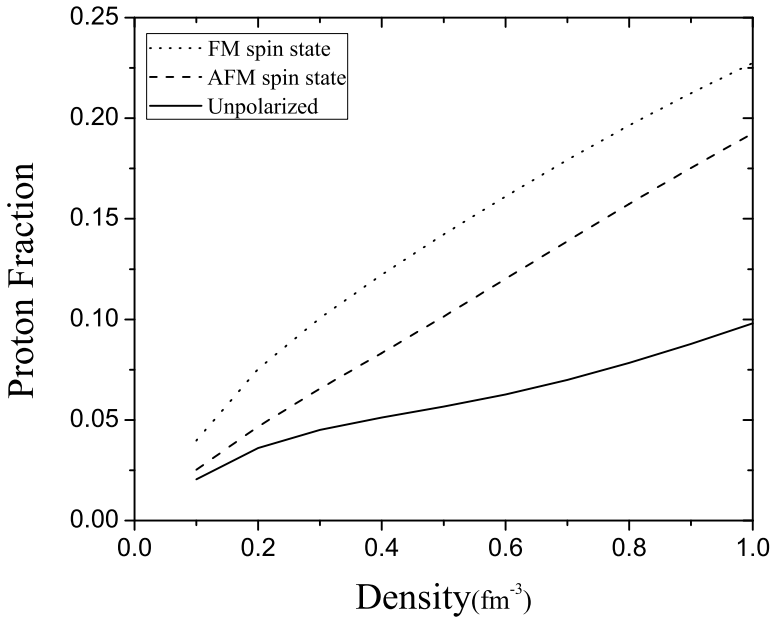

Figure 1: The proton fraction in the neutron star matter for different spin states.

3 Results and discussion

Figure 1 shows the proton fraction, x_p, versus the baryon number density, ρ, for unpolarized, ferromagnetic and antiferromagnetic spin state. It can be seen from this figure that the abundance of protons is an increasing function of both spin polarization and baryon density. Therefore, we can conclude that nuclear portion of spin polarized neutron star matter tend to be symmetric matter. It is also seen that for a given density, the highest value of proton fraction is gained for the ferromagnetic spin state.

In Figs. 2 and 3, we have presented the energy density, ε, and pressure of neutron star matter as a function of baryon number density, ρ, for unpolarized, ferromagnetic and antiferromagnetic spin state, respectively. Here, we have not considered the contribution of magnetic field. In these figures, we have also plotted the energy density and pressure of the fully polarized neutron matter (PNM), i.e. $\beta = 1, \delta_n = 1$. As we can see, the energy density and pressure increase by increasing both of spin and isospin asymmetry parameters. we have concluded that the spontaneous phase transition to ferromagnetic and antiferromanetic spin state does not occur. If such a transition existed, a crossing of the energies of different polarizations would have been observed at some density, indicating that the ground state of the system would be ferromagnetic or antiferromagnetic from that density on. As can be seen in these figures,there is no sign of such a crossing. Our results can be compared with those of Vidana's [18, 19]. Also, it is clear from these figures that the EOS of spin polarized neutron star matter is stiffer than unpolarized matter.

Now, we can investigate the structure of neutron star by using the equation of state and integrating the TOV equation. A summary of our results for the maximum mass, radius, central energy density and central baryon density of neutron star predicted from different

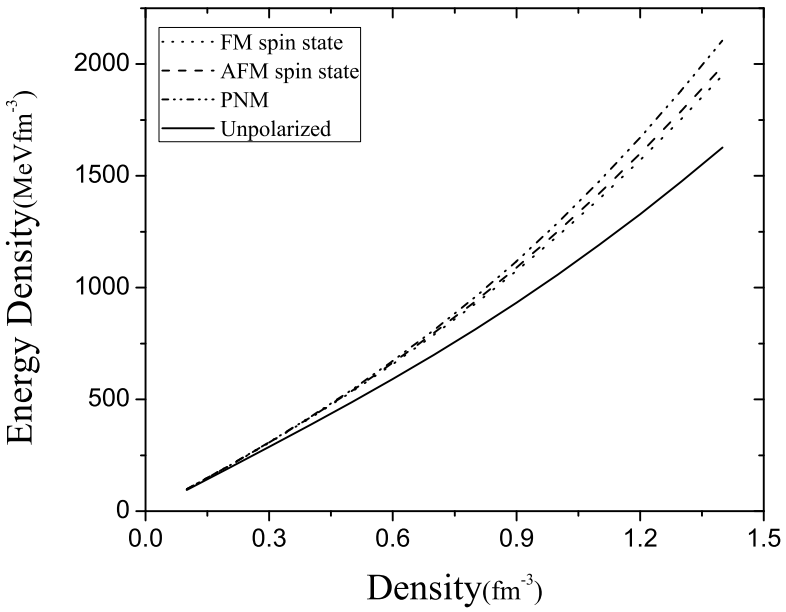

Figure 2: The energy density of neutron star matter versus baryon number density for for different spin states and fully polarized neutron matter.

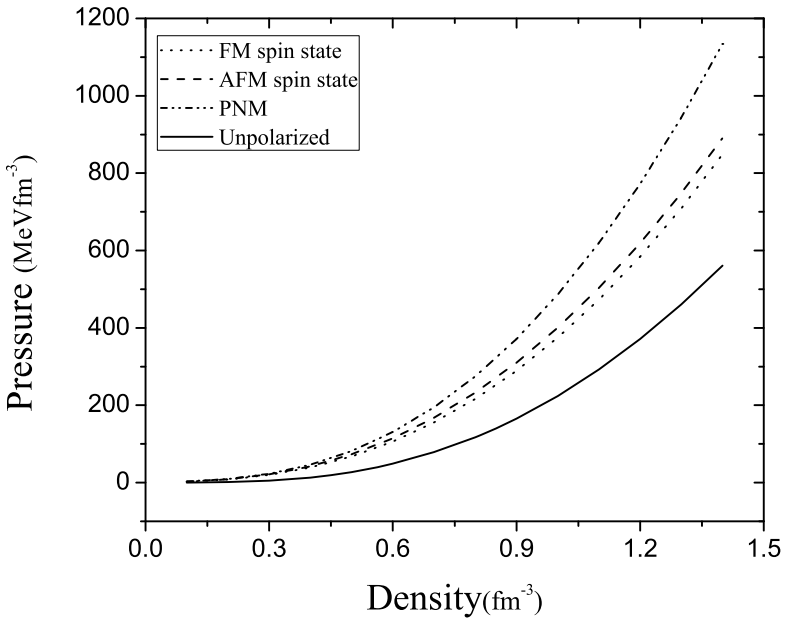

Figure 3: As a Fig. 2 but for pressure.

Table 1: Maximum mass, radius, central energy density and central baryon density of neutron star. The gravitational mass is given in solar mass ($M_\odot$).

EOS	M_{max}	R (km)	ϵ_c (10^{14} g/cm^3)	ρ_c (fm^{-3})
NSM [12]	1.63	8.04	-	-
FM-NSM	1.83	10.24	30.28	1.27
AFM-NSM	1.88	10.54	28.67	1.2
PNM	1.99	10.8	27.14	1.13

equations of state is given in table 1. We can conclude from this table that the more asymmetric is the neutron star matter, the higher maximum mass.

4 Summary and Conclusions

The purpose of this paper is investigating the influence of spin polarization on the equation of state of neutron star matter and, consequently, the structure of neutron star. We have used the lowest order constrained variational (LOCV) method by employing the AV_{18} potentials for nucleon-nucleon interaction. We conclude that the equation of state become stiffer by considering spin polarization, and it yields to high maximum mass for neutron stars.

Acknowledgment

We wish to thank Research Councils of the University of Zanjan.

References

[1] Antoniadis, J. & et al. 2013, Science, 340, 448

[2] Bigdeli, M. 2010, Phys. Rev. C, 82, 054312

[3] Bigdeli, M. 2013, Int. J. Mod. Phys. E, 22, 1350054

[4] Bigdeli, M., & Elyasi, S. 2015, Eur. Phys. J. A, 51, 38

[5] Bordbar, G. H., & Modarres, M. 1998, Phys. Rev. C, 57, 714

[6] Chandrasekhar, S., & Fermi, E. 1953, ApJ, 118, 116

[7] Chowdhury, P. R. 2010, PoS NICXI, 175

[8] Clark, J. W., & Chao, N. C. 1969, Lett. Nuovo Cimento, 2, 185

[9] Demorest, P. B., Pennucci, T., Ransom, S. M., Roberts, M. S. E., & Hessels, J. W. T. 2010, Nature, 467, 1081

[10] Gandolfi, S., Carlson, J., & Sanjay Reddy 2012, Phys. Rev. C, 85, 032801

[11] Gandolfi, S., Yu. Illarionov, A., Fantoni, S., Miller, J. C., Pederiva, F., & Schmidt, K. E. 2010, MNRAS, 404, 35

[12] Lee, CH. 2012, EPJ Web of Conferences, 20, 04002

[13] Owen, J. C., Bishop, R. F., & Irvine, J. M. 1977, Nucl. Phys. A, 277, 45

[14] Shen, G., Horowitz, C. J., & Teige, S. 2011, Phys. Rev. C, 83, 035802

[15] Sun, B. Y., Long, W. H., Meng, J., & Lombardo, U. 2008, Phys. Rev. C, 78, 065805

[16] Romani, R. W., Filippenko, A. V., Silverman, J. M., Bradley Cenko, S., Greiner, J., Rau, A., Elliott, J., & Pletsch, H. J. 2012, ApJL, 760, 36

[17] van Kerkwijk, M. H., Breton, R. P., & Kulkarni, S. R. 2011, ApJ, 728, 95

[18] Vidana, I., & Bombaci, I. 2002, Phys. Rev. C, 66, 045801

[19] Vidana, I., Polls, A. & Ramos, A. 2002, Phys. Rev. C, 65, 035804

[20] Wiringa, R. B., Stoks, V. G. J., & Schiavilla, R. 1995, Phys. Rev. C, 51, 38

Iranian Journal of Astronomy and Astrophysics
Vol. 3, No. 2, Autumn 2016

Iranian Journal of Astronomy and Astrophysics

Structure Formation and Generalized Second Law of Thermodynamics in Some Viable $f(R)$-gravity Models

S. Asadzadeh · M.S. Khaledian · K. Karami
Department of Physics, University of Kurdistan, Pasdaran Street, Sanandaj, Iran;
email: KKarami@uok.ac.ir

Abstract. We investigate the growth of matter density perturbations as well as the generalized second law (GSL) of thermodynamics in the framework of $f(R)$-gravity. We consider a spatially flat FRW universe filled with the pressureless matter and radiation which is enclosed by the dynamical apparent horizon with the Hawking temperature. For some viable $f(R)$ models containing the Starobinsky, Hu-Sawicki, Exponential, Tsujikawa and AB models, we first explore numerically the evolution of some cosmological parameters like the Hubble parameter, the Ricci scalar, the deceleration parameter, the density parameters and the equation of state parameters. Then, we examine the validity of GSL and obtain the growth factor of structure formation. We find that for the aforementioned models, the GSL is satisfied from the early times to the present epoch. But in the farther future, the GSL for all models is violated. Our numerical results also show that for all models, the growth factor for larger structures, like the ΛCDM model, fit the data very well.

Keywords: Modified theories of gravity, Dark energy

1 Introduction

The observed accelerated expansion of the universe, as evidenced by a host of cosmological data such as supernovae Ia (SNeIa) [1], cosmic microwave background (CMB) [2, 4], large scale structure (LSS) [5], came as a great surprise to cosmologists. The present accelerated phase of the universe expansion reveals new physics missing from our universe's picture, and it constitutes the fundamental key to understand the fate of the universe. There are two representative approaches to explain the current acceleration of the universe. One is to introduce "dark energy" (DE) [8] in the framework of general relativity (GR). The other is to consider a theory of modified gravity (MG), such as $f(R)$ gravity, in which the Einstein-Hilbert action in GR is generalized from the Ricci scalar R to an arbitrary function of the Ricci scalar [12]. Here, we will focus on the later approach. In [15], it was shown that a $f(R)$ model with negative and positive powers of Ricci curvature scalar R can naturally combine the inflation at early times and the cosmic acceleration at late times. It is actually possible for viable $f(R)$ models for late time acceleration to include inflation by adding R^2 term. Therefore, it is natural to consider combined $f(R)$ models which describe both primordial and present DE using one $f(R)$ function, albeit one containing two greatly different characteristic energy scales [16, 17]. In [19], it was pointed out that the $f(R)$-gravity can also serve as dark matter (DM). In [20, 23], a set of $f(R)$-gravity models corresponding to different DE models were reconstructed. Although a great variety of $f(R)$ models have been proposed in the literature, most of them is not perfect enough. A viable $f(R)$ model should simultaneously satisfy stringent solar-system bounds on deviations from GR as well as accelerate the expansion at late times.

In order to distinguish between DE and MG, it is crucial to measure the growth of structure in addition to the expansion history. This is because any given expansion history predicted by a MG model could be emulated by a smooth DE component. Measuring the matter velocity field at the locations of the galaxies via spectroscopy helps differentiate between the effect of DE and MG as the source of the accelerating universe through measurements of Redshift Space Distortions (RSD) [25]. RSD was identified by the recent "Rocky III" report as among the most powerful ways of addressing whether the acceleration is caused by DE or MG [26]. For the case of DE model, the growth index is independent of the size of structure, as the structure formation equation for the scales larger than the Jeans length is independent of the wavenumbers while in the MG model, the effective gravitational constant relates the growth index of the structure to its size [27, 28, 29, 30]. An interesting feature of the $f(R)$ theories is the fact that the gravitational constant in $f(R)$-gravity, varies with length scale as well as with time. Thus, the evolution of the matter density perturbation, $\delta_{\rm m} \equiv \delta\rho_{\rm m}/\rho_{\rm m}$, in this theory is affected by the effective Newton coupling constant, $G_{\rm eff}$, and it is scale dependent, too. Therefore, the matter density perturbation is a crucial tool to distinguish MG from DE model in GR, in particular the standard ΛCDM model. The scale dependencies of the linear growth rate of metric and density perturbations in $f(R)$-gravity can change predictions for cosmological power spectra in the linear regime [31].

On the other hand, the connection between gravity and thermodynamics is one of surprising features of gravity which was first reinforced by Jacobson [32], who associated the Einstein field equations with the Clausius relation in the context of black hole thermodynamics. This idea was also extended to the cosmological context and it was shown that the Friedmann equations in the Einstein gravity [33] can be written in the form of the first law of thermodynamics (the Clausius relation). The equivalence between the first law of thermodynamics and the Friedmann equation was also found for $f(R)$-gravity [34]. Besides the first law, the generalized second law (GSL) of gravitational thermodynamics, which states that entropy of the fluid inside the horizon plus the geometric entropy do not decrease with time, was also investigated in $f(R)$-gravity [36]. The GSL of thermodynamics in the accelerating universe driven by DE or MG has been also studied extensively in the literature [37]-[58].

All these motivate us to investigate the growth of matter density perturbations in a class of metric $f(R)$ models and see scale dependence of growth factor. Additionally, we are interested in examining the validity of GSL in some viable $f(R)$-gravity models. The structure of this paper is as follows. In Sec. 2, within the framework of $f(R)$-gravity we consider a spatially flat Friedmann-Robertson-Walker (FRW) universe filled with the pressureless matter and radiation. In Sec. 3, we study the growth rate of matter density perturbations in $f(R)$-gravity. In Sec. 4, the GSL of thermodynamics on the dynamical apparent horizon with the Hawking temperature is explained. In Sec. 5, the cosmological evolution of $f(R)$ models is illustrated. In Sec. 6, the viability conditions for $f(R)$ models are discussed. In addition, some viable $f(R)$ models containing the Starobinsky, Hu-Sawicki, Exponential, Tsujikawa and AB models are introduced. In Sec. 7, we give numerical results obtained for the evolution of some cosmological parameters, the GSL and the growth of structure formation in the aforementioned $f(R)$ models. Finally, Sec. 8 is devoted to conclusions.

2 $f(R)$-gravity framework

Within the framework of $f(R)$-gravity, the modified Einstein-Hilbert action in the Jordan frame is given by [12]

$$S_{\rm J} = \int \sqrt{-g}\ {\rm d}^4x \left[\frac{f(R)}{16\pi G} + L_{\rm matter}\right], \tag{1}$$

where G, g, R and $L_{\rm matter}$ are the gravitational constant, the determinant of the metric $g_{\mu\nu}$, the Ricci scalar and the lagrangian density of the matter inside the universe, respectively. Also, $f(R)$ is an arbitrary function of the Ricci scalar.

Varying the action (1) with respect to $g_{\mu\nu}$ yields

$$FG_{\mu\nu} = 8\pi G T^{(\rm m)}_{\mu\nu} - \frac{1}{2}g_{\mu\nu}(RF - f) + \nabla_\mu\nabla_\nu F - g_{\mu\nu}\Box F. \tag{2}$$

Here, $F = {\rm d}f/{\rm d}R$, $G_{\mu\nu} = R_{\mu\nu} - \frac{1}{2}Rg_{\mu\nu}$ and $T^{(\rm m)}_{\mu\nu}$ is the energy-momentum tensor of the matter. The gravitational field equations (2) can be rewritten in the standard form as [59, 61]

$$G_{\mu\nu} = 8\pi G\big(T^{(\rm m)}_{\mu\nu} + T^{(\rm D)}_{\mu\nu}\big), \tag{3}$$

with

$$8\pi G T^{(\rm D)}_{\mu\nu} = (1-F)G_{\mu\nu} - \frac{1}{2}g_{\mu\nu}(RF - f) + \nabla_\mu\nabla_\nu F - g_{\mu\nu}\Box F. \tag{4}$$

For a spatially flat FRW metric, taking $T^{\mu(m)}_\nu = {\rm diag}(-\rho, p, p, p)$ in the prefect fluid form, then the set of field equations (3) reduce to the modified Friedmann equations in the framework of $f(R)$-gravity as [62]

$$3H^2 = 8\pi G(\rho + \rho_{\rm D}), \tag{5}$$

$$2\dot{H} = -8\pi G(\rho + \rho_{\rm D} + p + p_{\rm D}), \tag{6}$$

where

$$8\pi G\rho_{\rm D} = \frac{1}{2}\big(RF - f\big) - 3H\dot{F} + 3H^2\big(1 - F\big), \tag{7}$$

$$8\pi G p_{\rm D} = \left[\frac{-1}{2}\big(RF - f\big) + \ddot{F} + 2H\dot{F} - (1-F)\big(2\dot{H} + 3H^2\big)\right], \tag{8}$$

with

$$R = 6(\dot{H} + 2H^2). \tag{9}$$

Here, $H = \dot{a}/a$ is the Hubble parameter. Also, $\rho_{\rm D}$ and $p_{\rm D}$ are the curvature contribution to the energy density and pressure which can play the role of DE. Also, $\rho = \rho_{\rm BM} + \rho_{\rm DM} + \rho_{\rm rad}$ and $p = p_{\rm rad} = \rho_{\rm rad}/3$ are the energy density and pressure of the matter inside the universe, consist of the pressureless baryonic and dark matters as well as the radiation. On the whole of the paper, the dot and the subscript R denote the derivatives with respect to the cosmic time t and the Ricci scalar R, respectively.

The energy conservation laws are still given by

$$\dot{\rho}_{\rm m} + 3H\rho_{\rm m} = 0, \tag{10}$$

$$\dot{\rho}_{\rm rad} + 4H\rho_{\rm rad} = 0, \tag{11}$$

$$\dot{\rho}_{\rm D} + 3H(\rho_{\rm D} + p_{\rm D}) = 0, \tag{12}$$

where $\rho_{\rm m} = \rho_{\rm BM} + \rho_{\rm DM}$. From Eqs. (10) and (11) one can find

$$\rho = \frac{\rho_{\rm m_0}}{a^3} + \frac{\rho_{\rm rad_0}}{a^4}, \tag{13}$$

where $\rho_{\rm m_0} = \rho_{\rm BM_0} + \rho_{\rm DM_0}$ and $\rho_{\rm rad_0}$ are the present values of the energy densities of matter and radiation. We also choose $a_0 = 1$ for the recent value of the scale factor.

Using the usual definitions of the density parameters

$$\Omega_{\rm m} = \frac{\rho_{\rm m}}{\rho_{\rm c}} = \frac{8\pi G\rho_{\rm m_0}}{3H^2a^3}, \quad \Omega_{\rm rad} = \frac{\rho_{\rm rad}}{\rho_{\rm c}} = \frac{8\pi G\rho_{\rm rad_0}}{3H^2a^4}, \quad \Omega_{\rm D} = \frac{\rho_{\rm D}}{\rho_{\rm c}} = \frac{8\pi G\rho_{\rm D}}{3H^2}, \tag{14}$$

in which $\rho_{\rm c} = 3H^2/(8\pi G)$ is the critical energy density, the modified Friedmann equation (5) takes the form

$$1 = \Omega_{\rm m} + \Omega_{\rm rad} + \Omega_{\rm D}. \tag{15}$$

From the energy conservation (12), the equation of state (EoS) parameter due to the curvature contribution is defined as

$$\omega_{\rm D} = \frac{p_{\rm D}}{\rho_{\rm D}} = -1 - \frac{\dot{\rho}_{\rm D}}{3H\rho_{\rm D}}. \tag{16}$$

Using the modified Friedmann equations (5) and (6), the effective EoS parameter is obtained as

$$\omega_{\rm eff} = \frac{p + p_{\rm D}}{\rho + \rho_{\rm D}} = -1 - \frac{2\dot{H}}{3H^2}. \tag{17}$$

Also, the two important observational cosmographic parameters called the deceleration q and the jerk j parameters, respectively related to $\ddot{a}$ and $\dddot{a}$, are given by [64]

$$q = -\frac{\ddot{a}}{aH^2} = -1 - \frac{\dot{H}}{H^2} = 1 - \frac{R}{6H^2}, \tag{18}$$

$$j = \frac{\dddot{a}}{aH^3} = 1 - \frac{\dot{H}}{H^2} + \frac{\dot{R}}{6H^3} = 2 + q + \frac{\dot{R}}{6H^3}. \tag{19}$$

Cosmologists believe that the universe transitioned from deceleration to acceleration in a cosmic jerk. The deceleration to acceleration transition of the universe occurs for different models with a positive value of the jerk parameter and negative value of the deceleration parameter [67]. For example, flat ΛCDM models have a constant jerk $j = 1$ [70].

3 Growth rate of matter density perturbations

Here, we study the growth rate of matter density perturbations in $f(R)$-gravity. The origin of structure formation in the universe is seeded by the small quantum fluctuations generated at the inflationary epoch. These small perturbations over time grew to become all of the structure we observe. Once the universe becomes matter dominated, primeval density inhomogeneities ($\delta\rho_{\rm m}/\rho_{\rm m} \sim 10^{-5}$) are amplified by gravity and grow into the structure we see today [71].

The evolution of the matter density contrast $\delta_{\rm m} = \delta\rho_{\rm m}/\rho_{\rm m}$ provides an important tool to distinguish $f(R)$-gravity and generally MG models from DE inside GR and, in particular, from the ΛCDM model. We consider the linear scalar perturbations around a flat FRW background in the Newtonian (longitudinal) gauge as

$$\mathrm{d}s^2 = -(1 + 2\Psi)\mathrm{d}t^2 + a^2(t)(1 + 2\Phi)\mathrm{d}x^2, \tag{20}$$

with two scalar potentials Ψ and Φ describing the perturbations in the metric. In this gauge, the matter density perturbation $\delta_{\rm m}$ and the perturbation of $\delta F(R)$ obey the following equations in the Fourier space [72, 73]

$$\ddot{\delta}_{\rm m} + \left(2H + \frac{\dot{F}}{2F}\right)\dot{\delta}_{\rm m} - \frac{8\pi G\rho_{\rm m}}{2F}\delta_{\rm m} = \frac{1}{2F}\left[\left(-6H^2 + \frac{k^2}{a^2}\right)\delta F + 3H\dot{\delta F} + 3\ddot{\delta F}\right], \tag{21}$$

$$\ddot{\delta F} + 3H\dot{\delta F} + \left(\frac{k^2}{a^2} + \frac{F}{3F_{\rm R}} - \frac{R}{3}\right)\delta F = \frac{8\pi G}{3}\rho_{\rm m}\delta_{\rm m} + \dot{F}\dot{\delta}_{\rm m}, \tag{22}$$

where k is the comoving wave number. For the modes deep inside the Hubble radius ($k^2/a^2 \gg H^2$), with considering this fact that the time derivative of F is small ($|\dot{F}| \ll HF$) and with neglecting the oscillating mode of $\delta F(\ddot{\delta F} \ll H\dot{\delta F} \ll H^2)$, the evolution of matter density contrast $\delta_{\rm m}$ is govern by [74, 75, 77]

$$\ddot{\delta}_{\rm m} + 2H\dot{\delta}_{\rm m} - 4\pi G_{\rm eff}\rho_{\rm m}\delta_{\rm m} = 0, \tag{23}$$

where

$$G_{\rm eff} = \frac{G}{F}\left[\frac{4}{3} - \frac{1}{3}\frac{M^2a^2}{k^2 + M^2a^2}\right], \tag{24}$$

and $M^2 = \frac{F}{3F_{\rm R}}$. The fraction of effective gravitational constant to the Newtonian one, i.e. $G_{\rm eff}/G$, is defined as screened mass function in the literature [29]. Equation (24) obviously shows that the screened mass function is the time and scale dependent parameter.

With the help of new variable namely $g(a) = \delta_{\rm m}/a$ which parameterizes the growth of structure in the matter, Eq. (23) becomes

$$\frac{{\rm d}^2 g}{{\rm d}\ln a^2} + \left(4 + \frac{\dot{H}}{H^2}\right)\frac{{\rm d}g}{{\rm d}\ln a} + \left(3 + \frac{\dot{H}}{H^2} - \frac{4\pi G_{\rm eff}\rho_{\rm m}}{H^2}\right)g = 0. \tag{25}$$

In general, there is no analytical solution to this equation. But in [79] for an asymptotic form of viable $f(R)$ models at high curvature regime given by $f(R) = R + R^{-n}$ where $n > -1$, an analytic solution for density perturbations in the matter component during the matter dominated stage was obtained in terms of hypergeometric functions. In what follows, we solve the differential equation (25), numerically. To this aim, the natural choice for the initial conditions are $g(a_{\rm m}) = 1$ and $\frac{{\rm dg}}{{\rm d\,ln\,a}}\,|_{a=a_{\rm m}} = 0$, where $a_{\rm m} = 1/(1+z_{\rm m})$ should be taken during the matter era, because for the matter dominated universe, i.e. $H^2 = 8\pi G\rho_{\rm m}/3$ and $G_{\rm eff}/G = 1$, the solution of Eq. (23) yields $\delta_{\rm m} = a$. The other useful quantity is the logarithmic rate of change of matter density with respect to the scale factor, known as the growth factor. The growth factor is defined as [80]

$$f(z) = \frac{{\rm d}\ln\delta_{\rm m}}{{\rm d}\ln a} = -(1+z)\frac{{\rm d}\ln\delta_{\rm m}}{{\rm d}z}, \tag{26}$$

which is an observational parameter. The redshift space distortion is used as a probe to measure the growth rate of the structures, $f(z)$, to underpin the expansion history of the universe and to distinguish between MG and DE theories [30]. In the present work, we obtain the evolution of linear perturbations relevant to the matter spectrum for the scales; $k = 0.1, 0.01, 0.001\ h\ {\rm Mpc}^{-1}$, where h corresponds to the Hubble parameter today. For smaller scales, $k > 0.2\ h\ {\rm Mpc}^{-1}$, the effect of non-linearity becomes important. In the non-linear regime, while gravity is still in the weak field limit, density fluctuations are no longer small and in addition, the density or potential fields may couple to additional scalar fields introduced in MG theories. The non-linear regime is therefore the hardest to describe in any general way as the nature of the coupling to scalar fields is theory specific [82].

4 Generalized second law of thermodynamics

Here, we are interested in examining the validity of the GSL of gravitational thermodynamics for a given $f(R)$ model. According to the GSL, entropy of the matter inside the horizon beside the entropy associated with the surface of horizon should not decrease during the time [33]. As demonstrated by Bekenstein, this law is satisfied by black holes in contact with their radiation [83]. The entropy of the matter containing the pressureless matter and radiation inside the horizon is given by the Gibbs' equation [37]

$$T_{\rm A}{\rm d}S = {\rm d}E + p{\rm d}V, \tag{27}$$

where $E = (\rho_{\rm m} + \rho_{\rm rad})V$, $V = \frac{4\pi}{3}\tilde{r}_{\rm A}^3$ is the volume containing the matter with the radius of the dynamical apparent horizon $\tilde{r}_{\rm A} = (H^2 + \frac{K}{a^2})^{-1/2}$ and $T_{\rm A} = \frac{1}{2\pi\tilde{r}_{\rm A}}\big(1 - \frac{\dot{\tilde{r}}_{\rm A}}{2H\tilde{r}_{\rm A}}\big)$ is the Hawking temperature. Here, $p = p_{\rm rad} = \rho_{\rm rad}/3$ is the total pressure of the matter inside the universe, consist of the pressureless baryonic and dark matters as well as the radiation. Taking time derivative of Eq. (27) and using the energy equations (10)-(11) as well as the Friedmann equations (5)-(6) for a spatially flat FRW universe ($K = 0$), one can find

$$T_{\rm A}\dot{S} = \frac{\tilde{r}_{\rm A}^2}{2G}\left(\dot{\tilde{r}}_{\rm A} - H\tilde{r}_{\rm A}\right)\left(-2\dot{H} + H\frac{\rm d}{{\rm d}t} - \frac{{\rm d}^2}{{\rm d}t^2}\right)F. \tag{28}$$

The horizon entropy in $f(R)$-gravity is given by $S_{\rm A} = \frac{AF}{4G}$ [84], where $A = 4\pi\tilde{r}_{\rm A}^2$ is the area of the apparent horizon. Taking the time derivative of $S_{\rm A}$, one can get the evolution of horizon entropy as

$$T_{\rm A}\dot{S}_{\rm A} = \frac{1}{4GH}\left(2H\tilde{r}_{\rm A} - \dot{\tilde{r}}_{\rm A}\right)\left(\frac{2\dot{\tilde{r}}_{\rm A}}{\tilde{r}_{\rm A}} + \frac{\rm d}{{\rm d}t}\right)F. \tag{29}$$

Now, we can calculate the GSL due to different contributions of the matter and horizon. Adding Eqs. (28) and (29), one can get the GSL in $f(R)$-gravity as [36]

$$T_{\rm A}\dot{S}_{\rm tot} = \frac{1}{4GH^4}\left[2\dot{H}^2F - \dot{H}H\dot{F} + 2(\dot{H} + H^2)\ddot{F}\right], \tag{30}$$

where $S_{\rm tot} = S + S_{\rm A}$. Note that Eq. (30) shows that the validity of the GSL, i.e. $T_{\rm A}\dot{S}_{\rm tot} \geq 0$ depends on the $f(R)$-gravity model. For the Einstein gravity ($F = 1$), one can immediately find that the GSL (30) reduces to

$$T_{\rm A}\dot{S}_{\rm tot} = \frac{\dot{H}^2}{2GH^4} \geq 0, \tag{31}$$

which shows that the GSL is always fulfilled throughout history of the universe. Within the framework of Einstein's gravity, it was also shown that the GSL in the presence of DE is always satisfied during history of the universe [37]. The GSL of thermodynamics is a universal principle governing the universe. As is well known, the GSL is a powerful tool to set bounds on astrophysical and cosmological models [86]. The satisfaction of the GSL of thermodynamics provides further confidence on the thermodynamical interpretation of gravity in $f(R)$ scenario based on the profound connection between gravity and thermodynamics. Therefore, as one of the most important theoretical touchstones to examine whether $f(R)$-gravity can be an alternative gravitational theory to GR, we examine the validity of the GSL for some viable $f(R)$ models in subsequent sections.

5 Cosmological evolution

Here, we recast the differential equations governing the evolution of the universe in dimensionless form which is more suitable for numerical integration. To do so, following [91] we use the dimensionless quantities

$$\bar{t} = H_0 t, \quad \bar{H} = \frac{H}{H_0}, \quad \bar{R} = \frac{R}{H_0^2}, \tag{32}$$

$$\bar{f} = \frac{f}{H_0^2}, \quad \bar{F} = F, \quad \bar{F}_{\rm R} = \frac{F_{\rm R}}{H_0^{-2}}, \quad \bar{F}_{\rm RR} = \frac{F_{\rm RR}}{H_0^{-4}}, \tag{33}$$

where H_0 is the Hubble parameter today. With the help of the above definitions and using

$$\frac{\mathrm{d}}{\mathrm{d}\bar{t}} = -\bar{H}(1+z)\frac{\mathrm{d}}{\mathrm{d}z}, \tag{34}$$

one can rewrite the modified Friedmann equation (5) as follows

$$\bar{H}^2 = \Omega_{\rm m_0}\left[(1+z)^3+\chi(1+z)^4\right]+(\bar{F}-1)\left[\bar{H}^2-(1+z)\bar{H}\bar{H}'\right]-\frac{1}{6}\left(\bar{f}-\bar{R}\right)+(1+z)\bar{H}^2\bar{F}_R\bar{R}', \tag{35}$$

where $\chi = \rho_{\rm rad_0}/\rho_{\rm m_0} = \Omega_{\rm rad_0}/\Omega_{\rm m_0}$ and prime '$'$' denotes a derivative with respect to the cosmological redshift $z = \frac{1}{a} - 1$.

To solve Eq. (35), we introduce new variables as [92]:

$$y_{\rm H} := \frac{\rho_{\rm D}}{\rho_{\rm m_0}} = \frac{\bar{H}^2}{\Omega_{\rm m_0}} - (1+z)^3 - \chi(1+z)^4, \tag{36}$$

and

$$y_{\rm R} := \frac{\bar{R}}{\Omega_{\rm m_0}} - 3(1+z)^3. \tag{37}$$

Taking the derivative of both sides of Eqs. (36) and (37) with respect to redshift z yield

$$-(1+z)y'_{\rm H} = \frac{1}{3}y_{\rm R} - 4y_{\rm H}, \tag{38}$$

$$\begin{aligned} -(1+z)y'_{\rm R} \;=\; & 9(1+z)^3 - \frac{1}{\bar{H}^2\bar{F}_{\rm R}}\left\{y_{\rm H} + \frac{1}{6\Omega_{\rm m_0}}(\bar{f}-\bar{R})\right. \\ & \left.-(\bar{F}-1)\left[\frac{y_{\rm R}}{6} - y_{\rm H} - \frac{1}{2}\Big((1+z)^3 + 2\chi(1+z)^4\Big)\right]\right\}. \end{aligned} \tag{39}$$

Finally, inserting Eq. (39) into the derivative of Eq. (38) gives a second differential equation governing $y_{\rm H}(z)$ as [93]

$$(1+z)^2 y''_{\rm H} + J_1(1+z)y'_{\rm H} + J_2 y_{\rm H} + J_3 = 0, \tag{40}$$

where

$$J_1 = -3 - \left(\frac{1-\bar{F}}{6\bar{H}^2\bar{F}_{\rm R}}\right), \tag{41}$$

$$J_2 = \frac{2-\bar{F}}{3\bar{H}^2\bar{F}_{\rm R}}, \tag{42}$$

$$J_3 = -3(1+z)^3 - \frac{1}{6\bar{H}^2\bar{F}_{\rm R}}\left[(1-\bar{F})\Big((1+z)^3 + 2\chi(1+z)^4\Big) + \frac{1}{3\Omega_{\rm m_0}}(\bar{R}-\bar{f})\right]. \quad (43)$$

Equation (40) cannot be solved analytically. Hence, we need to solve it numerically. To do so, we use the two initial conditions $y_{\rm H}(z_{\rm i}) = 3$ and $y'_{\rm H}(z_{\rm i}) = 0$ which come from the ΛCDM approximation of $f(R)$ model in high curvature regime. Notice $z_{\rm i}$ is the proper redshift in which we have $RF_{\rm R}(z_{\rm i}) \leq 10^{-13}$.

With the help of Eqs. (14), (16), (17) and (36), one can obtain the evolutionary behaviors of the matter density parameter, $\Omega_{\rm m}(z)$, DE density parameter, $\Omega_{\rm D}(z)$, EoS parameter of DE, $\omega_{\rm D}(z)$, and effective EoS parameter, $\omega_{\rm eff}(z)$, in terms of $y_{\rm H}$ and its derivatives as follows

$$\Omega_{\rm m}(z) = \frac{(1+z)^3}{y_{\rm H} + (1+z)^3 + \chi(1+z)^4}, \quad (44)$$

$$\Omega_{\rm D}(z) = \frac{y_{\rm H}}{y_{\rm H} + (1+z)^3 + \chi(1+z)^4}, \quad (45)$$

$$\omega_{\rm D}(z) = -1 + \frac{1+z}{3}\left(\frac{y'_{\rm H}}{y_{\rm H}}\right), \quad (46)$$

$$\omega_{\rm eff}(z) = -1 + \frac{(1+z)}{3}\left[\frac{y'_{\rm H} + 3(1+z)^2 + 4\chi(1+z)^3}{y_{\rm H} + (1+z)^3 + \chi(1+z)^4}\right]. \quad (47)$$

Also from Eqs. (18), (19) and (36) one can get the evolutions of the deceleration and jerk parameters as

$$q(z) = -1 + \frac{(1+z)}{2}\left[\frac{y'_{\rm H} + 3(1+z)^2 + 4\chi(1+z)^3}{y_{\rm H} + (1+z)^3 + \chi(1+z)^4}\right], \quad (48)$$

$$j(z) = 1 + \frac{(1+z)}{2}\left[\frac{(1+z)y''_{\rm H} - 2y'_{\rm H} + 4\chi(1+z)^3}{y_{\rm H} + (1+z)^3 + \chi(1+z)^4}\right]. \quad (49)$$

6 Viable $f(R)$-gravity models

The necessary conditions for having a viable $f(R)$ model can be summarized as follows:
(i) $F > 0$, which keeps the positivity of the effective gravitational coupling constant and avoids anti-gravity.
(ii) $F_{\rm R} > 0$, which gives the stability condition of cosmological perturbations [31, 96, 97].
(iii) In the large curvature regime ($R/R_0 \gg 1$), the $f(R)$ model behaves like ΛCDM model. It means that $f(R) \to R - 2\Lambda$, where R_0 is the Ricci scalar today. This is required for the presence of the matter-dominated stage.
(iv) A stable late time de Sitter point; the condition which is required for this stability is, $0 < m(R = R_{\rm d}) < 1$ [98], where $m \equiv \frac{RF_{\rm R}}{F}$ and $R_{\rm d} = 2f(R_{\rm d})/F(R_{\rm d})$ is the value of the scalar curvature at the de Sitter point. Note that the quantity m characterizes the deviation from the ΛCDM model.
(v) Passing constraint from the equivalence principle and solar system test [99].

Since we are intersected in investigating the growth of structure formation and examining the GSL in $f(R)$-gravity, hence in what follows we consider some viable $f(R)$ models including the Starobinsky, Hu-Sawicki, Exponential, Tsujikawa and AB models which satisfy the conditions (i) to (v).

6.1 Starobinsky Model

The Starobinsky $f(R)$ model is as follows [74]

$$f(R) = R + \lambda R_{\rm s}\left[\left(1+\frac{R^2}{R_{\rm s}^2}\right)^{-n} - 1\right], \tag{50}$$

where $n > 0$, λ and $R_{\rm s}$ are constant parameters of the model. Following [100], we take $n = 2$ and $\lambda = 1$. Note that in the high z regime ($z \simeq z_{\rm i}$), we have $R/R_{\rm s} \gg 1$. This yields the $f(R)$ model (50) to behave like the ΛCDM model, i.e. $f(R) = R - 2\Lambda$. Consequently, the constant parameter $R_{\rm s}$ is obtained as $R_{\rm s} = 18\Omega_{\rm m_0}H_0^2/\lambda$.

6.2 Hu-Sawicki Model

This model was reconstructed based on the local observational data and presented by Hu and Sawicki [92] as

$$f(R) = R - \frac{c_1 R_{\rm s}\left(\frac{R}{R_{\rm s}}\right)^n}{c_2\left(\frac{R}{R_{\rm s}}\right)^n + 1}, \tag{51}$$

where $n > 0$, c_1, c_2 and $R_{\rm s}$ are constants of the model. For this model, we take $n = 4$, $c_1 = 1.25 \times 10^{-3}, c_2 = 6.56 \times 10^{-5}$ [91], and obtain $R_{\rm s} = 18c_2\Omega_{\rm m_0}H_0^2/c_1$.

6.3 Exponential Model

This model is defined by the following function [93],

$$f(R) = R - \beta R_{\rm s}\left(1 - e^{-\frac{R}{R_{\rm s}}}\right), \tag{52}$$

where β and $R_{\rm s}$ are two constants of the model. Here, $R_{\rm s}$ corresponds to the characteristic curvature modification scale. Here, we take $\beta = 1.8$ [93] and obtain $R_{\rm s} = 18\Omega_{\rm m_0}H_0^2/\beta$.

6.4 Tsujikawa Model

This model was originally presented in [73] as

$$f(R) = R - \lambda R_{\rm s}\tanh\left(\frac{R}{R_{\rm s}}\right), \tag{53}$$

where λ and $R_{\rm s}$ are the model parameters. For this model, we obtain $R_{\rm s} = 18\Omega_{\rm m_0}H_0^2/\lambda$ and set $\lambda = 1$ [101].

6.5 AB Model

This model was proposed by Appleby and Battye [16, 103] as

$$f(R) = \frac{R}{2} + \frac{\epsilon}{2}\log\left[\frac{\cosh\left(\frac{R}{\epsilon} - b\right)}{\cosh(b)}\right], \tag{54}$$

where b is a dimensionless constant and $\epsilon = R_{\rm s}/\big[b + \log(2\cosh b)\big]$. The constant $R_{\rm s}$ can be obtained at high curvature regime when the AB $f(R)$ model (54) behaves like the ΛCDM model, i.e. $f(R) = R - 2\Lambda$. This gives

$$R_{\rm s} = \frac{-36\ \Omega_{\rm m_0}H_0^2\big[b + \log(2\cosh b)\big]}{\log\left(\frac{1-\tanh b}{2}\right)}.$$

Here, we also set $b = 1.4$.

7 Numerical results

Here to solve Eq. (40) numerically, we choose the cosmological parameters $\Omega_{\mathrm{m}_0} = 0.24$, $\Omega_{\mathrm{D}_0} = 0.76$ and $\Omega_{\mathrm{rad}_0} = 4.1 \times 10^{-5}$. As we have already mentioned, we use the two suitable initial conditions $y_{\mathrm{H}}(z_{\mathrm{i}}) = 3$ and $y'_{\mathrm{H}}(z_{\mathrm{i}}) = 0$, in which z_{i} is obtained where $RF_{\mathrm{R}} \to 10^{-13}$. For the Starobinsky, Hu-Sawicki, Exponential, Tsujikawa and AB $f(R)$ models, we obtain z_{i} =15.61, 13.12, 3.66, 3.52 and 3.00, respectively.

In addition, to study the growth rate of matter density perturbations, we numerically solve Eq. (25) with the initial conditions $g(z_{\mathrm{m}}) = 1$ and $(\mathrm{d}g/\mathrm{d}\ln a)|_{z_{\mathrm{m}}} = 0$, in which z_{m} is obtained where $\Omega_{\mathrm{m}}(z_{\mathrm{m}}) = 1$. For the aforementioned models, we obtain z_{m} =14, 13, 12, 14 and 14.36, respectively.

With the help of numerical results obtained for $y_{\mathrm{H}}(z)$ in Eq. (40), we can obtain the evolutionary behaviors of H, R, q, Ω_{m}, Ω_{D}, ω_{eff}, ω_{D} and GSL for our selected $f(R)$ models. The results for the Starobinsky, Hu-Sawicki, Exponential, Tsujikawa and AB $f(R)$ models are displayed in Figs. 1-5. Figures show that: (i) the Hubble parameter and the Ricci scalar decrease during history of the universe. (ii) The deceleration parameter q varies from an early matter-dominant epoch ($q = 0.5$) to the de Sitter era ($q = -1$) in the future, as expected. It also shows a transition from a cosmic deceleration $q > 0$ to the acceleration $q < 0$ in the near past. The current values of the deceleration parameter for the Starobinsky, Hu-Sawicki, Exponential, Tsujikawa and AB $f(R)$ models are obtained as $q_0 = -0.56$, -0.60, -0.56, -0.57 and -0.60, respectively. These are in good agreement with the recent observational constraint $q_0 = -0.43^{+0.13}_{-0.17}$ (68% CL) obtained by the cosmography [105]. (iii) The density parameters Ω_{D} and Ω_{m} increases and decreases, respectively, as z decreases. (iv) The effective EoS parameter, ω_{eff}, for the all models, starts from an early matter-dominated regime (i.e. $\omega_{\mathrm{eff}} = 0$) and in the late time, $z \to -1$, it behaves like the ΛCDM model, $\omega_{\mathrm{eff}} \to -1$. (v) The EoS parameter of DE, ω_{D}, for the all models starts at the phase of a cosmological constant, i.e. $\omega_{\mathrm{D}} = -1$, and evolves from the phantom phase, $\omega_{\mathrm{D}} < -1$, to the non-phantom (quintessence) phase, $\omega_{\mathrm{D}} > -1$. The crossing of the phantom divide line $\omega_{\mathrm{D}} = -1$ occurs in the near past as well as farther future. At late times ($z \to -1$), ω_{D} approaches again to -1 like the ΛCDM model. Moreover, the present values of ω_{D} for the Starobinsky, Hu-Sawicki, Exponential, Tsujikawa and AB $f(R)$ models are obtained as $\omega_{\mathrm{D}_0} = -0.94$, -0.98, -0.93, -0.94 and -0.97, respectively. These values satisfy the present observational constraints [2, 4].

(vi) The variation of the GSL shows that it holds for the aforementioned models from early times to the present epoch. But in the farther future, the GSL for the Starobinsky, Hu-Sawicki, Exponential, Tsujikawa and AB $f(R)$ models is violated for $-0.996 < z < -0.955$, $-0.935 < z < -0.909$, $-0.897 < z < -0.751$, $-0.997 < z < -0.958$ and $-0.995 < z < -0.950$, respectively. To investigate this problem in ample detail, using Eq. (17) we rewrite Eq. (30) in terms of ω_{eff} as

$$T_{\mathrm{A}}\dot{S}_{\mathrm{tot}} = \frac{1}{4G}\left[\frac{9}{2}(1+\omega_{\mathrm{eff}})^2 F + \frac{3}{2}(1+\omega_{\mathrm{eff}})\frac{\dot{F}}{H} - (1+3\omega_{\mathrm{eff}})\frac{\ddot{F}}{H^2}\right], \tag{55}$$

which shows that in the farther future $z \to -1$ when $\omega_{\mathrm{eff}} \to -1$ (see Figs. 1-5), we have

$$T_{\mathrm{A}}\dot{S}_{\mathrm{tot}} \simeq \frac{\ddot{F}}{2GH^2}. \tag{56}$$

According to Eq. (56), the validity of GSL, i.e. $T_{\rm A}\dot{S}_{\rm tot} \geq 0$, depends on the sign of $\ddot{F}$. In Figs. 1-5, we plot the variation of $\ddot{F}/(2H^2)$ versus z in the farther future for the selected $f(R)$ models. Figures confirm that when the sign of $\ddot{F}$ changes from positive to negative due to the dominance of DE over non-relativistic matter then the GSL is violated. As we know that the natural tendency of any system is to evolve toward thermodynamic equilibrium which is characterized by a state of maximum entropy. In the context of an ever expanding FRW universe, this translates in that the entropy of the apparent horizon plus that of matter and fields enclosed by it must fulfill the GSL of thermodynamics, i.e. $T_{\rm A}\dot{S}_{\rm tot} \geq 0$. Thus, the violation of the GSL in a $f(R)$ model means that the model does not approach thermodynamic equilibrium at late times [106]. Of course, as we already mentioned, the GSL can be used as a powerful tool to set bounds on cosmological $f(R)$ models [86]. It means that we can set the parameters of a given $f(R)$ model so that the GSL holds throughout the evolution of the universe. Although the parameters used for each model in Figs. 1-5 are the viable ones, by more fine tuning the model parameters the GSL can be held and consequently the model approaches thermodynamic equilibrium at late times. For instance, in AB $f(R)$ model by choosing the model parameter as $b = 1.3$, the GSL is always satisfied from early times to the late cosmological history of the universe.

In Figs. 6-10, we plot the evolutions of $RF_{\rm R}$, $G_{\rm eff}/G$, g and the growth factor f versus z for the selected $f(R)$ models. Figures show that: (i) $RF_{\rm R}$ goes to zero for higher values of z which means that the $f(R)$ models at high z regime behave like the ΛCDM model. (ii) The screened mass function $G_{\rm eff}/G$ for a given wavenumber k is larger than one which makes a faster growth of the structures compared to the GR. However, for the higher redshifts, the screened mass function approaches to unity in which the GR structure formation is recovered. Note that the deviation of $G_{\rm eff}/G$ from unity for small scale structures (larger k) is greater than large scale structures (smaller k). (iii) The linear density contrast relative to its value in a pure matter model $g = \delta/a$ starts from an early matter-dominated phase, i.e. $g \simeq 1$ and decreases during history of the universe. For a given z, g in the all $f(R)$ models is greater than that in the ΛCDM model. (iv) The evolution of the growth factor $f(z)$ for $f(R)$ models and ΛCDM model together with the 11 observational data of the growth factor listed in Table 1 show that for smaller structures (larger k), the all $f(R)$ models deviate from the observational data. But for larger structures (smaller k), the growth factor in the all $f(R)$ models, very similar to the ΛCDM model, fits the data very well.

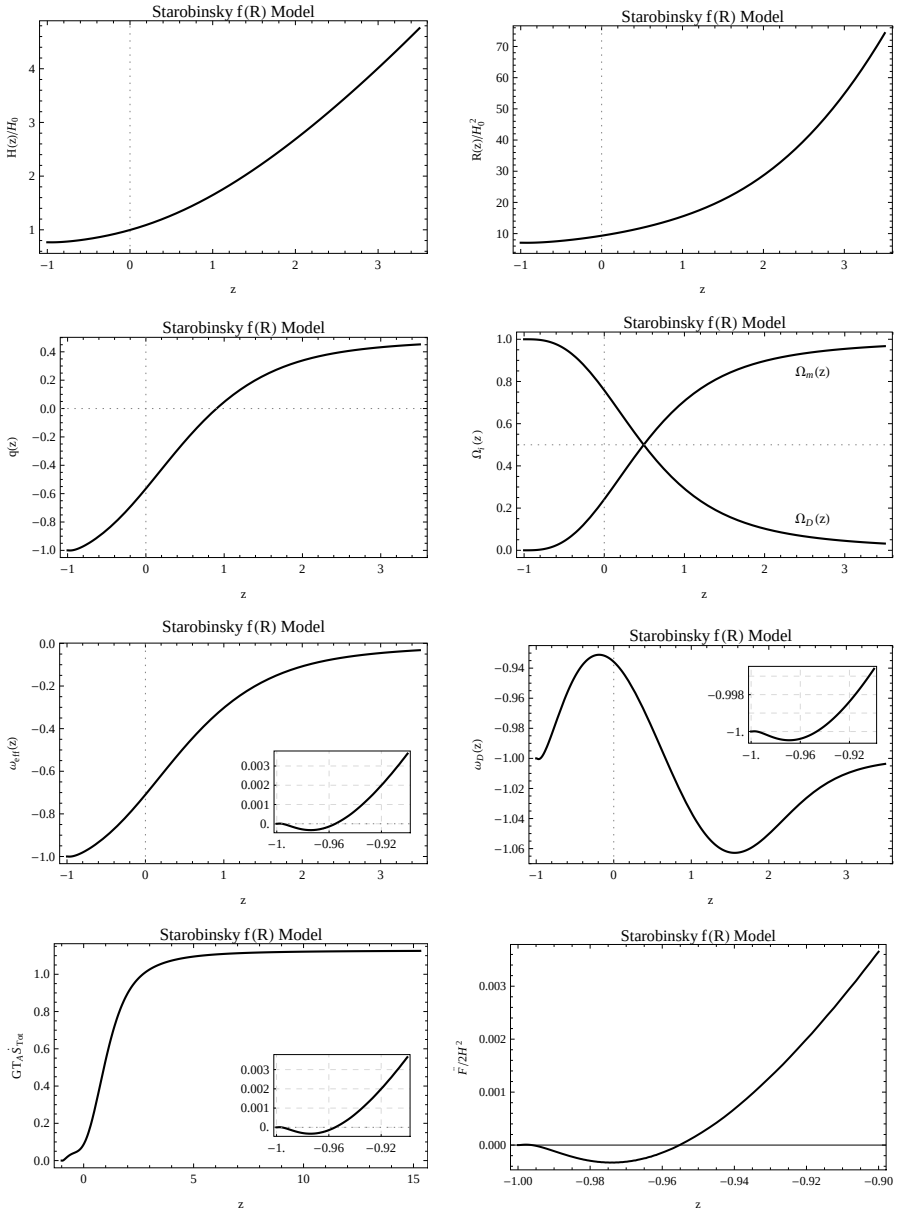

Figure 1: The variations of the Hubble parameter H/H_0, the Ricci scalar R/H_0^2, the deceleration parameter q, the density parameter $\Omega_{\rm i}$, the effective EoS parameter $\omega_{\rm eff}$, the EoS parameter of DE $\omega_{\rm D}$, the GSL, $GT_{\rm A}\dot{S}_{\rm tot}$ and $\frac{\ddot{F}}{2H^2}$ versus redshift z for the Starobinsky model. Auxiliary parameters are $\Omega_{\rm m_0} = 0.24$, $\Omega_{\rm D_0} = 0.76$, $\Omega_{\rm rad_0} = 4.1 \times 10^{-5}$, $\lambda = 1$ and $n = 2$.

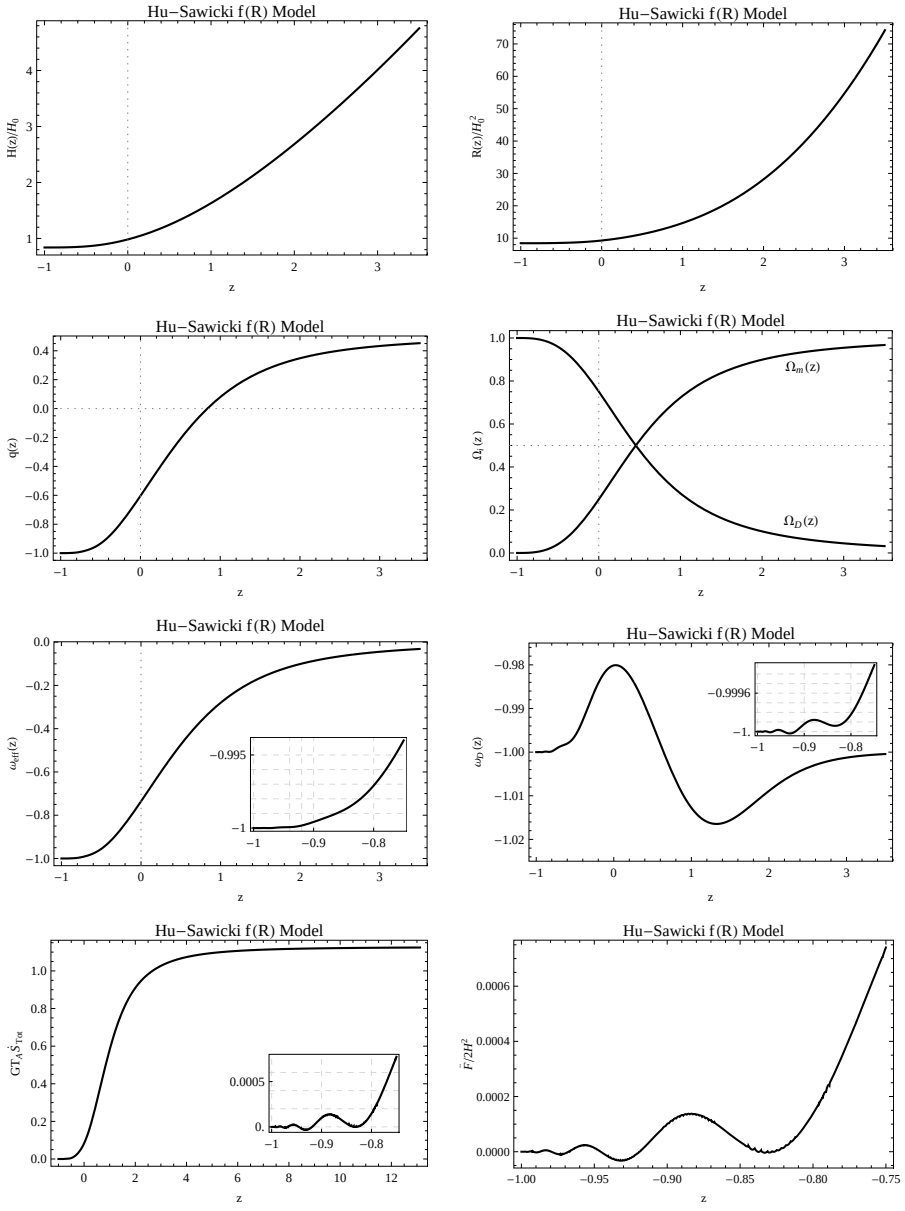

Figure 2: Same as Fig. 1 but for the Hu-Sawicki model. Auxiliary parameters are $\Omega_{\mathrm{m}_0} = 0.24$, $\Omega_{\mathrm{D}_0} = 0.76$, $\Omega_{\mathrm{rad}_0} = 4.1 \times 10^{-5}$, $c_1 = 1.25 \times 10^{-3}$, $c_2 = 6.56 \times 10^{-5}$ and $n = 4$.

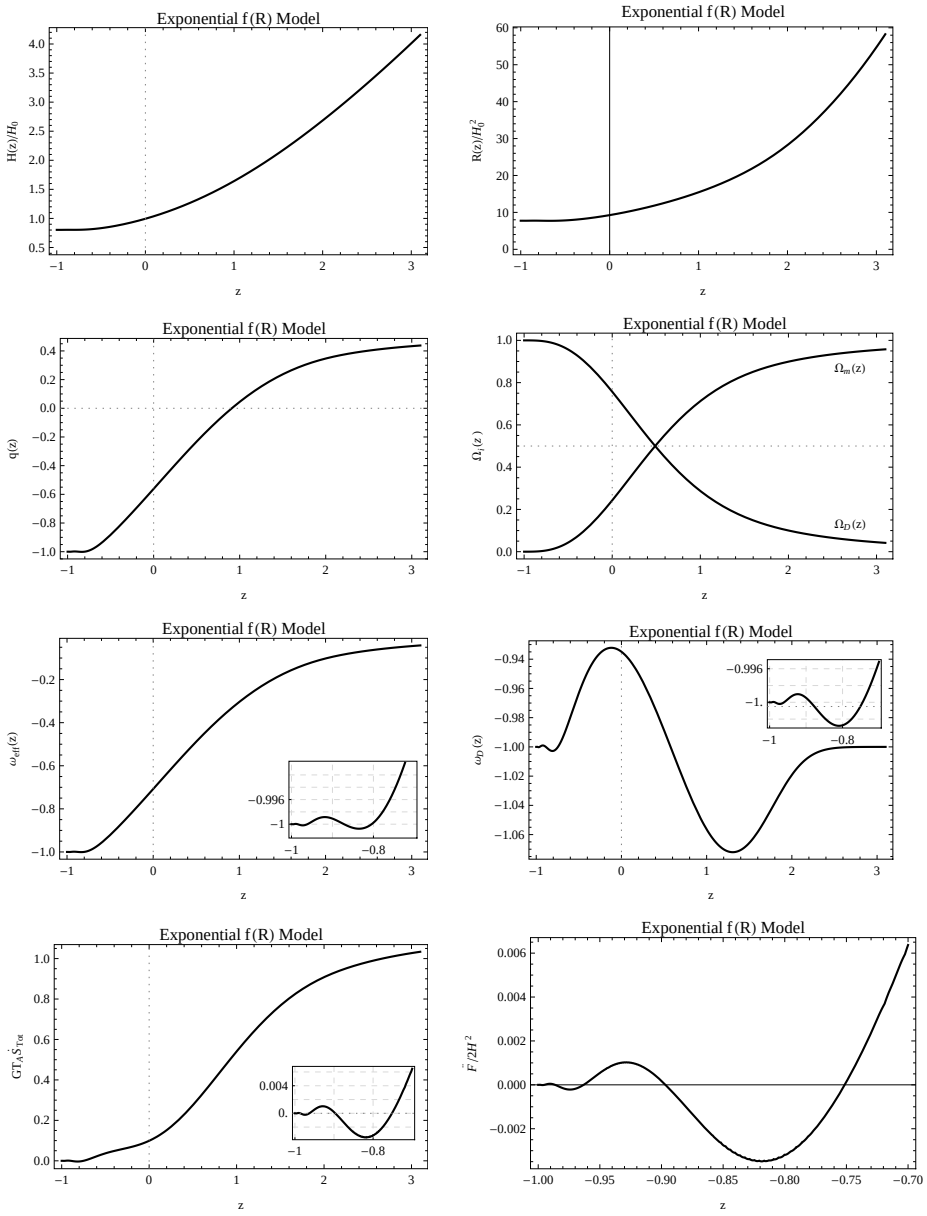

Figure 3: Same as Fig. 1 but for the Exponential model. Auxiliary parameters are $\Omega_{\mathrm{m}_0} = 0.24$, $\Omega_{\mathrm{D}_0} = 0.76$, $\Omega_{\mathrm{rad}_0} = 4.1 \times 10^{-5}$ and $\beta = 1.8$.

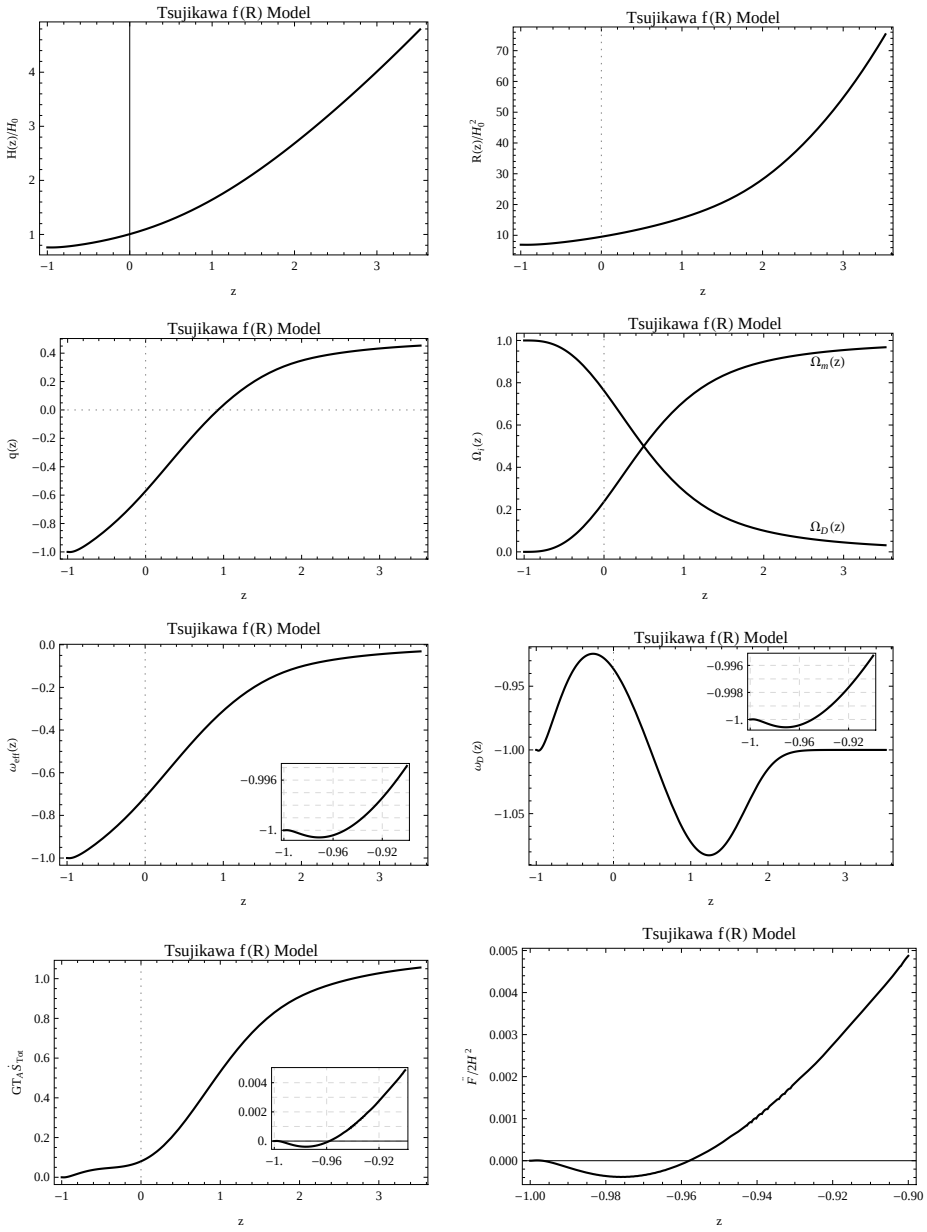

Figure 4: Same as Fig. 1 but for the Tsujikawa model. Auxiliary parameters are $\Omega_{\mathrm{m}_0} = 0.24$, $\Omega_{\mathrm{D}_0} = 0.76$, $\Omega_{\mathrm{rad}_0} = 4.1 \times 10^{-5}$ and $\lambda = 1$.

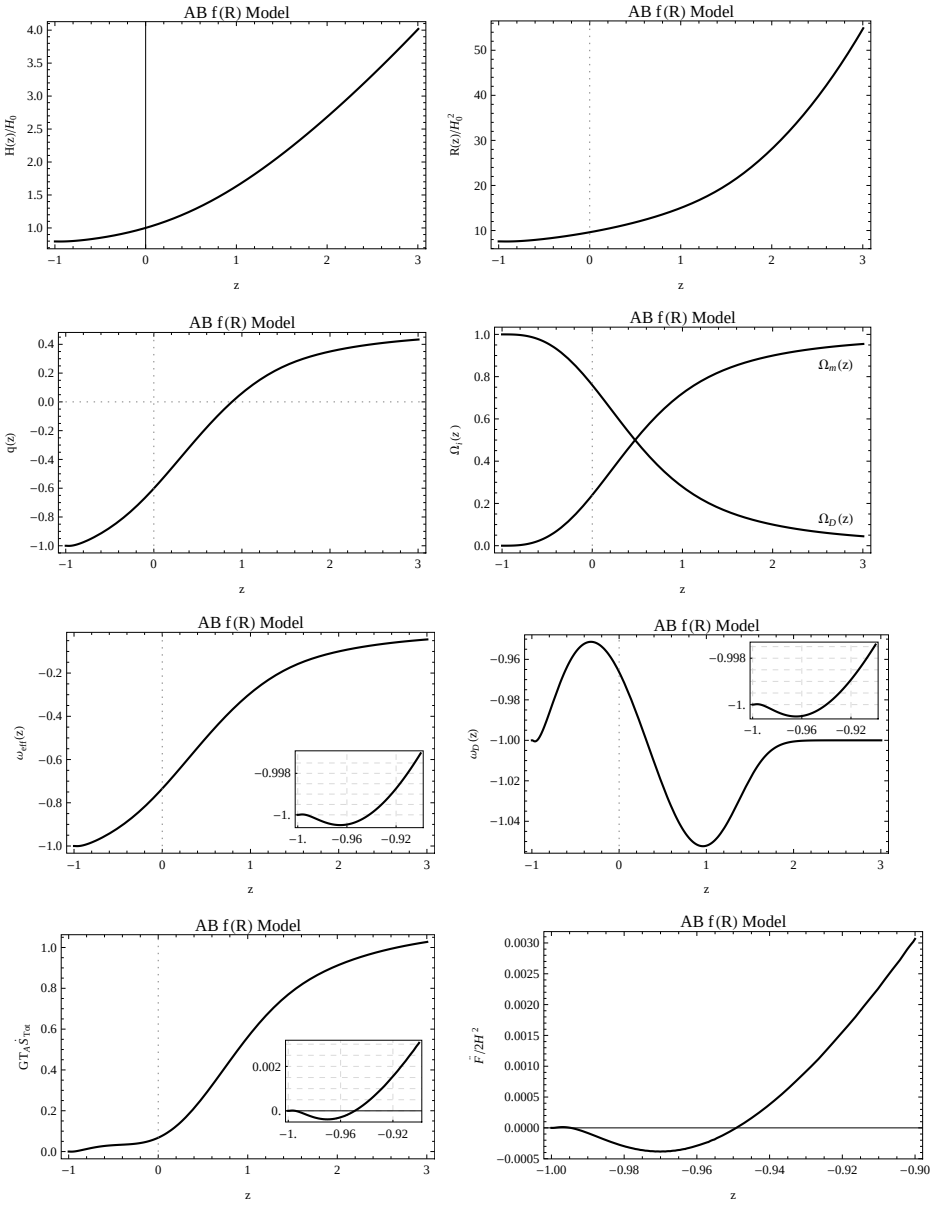

Figure 5: Same as Fig. 1 but for the AB model. Auxiliary parameters are $\Omega_{\mathrm{m}_0} = 0.24$, $\Omega_{\mathrm{D}_0} = 0.76$, $\Omega_{\mathrm{rad}_0} = 4.1 \times 10^{-5}$ and $b = 1.4$.

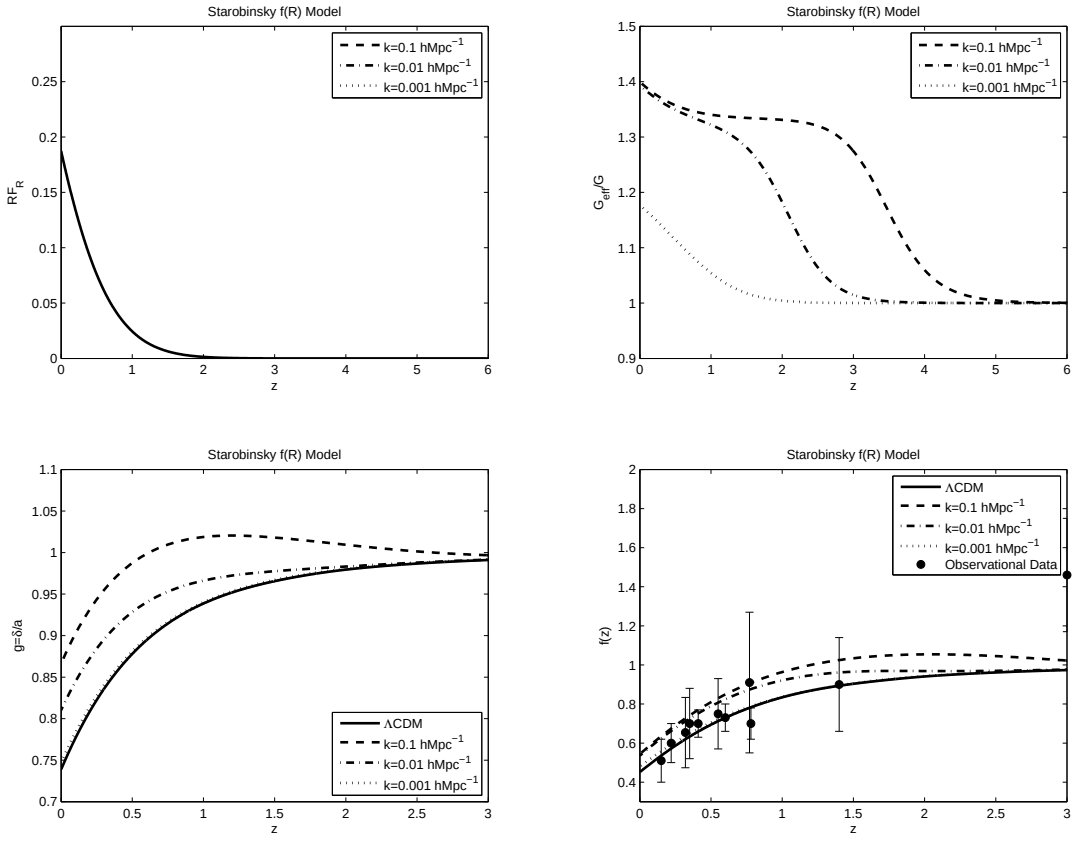

Figure 6: The variations of $RF_{\rm R}$, the screened mass function $G_{\rm eff}/G$, the linear density contrast relative to its value in a pure matter model $g = \delta/a$ and the growth factor $f(z)$, versus redshift z for the Starobinsky model.

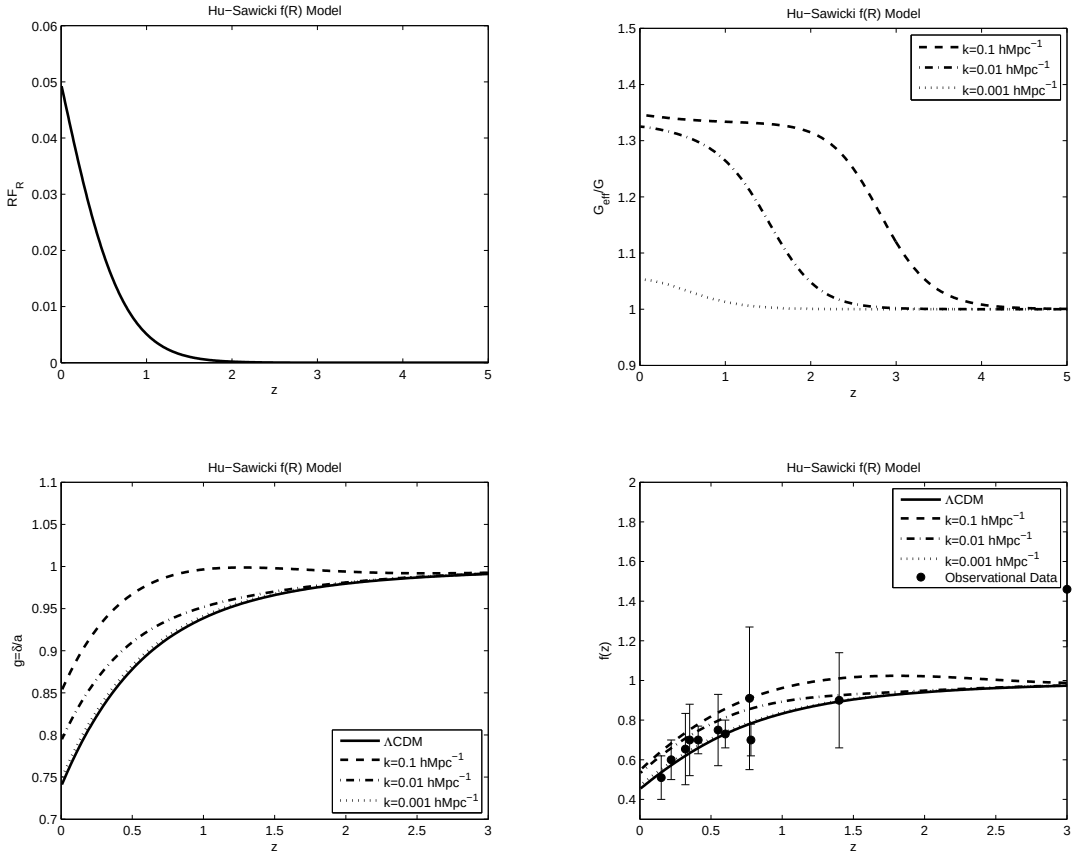

Figure 7: Same as Fig. 6 but for the Hu-Sawicki model.

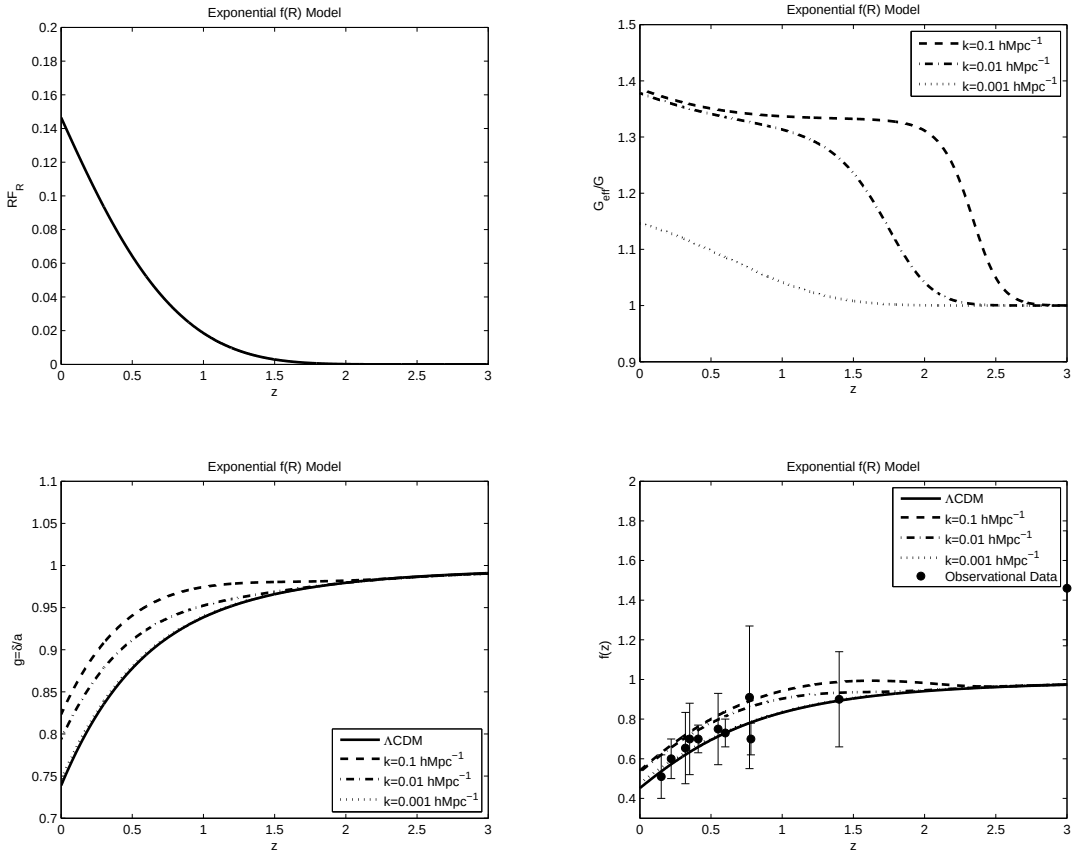

Figure 8: Same as Fig. 6 but for the Exponential model.

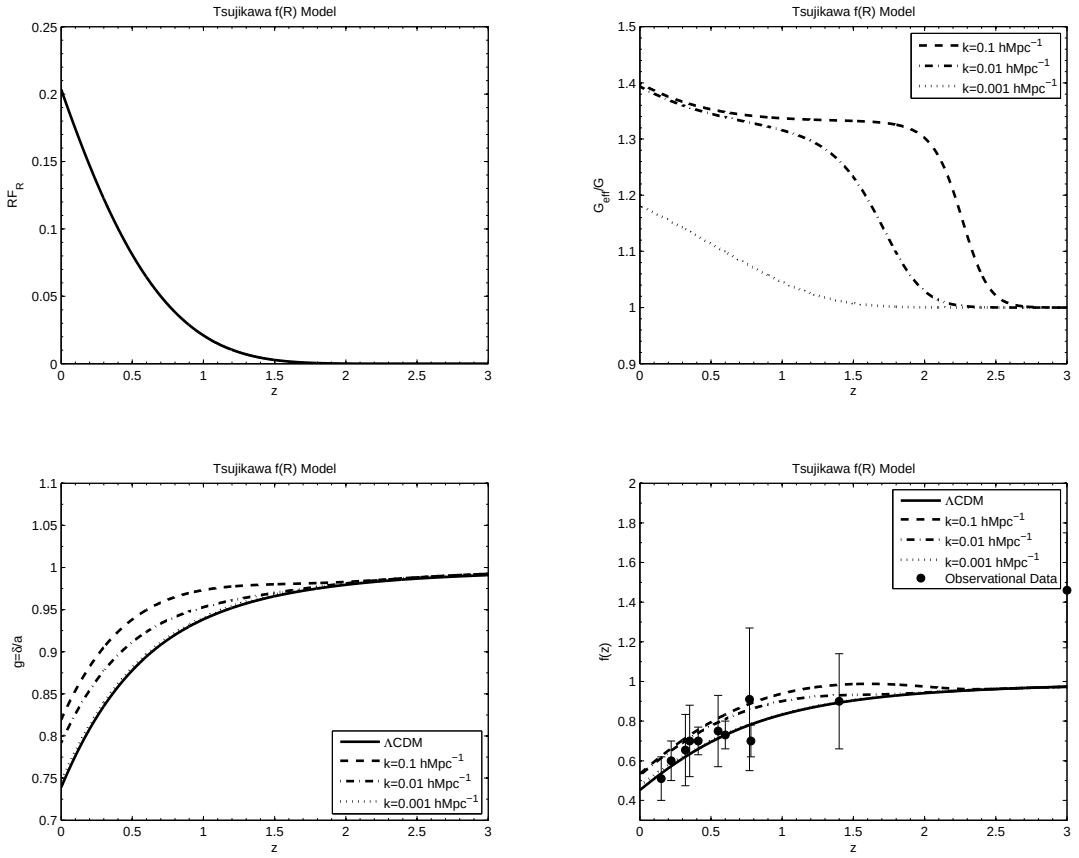

Figure 9: Same as Fig. 6 but for the Tsujikawa model.

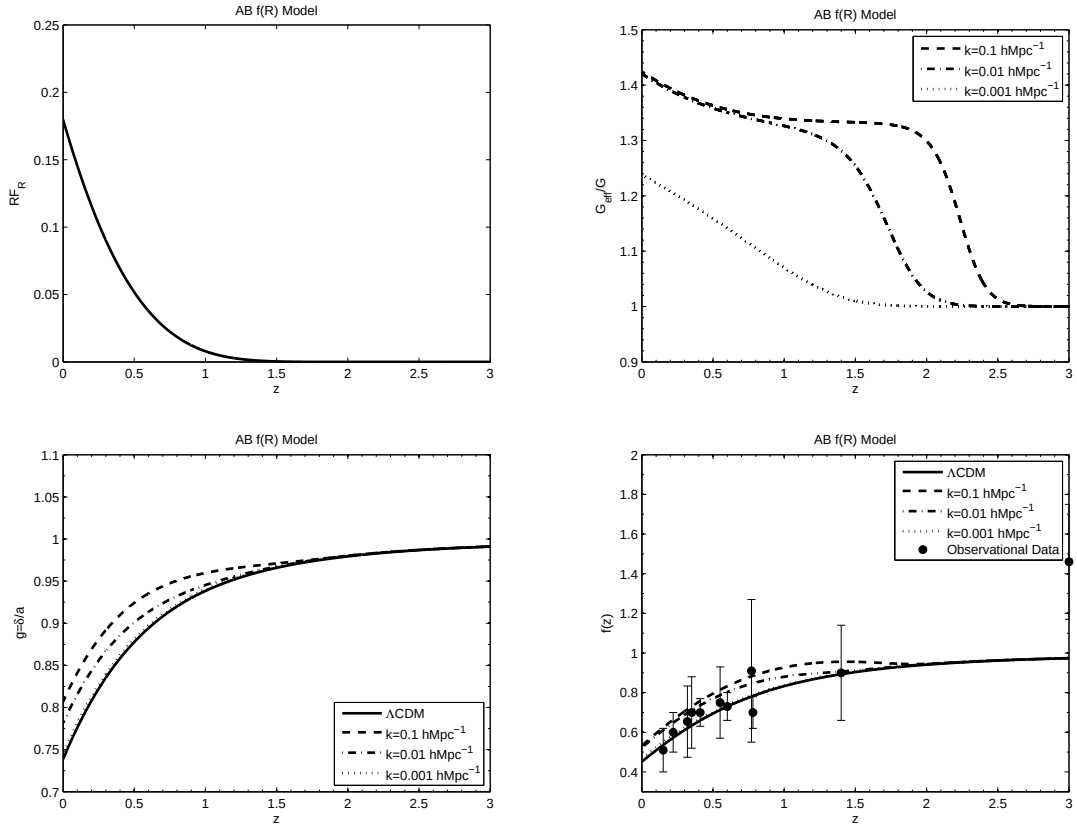

Figure 10: Same as Fig. 6 but for the AB model.

Table 1: The observational data for the linear growth rate $f_{\rm obs}(z)$.

z	0.15	0.22	0.32	0.35	0.41	0.55	0.60	0.77	0.78	1.4	3.0
$f_{\rm obs}$	0.51	0.60	0.654	0.70	0.70	0.75	0.73	0.91	0.70	0.90	1.46
1σ	0.11	0.10	0.18	0.18	0.07	0.18	0.07	0.36	0.08	0.24	0.29
Ref.	[107]	[110]	[111]	[112]	[110]	[113]	[110]	[114]	[110]	[115]	[116]

8 Conclusions

Here, we investigated the evolution of both matter density fluctuations and GSL in some viable $f(R)$ models containing the Starobinsky, Hu-Sawicki, Exponential, Tsujikawa and AB models. For the aforementioned models, we first obtained the evolutionary behaviors of the Hubble parameter, the Ricci scalar, the deceleration parameter, the matter and DE density parameters, the EoS parameters and the GSL. Then, we explored the growth of structure formation in the selected $f(R)$ models. Our results show the following.

(i) All of the selected $f(R)$ models can give rise to a late time accelerated expansion phase of the universe. The deceleration parameter for all models shows a cosmic deceleration $q > 0$ to acceleration $q < 0$ transition. The present value of the deceleration parameter takes place

in the observational range. Also, at late times ($z \to -1$), it approaches a de Sitter regime (i.e. $q \to -1$), as expected.

(ii) The effective EoS parameter $\omega_{\rm eff}$ for the all models starts from the matter dominated era, $\omega_{\rm eff} \simeq 0$, and in the late time, $z \to -1$, it behaves like the ΛCDM model, $\omega_{\rm eff} \to -1$.

(iii) The evolution of the EoS parameter of DE, $\omega_{\rm D}$, shows that the crossing of the phantom divide line $\omega_D = -1$ appears in the near past as well as farther future. This is a common physical phenomena to the existing viable $f(R)$ models and thus it is one of the peculiar properties of $f(R)$ gravity models characterizing the deviation from the ΛCDM model [101].

(iv) The GSL is respected from the early times to the present epoch. But in the farther future, the GSL for the all models is violated in some ranges of redshift. The physical reason why the GSL does not hold in the farther future is that the sign of $\ddot{F}$ changes from positive to negative due to the dominance of DE over non-relativistic matter.

(v) For all models, the screened mass function $G_{\rm eff}/G$ is larger than 1 and in high z regime goes to 1. The deviation of $G_{\rm eff}/G$ from unity for larger k (smaller structures) is greater than the smaller k (larger structures). The modification of GR in the framework of $f(R)$-gravity gives rise to an effective gravitational constant, $G_{\rm eff}$, which is time and scale dependent parameter in contrast to the Newtonian gravitational constant.

(vi) The linear density contrast relative to its value in a pure matter model, $g(a) = \delta_{\rm m}/a$, for all models starts from an early matter-dominated phase, $g(a) = 1$, and decreases during history of the universe.

(vii) The evolutionary behavior of the growth factor of linear matter density perturbations, $f(z)$, shows that for all models, the growth factor for smaller k (larger structures) like the ΛCDM model fits the data very well.

It is worth noting that the $f(R)$-gravity for very small wavenumbers (larger structures) is completely indistinguishable from ΛCDM. The main effect of the $f(R)$ theory is in quasi-linear regimes, large wavenumbers (smaller structures) where the growth rate has a strong scale dependence and deviates from the standard ΛCDM case. Also, for any given wavenumber corresponding to the larger/smaller structures, the $f(R)$ model can have a growth function identical to Λ's at high redshift. Future surveys of the large scale structure such as eBOSS, DESI, Euclid, or WFIRST [26] may reveal the growth index in terms of wavenumber of the structures and help the $f(R)$-gravity models to be clearly distinguished from the ΛCDM model.

References

[1] M. Kowalski, et al., (Supernova Cosmology Project), Astrophys. J. **686**, 749 (2008).

[2] E. Komatsu, et al., (WMAP Collaboration), Astrophys. J. Suppl. **192**, 18 (2011).

[3] G. Hinshaw, et al., (WMAP Collaboration), Astrophys. J. Suppl. **208**, 19 (2013).

[4] P.A.R. Ade, et al., (Planck Collaboration), Astron. Astrophys. **571**, A16 (2014).

[5] M. Tegmark, et al., (SDSS collaboration), Phys. Rev. D **69**, 103501 (2004).

[6] D.J. Eisenstein, et al., (SDSS collaboration), Astrophys. J. **633**, 560 (2005).

[7] H. Lampeitl, et al., (SDSS collaboration), Mon. Not. Roy. Astron. Soc. **401**, 2331 (2009).

[8] T. Padmanabhan, Phys. Rep. **380**, 235 (2003).

[9] P.J.E. Peebles, B. Ratra, Rev. Mod. Phys. **75**, 559 (2003).

[10] C.G. Tsagas, A. Challinor, R. Maartens, Phys. Rept. **465**, 61 (2008).

[11] M. Li, et al., Commun. Theor. Phys. **56**, 525 (2011).

[12] T.P. Sotiriou, V. Faraoni, Rev. Mod. Phys. **82**, 451 (2010).

[13] A. De Felice, S. Tsujikawa, Living Rev. Relativ. **13**, 3 (2010).

[14] S. Nojiri, S.D. Odintsov, Phys. Rept. **505**, 59 (2011).

[15] S. Nojiri, S.D. Odintsov, Phys. Rev. D **68**, 123512 (2003).

[16] S.A. Appleby, R.A. Battye, A.A. Starobinsky, JCAP **06**, 005 (2010).

[17] H. Motohashi, A. Nishizawa, Phys. Rev. D **86**, 083514 (2012).

[18] A. Nishizawa, H. Motohashi, Phys. Rev. D **89**, 063541 (2014).

[19] Y. Sobouti, Astron. Astrophys. **464**, 921 (2007).

[20] S. Nojiri, S.D. Odintsov, Phys. Rev. D **74**, 086005 (2006).

[21] S. Nojiri, S.D. Odintsov, Phys. Lett. B **657**, 238 (2007).

[22] S. Nojiri, S.D. Odintsov, Phys. Rev. D **77**, 026007 (2008).

[23] K. Karami, M.S. Khaledian, JHEP **03**, 086 (2011).

[24] K. Karami, M.S. Khaledian, Int. J. Mod. Phys. D **21**, 1250083 (2012).

[25] A. Raccanelli, et al., Mon. Not. Roy. Astron. Soc. **436**, 89 (2013).

[26] D. Huterer, et al., Astropart. Phys. **63**, 23 (2015).

[27] M. Kunz, D. Sapone, Phys. Rev. Lett. **98**, 121301 (2007).

[28] E. Bertschinger, P. Zukin, Phys. Rev. D **78**, 024015 (2008).

[29] S. Baghram, S. Rahvar, JCAP **12**, 008 (2010).

[30] N. Mirzatuny, S. Khosravi, S. Baghram, H. Moshafi, JCAP **01**, 019 (2014).

[31] Y.S. Song, W. Hu, I. Sawicki, Phys. Rev. D **75**, 044004 (2007).

[32] T. Jacobson, Phys. Rev. Lett. **75**, 1260 (1995).

[33] R.G. Cai, S.P. Kim, JHEP **02**, 050 (2005).

[34] M. Akbar, R.G. Cai, Phys. Lett. B **635**, 7 (2006).

[35] M. Akbar, R.G. Cai, Phys. Lett. B **648**, 243 (2007).

[36] K. Karami, M.S. Khaledian, N. Abdollahi, Europhys. Lett. **98**, 30010 (2012).

[37] G. Izquierdo, D. Pavón, Phys. Lett. B **639**, 1 (2006).

[38] H. Mohseni Sadjadi, Phys. Rev. D **73**, 063525 (2006).

[39] H. Mohseni Sadjadi, Phys. Rev. D **76**, 104024 (2007).

[40] H. Mohseni Sadjadi, Phys. Lett. B **645**, 108 (2007).

[41] J. Zhou, et al., Phys. Lett. B **652**, 86 (2007).

[42] Y. Gong, B. Wang, A. Wang, Phys. Rev. D **75**, 123516 (2007).

[43] Y. Gong, B. Wang, A. Wang, JCAP **01**, 024 (2007).

[44] M. Jamil, M. Akbar, Gen. Relativ. Gravit. **43**, 1061 (2011).

[45] A. Sheykhi, B. Wang, Phys. Lett. B **678**, 434 (2009).

[46] A. Sheykhi, Phys. Rev. D **81**, 104011 (2010).

[47] N. Banerjee, D. Pavón, Phys. Lett. B **647**, 447 (2007).

[48] K. Karami, JCAP **01**, 015 (2010).

[49] K. Karami, S. Ghaffari, Phys. Lett. B **685**, 115 (2010).

[50] K. Karami, S. Ghaffari, Phys. Lett. B **688**, 125 (2010).

[51] K. Karami, S. Ghaffari, M.M. Soltanzadeh, Class. Quantum Grav. **27**, 205021 (2010).

[52] K. Karami, et al., JHEP **08**, 150 (2011).

[53] K. Karami, A. Abdolmaleki, JCAP **04**, 007 (2012).

[54] K. Karami, et al., Eur. Phys. J. C **73**, 2565 (2013).

[55] K. Karami, et al., Phys. Rev. D **88**, 084034 (2013).

[56] A. Abdolmaleki, T. Najafi, K. Karami, Phys. Rev. D **89**, 104041 (2014).

[57] N. Radicella, D. Pavón, Phys. Lett. B **691**, 121 (2010).

[58] K. Bamba, C.Q. Geng, JCAP **11**, 008 (2011).

[59] A.A. Starobinsky, Phys. Lett. B **91**, 99 (1980).

[60] H. Motohashi, A.A. Starobinsky, J. Yokoyama, Prog. Theor. Phys. **123**, 887 (2010).

[61] H. Motohashi, A.A. Starobinsky, J. Yokoyama, JCAP **06**, 006 (2011).

[62] S. Capozziello, et al., Int. J. Mod. Phys. D **12** 1969, (2003).

[63] S. Capozziello, V.F. Cardone, A. Troisi, Phys. Rev. D **71**, 043503 (2005).

[64] N.J. Poplawski, Phys. Lett. B **640**, 135 (2006).

[65] S. Capozzielo, et al., Astrophys. Space Sci. **342**, 155 (2012).

[66] V.F. Cardone, S. Camera, A. Diaferio, JCAP **02**, 030 (2012).

[67] T. Chiba, T. Nakamura, Prog. Theor. Phys. **100**, 1077 (1998).

[68] M. Visser, Class. Quantum Grav. **21**, 2603 (2004).

[69] M. Visser, Gen. Relativ. Gravit. **37**, 1541 (2005).

[70] A. Pradhan, et al., Astrophys. Space Sci. **337**, 401 (2012).

[71] R. Zheng, Q. Huang, JCAP **03**, 002 (2011).

[72] J.c. Hwang, H. Noh, Phys. Rev. D **71**, 063536 (2005).

[73] S. Tsujikawa, Phys. Rev. D **77**, 023507 (2008).

[74] A.A. Starobinsky, JETP Lett. **86**, 157 (2007).

[75] S. Tsujikawa, Phys. Rev. D **76**, 023514 (2007).

[76] S. Tsujikawa, K. Uddin, R. Tavakol, Phys. Rev. D **77**, 043007 (2008).

[77] E. Elizalde, et al., Eur. Phys. J. C **72**, 1843 (2012).

[78] K. Bamba, et al., Class. Quantum Grav. **30**, 015008 (2013).

[79] H. Motohashi, A.A. Starobinsky, J. Yokoyama, Int. J. Mod. Phys. D **18**, 1731 (2009).

[80] P.J.E. Peebles, *Principles of Physical Cosmology*, Princeton University Press (1993).

[81] T. Padmanabhan, *Structure formation in the universe*, Cambridge University Press (1993).

[82] B. Jain, J. Khoury, arXiv:1004.3294.

[83] J.D. Bekenstein, Phys. Rev. D **9**, 3292 (1974).

[84] R.M. Wald, Phys. Rev. D **48**, 3427 (1993).

[85] G. Cognola, et al., JCAP **02**, 010 (2005).

[86] L.P. Chimento, A.S. Jakubi, D. Pavón, Phys. Lett. B **508**, 1 (2001).

[87] P.C.W. Davies, T.M. Davis, C.H. Lineweaver, Nature **418**, 602 (2002).

[88] G. Izquierdo, D. Pavón, Phys. Lett. B **633**, 420 (2006).

[89] J.H. MacGibbon, Phys. Rev. Lett. **99**, 061301 (2007).

[90] Y.B. Wu, et al., Phys. Lett. B **717**, 323 (2012).

[91] L.G. Jaime, L. Patiño, M. Salgado, arXiv:1206.1642.

[92] W. Hu, I. Sawicki, Phys. Rev. D **76**, 064004 (2007).

[93] G. Cognola, et al., Phys. Rev. D **77**, 046009 (2008).

[94] K. Bamba, C.Q. Geng, C.C. Lee, JCAP **08**, 021 (2010).

[95] E. Elizalde, et al., Phys. Rev. D **83**, 086006 (2011).

[96] A.D. Dolgav, M. Kawasaki, Phys. Lett. B **573**, 1 (2003).

[97] V. Faraoni, Phys. Rev. D **74**, 104017 (2006).

[98] S. Tsujikawa, et al., Phys. Rev. D **80**, 084044 (2009).

[99] A. de la Cruz-Dombriz, A. Dobado, A.L. Maroto, Phys. Rev. Lett. **103**, 179001 (2009).

[100] H. Motohashi, A.A. Starobinsky, J. Yokoyama, Int. J. Mod. Phys. D **20**, 1347 (2011).

[101] K. Bamba, C.Q. Geng, C.C. Lee, JCAP **11**, 001 (2010).

[102] K. Bamba, C.Q. Geng, C.C. Lee, Int. J. Mod. Phys. D **20**, 1339 (2011).

[103] S.A. Appleby, R.A. Battye, Phys. Lett. B **654**, 7 (2007).

[104] S.A. Appleby, R.A. Battye, JCAP **05**, 019 (2008).

[105] S. Capozziello, et al., Phys. Rev. D **84**, 043527 (2011).

[106] N. Radicella, D. Pavón, Gen. Relativ. Gravit. **44**, 685 (2012).

[107] L. Verde, et al., Mon. Not. Roy. Astron. Soc. **335**, 432 (2002).

[108] E. Hawkins, et al., Mon. Not. Roy. Astron. Soc. **346**, 78 (2003).

[109] E.V. Linder, Astropart. Phys. **29**, 336 (2008).

[110] C. Blake, et al., Mon. Not. Roy. Astron. Soc. **415**, 2876 (2011).

[111] R. Reyes, et al., Nature **464**, 256 (2010).

[112] M. Tegmark, et al., Phys. Rev. D **74**, 123507 (2006).

[113] N.P. Ross, et al., Mon. Not. Roy. Astron. Soc. **381**, 573 (2007).

[114] L. Guzzo, et al., Nature **451**, 541 (2008).

[115] J. da Angela, et al., Mon. Not. Roy. Astron. Soc. **383**, 565 (2008).

[116] P. McDonald, et al., Astrophys. J. **635**, 761 (2005).

Iranian Journal of Astronomy and Astrophysics
Vol. 3, No. 2, Autumn 2016

Iranian Journal of Astronomy and Astrophysics

Formation of Large Structures in the Acceleration Universe with a Hybrid Expansion Law

Neda Amjadi · Vahid Abbasvand · D.M Jassur
Astrophysics Department, Physics Faculty, University of Tabriz, Tabriz, Iran

Abstract. In the current paper, we have studied the effect of dark energy on formation where dark energy exists in the background. For this purpose, we used both WMAP9 and Planck data to study how the radius changes with redshift in these models. We used different data sets to fix the cosmological parameters to obtain a solution for a spherical region under collapse. The mechanism of structure formation for dark and baryonic matter is different. When processed by gravitational instability, density perturbations have given rise to collapsed dark matter structures, called halos. These dark matter halos offer the backdrop for the subsequent formation of all collapsed baryonic structures, including stars, galaxies, and galaxy clusters. In Planck Data forΛCDM, with the presence of dark energy in the background, the formation of baryonic matter is delayed. Therefore, it is a factor for the largening of the baryonic matter radius. Accompanying dark energy is entailing an increment of dark matter virial radius. For WACDM Data, dark energy alongside time-dependent parameter of state and baryon acoustic oscillations are the reasons for the delay of dark matter formation and the radius reduction. Due to the lack of data without baryonic acoustic waves in the background, we are left unable to delineate its impact on the structures. In $WCDM(BAO+H_0)$ and $WCDM(H_0)$, the lack of BAO shows a critical role in the delaying of baryonic matter structure formation. Respectively, it causes growing virial radius of dark matter. BAO, without taking dark energy into accounts, is the reason for the increasing and decresing of radius of dark and baryonic matter. It also delays baryonic matter formation. In $\Lambda CDM(BAO+H_0)$ and $\Lambda CDM(H_0)$, We have studied ΛCDM data for standard model under two circumstances: (a) $\Lambda CDM(BAO+H_0)$, (b) $\Lambda CDM(H_0)$ data. Dark energy in this data delays formation and intensifies virial radius of baryonic matter. Our studies show WCDM andΛCDM have the same effect on formation if we do not consider dark energy in BG. Planck data, in comparing with WMAP, has important role in describing standard model.

Keywords: Dark Energy – Scalar Fields – Baryonic Acoustic Waves – Standard Model

1 Introduction

In 1998, two teams studying distant Type Ia supernovae presented independent evidence that our universe is currently accelerating [1, 2]. The physical origin of cosmic acceleration remains a deep mystery. The accelerated expansion of the Universe,discovered in 1998, has raised fascinating questions for cosmology and physics as a whole. Two different approaches are proposed for this problem: (i) Dark Energy models that modify the stress-energy content of the Universe, adding an additional component with equation of state w=-1. That is, we modify the right-hand side of the Einstein equations. (ii) The Modified Gravity category corresponds to modifying the left-hand side. For example General Relativity (GR) by modifying the Einstein-Hilbert action [3, 4, 5].

The candidates of dark energy include cosmological constant and a variety of scalar field models. The models based upon modified theories of gravity are faced with the challenges posed by the local physics. Large scale modification of gravity essentially implicates extra degrees of freedom which might influence local physics where the Einstein theory of gravity is approving with observations. By giving a priori a cosmic history, specifying either the equation of state (EoS) or the scale factor $''a''$, we can always construct a scalar field potential which would imitate the desired result. Similar reconstruction can be executed in scalar tensor theories [6, 7].

The dynamics of realistic Universe are illustrated by an EoS parameter which behaves differently at different epochs. For instance, in general relativistic description of the dynamics of the spatially flat RW space-time, the fluids with constant EoS parameter $w > -1$ give rise to a power-law expansion ($a \propto t^{\frac{2}{3(1+w)}}$) of the Universe and for an exponential expansion $a \propto e^{kt}$, where $k > 0$ is a constant; it is required that $w = -1$. The solution of the Einstein's field equation in the presence of a single fluid with a constant EoS parameter gives a relation for the EoS parameter of a fluid. The discovery of cosmic acceleration is debatably one of the most important developments in modern cosmology [8, 9].

Most dark energy modelling using scalar fields has followed the Quintessence pattern of a slowly rolling canonical scalar field. However, there has been increasing interest in loosening the assumption of a canonical kinetic term. In its most general form, this idea is known as k-essence [10].

Tachyon dark energy has been explored by many authors, e.g.[6, 11, 12]. Bagla et al (2003) focused on two specific choices of Tachyon potential, and carried out numerical analysis of the cosmological evolution in order to constrain them against supernova data and the growth rate of large-scale structure [6]. Copeland et al (2005) studied a wider range of potentials, concentrating mainly on analytical inspection of attractor behavior and the critical point structure without making comparison to specific observations [12]. By studying a wide range of potentials and testing them directly against current observational constraints, they aim to combine some of the positive features of each analysis [13].

Parsons and Barrow studied the behavior of the scale factor in the context of inflation in the early Universe [14]. They pointed out that Einstein's field equations in the presence of self-interacting scalar field are invariant under the constant rescaling of the scalar field, and then they generated the HEL (Hybrid Expansion Law) behavior from power-law expansion. They also showed that such an expansion of the Universe can be represented as a Friedmann Universe in the presence of imperfect fluid. Akarsu et al (2014) study HEL expansion in the context of the history of the Universe after the inflation took place, and mainly investigate whether this law could be used for explaining the evolution of the Universe starting from the radiation- or matter-dominated Universe to the currently accelerating Universe. They also carried out the effective fluid and the single scalar field reconstruction using Quintessence, Tachyon and Phantom fields, which can capture HEL in the framework of general relativity [15].

In cosmology, baryon acoustic oscillations (BAO) refers to regular, periodic fluctuations in the density of the visible baryonic matter (BM) of the Universe. BAO matter clustering provides a $''standardruler''$for length scale in cosmology in the same way that supernova experiments provide a $''standardcandle''$ for astronomical observations. BAO measurements help cosmologists understand the nature of dark energy better by constraining cosmological existing BAO in the background [15].

The effect of the dynamics of dark energy on the growth rate of the large scale structures in the framework of LCDM and MOND is investigated. For variable dark energy model, increasing the bending parameter b causes the structure viralizes at lower redshift with

larger radius. Therefore, the variable dark energy model put off the spherical collapse to the later times. The case of the low-density model has an intermediate behavior such that the virialization redshift in this model corresponds with b = 0.4 in variable dark energy model. Finally, we compared the virialization of structures under the variable dark energy model with the recent results of MONDian N-body simulations. We showed that the various models of simulation are consistent with the variable dark energy model with different bending parameter [16, 17].

The process of the structure formation in the presence of dark energy models must be studied linear theory in order to address the growth of structures in linear regime and the effect of dark energy on matte power spectrum and variance, which is then, must be used in Press- Schechter kind of study of the nonlinear structures [18]. There is ample evidence that galaxies reside in extended halos of dark matter(DM) which forms through gravitational instability. Density perturbations grow linearly until they reach a critical density, after which they turn around from the expansion of the Universe and collapse to form virialized dark matter halos. These halos continue to grow in mass and size, either by accreting material from their neighborhood or by merging with other halos. Some of these halos may survinve as bound entities after merging into a bigger halo, thus giving rise to a population of subhalos. The illustrated process shows the formation of a dark matter halo in a numerical simulation of structure formation in a CDM cosmology. It also shows how a small volume with small perturbations initially expands with the Universe. As time proceeds, small-scale perturbations grow and collapse to form small halos. At a later stage, these small halos merge together to form a single virialized DM halo with an ellipsoidal shape, which reveals some substructure in the form of DM subhalos[19].

Within this paper, we intend to investigate whether a simple scale factor obtained by multiplying power-law and exponential law, which we will call hybrid expansion law, could triumph in explaining the observed Universe. We have used scalar fields for investigating structures formation and the effect dark energy has on it.

Here follows the outline: In Sec. 2, we will inspect the potential and EoS in scalar fields such as Quintessence, Tachyon and Phantom. In Sec. 3, we will exhibit how the presence of dark energy affects structure formation by using Planck, WACDM, and WCDM data. We will finalize the paper summarizing the results in the conclusion section.

2 Scalar fields

Scalar field models have played a vital role in cosmological studies for nearly half a century. Those assumed scalar fields have appeared in different cosmological research aspects to resolve various cosmological problems [21], such as driving inflation, time variable cosmological constant explaination, and so on. The scalar fields have played one other essential role for the past fifteen years as a candidate for dark energy proceeding the discovery of the accelerating expansion of universe. There are so many phenomenological dark energy models of scalar fields, such as Quintessence, Phantom, quintom and the scalar fields with non-canonical kinetic energy term [22, 23].

To study the dynamical evolution of those scalar field models and their cosmological implications with a phase-plane analysis is a very useful and common method. However, most studies only focus on the Quintessence models (including Phantom, Quintessence, and quintom) with unique exponential potential and Tachyon models (including Phantom Tachyon) with inverse square potential. Correspondingly, the dynamical systems are two dimensional autonomous systems with those particular forms of potentials [24, 25].

2.1 Quintessence field

Most cosmological models implicitly assume that matter and dark energy interact only gravitationally. In the absence of an underlying symmetry that would suppress a matter-dark energy coupling (or interaction), there is no a priori reason for dismissing it. Cosmological models in which dark energy and matter do not evolve separately but interact with one another were first introduced to justify the small value of the cosmological constant [26]. Recently, various proposals at the fundamental level, including field Lagrangians, have been advanced to account for the coupling. Scalar field Lagrangians coupled with matter do not generate scaling solutions with a long enough DM dominated period as required by structure formation. The phenomenological model we are going to discuss was constructed to account for late acceleration in the framework of Einstein's relativity and to significantly alleviate the mentioned coincidence problem and escapes the limits imposed by it[27, 28].

Most of the dark energy studies are carried out within the Quintessence pattern of a slowly rolling canonical scalar field with a potential. For that reason, we will first consider the Quintessence realization of the HEL. In general relativity, the effective energy density and EoS parameter of the fluid follow as below [20]:

$$\rho_{eff}(t) = 3(\frac{\alpha}{t} + \frac{\beta}{t_0})^2 \tag{1}$$

$$W_{eff} = \frac{2}{3}\frac{\alpha}{t^2}(\frac{\alpha}{t} + \frac{\beta}{t_0})^{-2} - 1 \tag{2}$$

The potential and EoS parameter as a function of time (t) are then given by the following expression:

$$\dot{\phi}^2(t) = \frac{2\alpha}{t^2} \tag{3}$$

$$V(t) = 3(\frac{\alpha}{t} + \frac{\beta}{t_0})^2 - \frac{\alpha}{t^2} \tag{4}$$

$$W(t) = \frac{\frac{2\alpha}{t^2}}{3(\frac{\alpha}{t} + \frac{\beta}{t_0})^2} - 1 \tag{5}$$

2.2 Tachyon field

Quintessence pattern relies on the potential energy of scalar fields to drive the late time acceleration of the Universe. On the other hand, it is also possible to relate the late time acceleration of the Universe to the kinetic term of the scalar field by relaxing its canonical kinetic term. This idea is known as k-essence [29]. Tachyon fields can be taken as a particular case of k-essence models with Dirac-Born-Infeld (DBI) action and can also be motivated by the string theory [30]. That item together with $p = w\rho$, give the following relations:

$$\dot{\phi}^2 = \frac{\frac{2\alpha}{t^2}}{3(\frac{\alpha}{t} + \frac{\beta}{t_0})^2} \tag{6}$$

$$V(t) = 3(\frac{\alpha}{t} + \frac{\beta}{t_0})^2\sqrt{1 - \frac{\frac{2\alpha}{t^2}}{3(\frac{\alpha}{t} + \frac{\beta}{t_0})^2}} \tag{7}$$

$$w = \frac{\frac{2\alpha}{t^2}}{3(\frac{\alpha}{t} + \frac{\beta}{t_0})^2} - 1 \tag{8}$$

2.3 Phantom field

Quintessence and Tachyon fields investigated in the previous two subsections can yield EoS parameters $w \geq -1$. However, present observations allow slight Phantom values for the EoS parameter, i.e., $w < -1$. Sources behaving as a Phantom field can arise in braneworlds, Brans-Dicke scalar-tensor gravity and may be motivated by S-brane constructions in the string theory [15, 20]. On the other hand, the Phantom energy can, in general, be simply described by a scalar field with a potential $V(\phi)$ like the Quintessence dark energy, yet with a negative kinetic term [31]. Accordingly, the energy density and pressure of the Phantom field can be given by

$$\rho = -\frac{1}{2}\dot{\phi}^2 + V(\phi) \tag{9}$$

$$P = -\frac{1}{2}\dot{\phi}^2 - V(\phi) \tag{10}$$

where ϕ is the Phantom field with potential $V(\phi)$. We rescale time as $t \longrightarrow t_s - t$, where t_s is a sufficiently positive reference time. Thus, the HEL ansatz [1] becomes

$$a = a_0(\frac{t_s - t}{t_s - t_0})^{\alpha} e^{[\beta(\frac{t_s - t}{t_s - t_0} - 1)]} \tag{11}$$

The effective EoS parameter and energy density ρ are respectively:

$$\rho_{eff}(t) = 3(\frac{\alpha}{t_s - t} + \frac{\beta}{t_s - t_0})^2 \tag{12}$$

$$w_{eff} = \frac{2}{3}\frac{\alpha}{(t_s - t)^2}(\frac{\alpha}{t_s - t} + \frac{\beta}{t_s - t_0})^{-2} - 1 \tag{13}$$

Thus, we can get following equations from Eqs $(14 - 18)$:

$$\dot{\phi}^2 = \frac{-2\alpha}{(t_s - t)^2} \tag{14}$$

$$V(t) = 3(\frac{\alpha}{t_s - t} + \frac{\beta}{t_s - t_0})^2 - \frac{\alpha}{(t_s - t)^2} \tag{15}$$

$$w = \frac{\frac{2\alpha}{(t_s - t)^2}}{3(\frac{\alpha}{t_s - t} - \frac{\beta}{t_s - t_0})^2} \tag{16}$$

where α and β are non-negative constants ($\alpha = 0.488, \beta = 0.444$).

3 Results & Discussion

In the current paper, we have investigated scalar field models for ansatz that are produced with power-law and exponential type of functions. We have also carried out the evolution of large scale structures in a single scalar field reconstruction using Quintessence, Tachyon and Phantom fields and compared them with the standard model (ΛCDM). Following that purpose, we have applied dark energy effect on formation. We have used two numerical data, namely WMAP9 and Planck to study how the radius changes with redshift in these models. It helps us obtain virilization of models, which agrees to structure formation in Cosmological observations. Results are regularized in three subsections. First, we will investigate Planck data first, then WACDM and finally WCDM.

3.1 Planck Data

Cosmological observations prior to Planck were consistent with the simplest models of inflation within the slow-roll paradigm. Planck data are remarkably consistent with the predictions of the base ΛCDM cosmology. In the following section, we will use Planck numerical data [33] to investigate dark energy effect on structure formation in background under two circumstances: (a) radiation and matter(dark and light separately), (b) radiation, matter and dark energy , in the BG.

Since the HEL model predicts the beginning of universe with radiation and the current accelerating phase of the universe at the same time. However, from the CMB test it does not accommodate the matter-dominated era properly unless we consider the parameter α. Thus, with the current form of HEL, radiation alone cannot construct structure [15].

According to Newton's gravity law, the radius of dark and baryonic matter can be given by

$$\begin{aligned} \frac{dr_b}{da} &= \frac{1}{aH((-r_b^2H^2\delta_b + \frac{2GM}{r_b})^{-\frac{1}{2}})} \\ \frac{dr_d}{da} &= \frac{1}{aH((-3r_d^2H^2\delta_d + \frac{2GM}{r_d})^{-\frac{1}{2}})} \end{aligned} \tag{17}$$

Where $a_0 = 1$ and δ is matter density contrast. Now using Planck data [32, 33] and Harrison-Zeldovich spectrum data [16], we obtain numerical data that shows in Tab.1.

In the other case, Friedmann equation encompasses radiation, matter and energy. There, the numerical value of Planck data is placed in ΛCDM and scalar field models follow as Tab.1.

We plotted radius evolution of scalar fields and ΛCDM models in Fig.1 by considering the values of model parameters given in Table 3 from Planck data. According to virial theorem, when the kinetic energy of structure abates, the total energy becomes potential energy. In this phase, the structure spends its maximum radius. For comparison, all of the models are in a plot which shows all models have similar behavior for DM. In other words, Planck data are compatible with the predictions of the base ΛCDM cosmology. By using this data, standard model can be explained as structure formation. Hence, dark energy in the background makes a delay in formation of BM and intensifies its radius. Accompanying the existence of dark energy is entailing an intensification of DM virial radius. For scalar field models, dark energy is a factor to the accretion of DM radius. However, BM cannot be constructed with such data.

Table 1: The mass of baryonic and DM ($10^{12}M_{\odot}$) with radiation and dark energy in background in three models. Using Planck numerical data to investigate dark energy effect on structure formation in background under two circumstances (a) and (b).

	$Model$	Com	$R_{Max}(Kpc)$	$R_{vir}(Kpc)$	Z_{Max}	Z_{vir}
a	Plank	DM	156.268±2.315	81.809±1.404	5.7±0.020	3.4±0.012
		BM	467.657±4.428	250.161±2.705	1.3±0.007	0.45±0.001
b	ΛCDM	DM	156.263±2.315	83.247±1.407	5.7±0.020	3.4±0.012
		BM	467.750±4.429	251.441±2.709	1.25±0.007	0.35±0.001
b	Phantom	DM	156.263±2.315	83.247±1.407	5.7±0.001	3.4±0.012
		BM	421.7±4.421	421.7±4.421	2.05±0.009	2.05±0.009
b	Tachyon &	DM	156.263±2.315	83.247±1.407	5.7±0.020	3.4±0.012
	Quintessence	BM	422.494±4.429	422.494±4.429	2.05±0.009	2.05±0.009

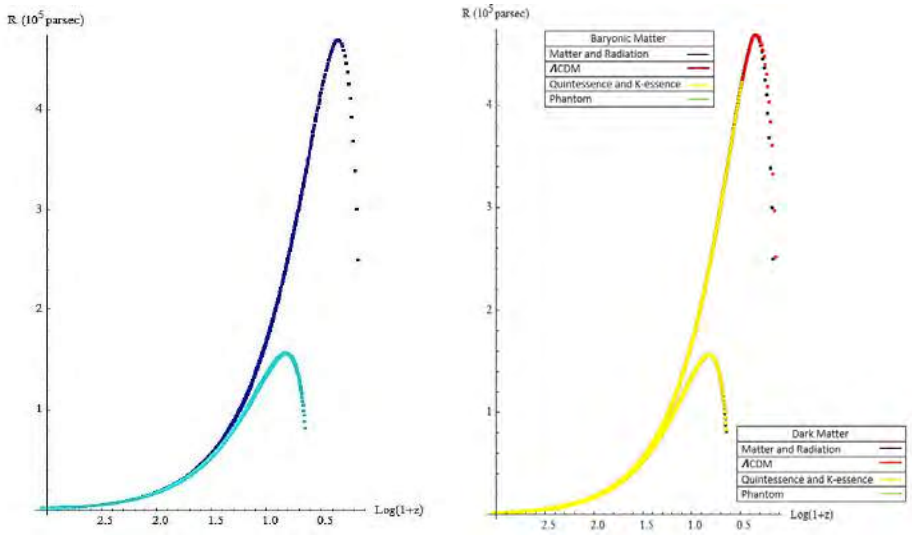

Figure 1: Left: Radial evolution of BM (dark blue) and DM (light blue) for mass = $10^{12}M_{\odot}$ from Planck Data. In this model, radiation and matter exist in background. Right: Diagrams show radial evolution of BM and DM for ΛCDM model (red), Phantom model (green), Tachyon and Quintessence models (yellow). Black curve shows matter and radiation in background. Dots relate virialization of model. In BM, this compatible is interrupted for $\log\,(1+Z) < 0.5$.

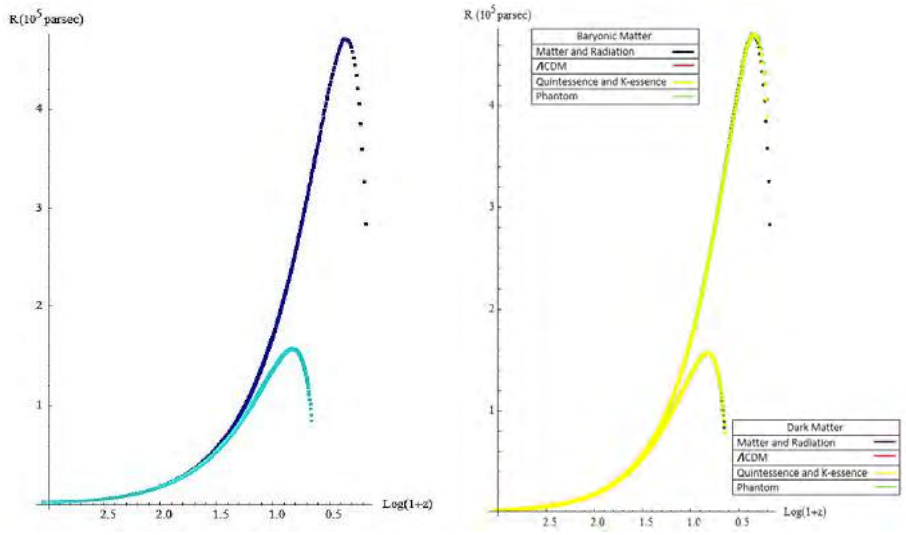

Figure 2: The same as in Figure 1 but by using WACDM Data. Black curve shows matter and radiation in background. Dots relate virialization of model.

3.2 WACDM Data

A major challenge for cosmology today is to elucidate the nature of the dark energy driving the accelerated expansion of the Universe. Among cosmological models, there is one that depicts flat universe with dark energy where equation of state is time-dependent. Scalar field models are time-dependent. Therefore, we analyzed redshifts in which parameter of state has a negative value. For Tachyon and Quintessence models, this value is $z < 2.273$. However, in the case of the Phantom scenario, the ansatz and Hubble parameter diverge as $t \longrightarrow t_s$, and thus expose the Universe to Big Rip. We supposed that in flat universe, radiation, matter and energy exist in the background. Tab.2 shows numerical data that is given from WACDM data.

Table 2: The same as in Table 1 but by using WACDM Data.

	Model	*Comp*	$R_{Max}(Kpc)$	$R_{vir}(Kpc)$	Z_{Max}	Z_{vir}
a	Scalar	DM	157±2.316	84.087±1.410	5.74±0.020	3.44±0.012
	field	BM	469.245±4.431	283.47±3.070	1.34±0.007	0.49±0.001
b	Phantom	DM	157±2.316	78.914±1.397	5.74±0.020	3.39±0.011
		BM	470.181±4.432	406.64±4.360	1.24±0.007	0.59±0.001
b	Tachyon &	DM	157±2.316	78.914±1.397	5.74±0.020	3.39±0.011
	Quintessence	BM	469.967±4.431	388.905±4.115	1.29±0.007	0.59±0.001

Since DM is constructed earlier than BM, for investigating dark energy effect on structure, we compare redshift virilism with a state wherein energy is not in the background. Our study shows that dark energy alongside time-dependent parameter of state and baryon acoustic oscillations. These are the factor for the reducing of DM radius. Due to lack of data on the absence of baryonic acoustic waves in the background, we are left unable to delineate its impact on the structures. The absence mentioned is on the account of the simultaneous existence of dark energy and BAO in the background.

3.3 WCDM Data

WCDM data has investigated flat universe with dark energy by observing the effect of baryon acoustic oscillations. The BAO angular scale serves as a standard ruler and allows us to map out the expansion history of the Universe after last scattering. The BAO scale, which is extracted from galaxy redshift surveys, provides a constraint on the late-time geometry and breaks degeneracies with other cosmological parameters.

3.3.1 $WCDM(BAO + H_0)\&WCDM(H_0)$

Within the following subsection, first, we studied WCDM data for scalar fields under two circumstances: (a) WCDM (H_0+BAO), (b) WCDM (H_0) data then, inspected the presence of dark energy in the background. Tab.3 , Tab.4 and Fig.3 show numerical data that is given from WCDM data.

Table 3: The same as in Table 1 but by using WCDM($H_0 + BAO$) Data.

	$Model$	Com	$R_{Max}(Kpc)$	$R_{vir}(Kpc)$	Z_{Max}	Z_{vir}
a	Scalar	DM	156.783±2.317	81.955±1.405	5.71±0.020	3.41±0.012
	field	BM	469.13±4.430	255.459±2.715	1.31±0.007	0.46±0.001
b	Phantom	DM	156.778±2.317	83.553±1.408	5.71±0.020	3.41±0.012
		BM	469.056±4.430	466.667±4.427	1.26±0.006	1.01±0.005
b	Tachyon &	DM	156.778±2.317	83.553±1.408	5.71±0.020	3.41±0.012
	Quintessence	BM	468.786±4.429	464.351±4.421	1.31±4.421	1.01±0.005

Table 4: The same as in Table 1 but by using WCDM(H_0) Data.

	$Model$	Com	$R_{Max}(Kpc)$	$R_{vir}(Kpc)$	Z_{Max}	Z_{vir}
a	Scalar	DM	157.337±2.318	81.578±1.403	5.8±0.022	3.45±0.012
	field	BM	470.402±4.432	281.74±2.773	1.35±0.007	0.5±0.001
b	Phantom	DM	157.374±2.318	85.616±1.411	5.75±0.021	3.45±0.012
		BM	471.203±4.439	312.244±3.001	1.25±0.007	0.4±0.001
b	Tachyon &	DM	157.374±2.318	85.616±1.411	5.75±0.021	3.45±0.012
	Quintessence	BM	470.832±4.433	275.387±2.755	1.3±0.007	0.4±0.001

The presence of baryon acoustic oscillations plays a critical role in the postponing of dark and baryonic matter structure formation. Respectively, it causes increasing and decreasing virial radius of dark and baryonic matter. Dark energy, without taking BAO into accounts, is the reason for the declining of BM radius. If we consider both of them, we will be facing an increment of DM radius.

3.3.2 $\Lambda CDM(BAO + H_0)\&\Lambda CDM(H_0)$

Through this instance, we studied ΛCDM data for standard model under two circumstances: (a) $\Lambda CDM(BAO + H_0)$, (b) $\Lambda CDM(H_0)$ data. Then, we suppose that in flat universe, radiation, matter and energy exist in the background. Tab.5 and Fig.4 show this success.

Dark energy in this data grows virial radius of both of them. The structure formation in a standard model is dependent on BAO. In other words, BAO is a necessity factor for constructing structure in the standard model.

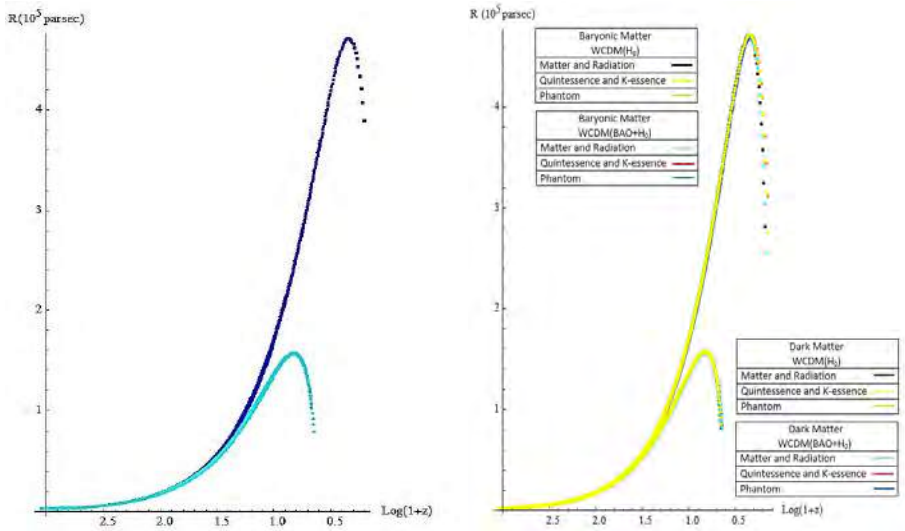

Figure 3: The same as in Figure 1 but by using Left: $WCDM(BAO + H_0)\&WCDM(H_0)$ Data. Right: $WCDM(BAO + H_0)\&WCDM(H_0)$ Data for Phantom, Tachyon and Quintessence models that radiation, matter and dark energy exist in background. Dots relate virialization of model.

Table 5: The same as in Table 1 but by using ΛCDMData.

	$Data$	Com	$R_{Max}(Kpc)$	$R_{vir}(Kpc)$	Z_{Max}	Z_{vir}
a	ΛCDM	DM	157.111±2.316	80.160±1.398	5.77±0.022	3.42±0.012
	$(BAO + H_0)$	BM	470.175±4.430	260.364±2.601	1.32±0.007	0.47±0.001
a	ΛCDM	DM	157.55±2.319	78.948±1.389	5.79±0.022	3.44±0.012
	(H_0)	BM	471.371±4.433	268.541±2.696	1.34±0.007	0.49±0.001
b	ΛCDM	DM	157.149±2.316	84.078±1.409	5.72±0.022	3.42±0.012
	$(BAO + H_0)$	BM	470.144±4.432	271.715±2.720	1.27±0.007	0.37±0.001
b	ΛCDM	DM	157.545±2.317	645.903±2.544	5.79±0.021	-1.91±0.001
	(H_0)	BM	471.203±4.431	914.531±10.117	1.29±0.007	-1.91±0.001

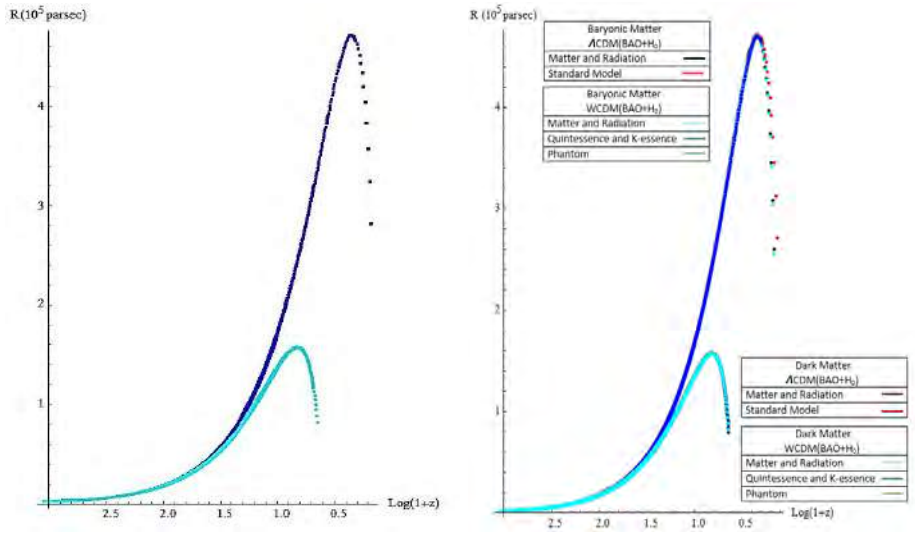

Figure 4: The same as in Figure 1. Left:$\Lambda CDM(BAO + H_0)$&$\Lambda CDM(H_0)$ Data. Right: ΛCDM Data.

4 Conclusion

In this paper, We have examined the hybrid form of scale factor, namely, a product of power law and an exponential function, which provides a simple mechanism of transition from decelerating to accelerating phase. Two numerical data are utilized to study how the radius of structures can remark in these models, as the virialization of structures depends strongly on the background. We used different data sets to fix the cosmological parameters to get a solution for a spherical region under collapse. We dealt with the problem of the structure formation in the framework of Cosmological Models under the influence of dark energy and BAO.

The mechanism of structure formation for DM and BM is different. Due to hierarchical structure formation, because of gravitational instability, density perturbations have given rise to collapsed DM structures, is called halos. These DM halos provide the backdrop for the subsequent formation of all collapsed baryonic structures, including stars, galaxies, and galaxy clusters.

We showed that the dark energy dominated background delays the virialization of structures and formation of BM which proceeds a larger structures. In other word, it causes an increase of virial radius of DM without deferment. Using Planck data in scalar field models shows that dark energy is an element to the intensification of dark matter radius. However, BM cannot be constructed with such data. Our study on WACDM data shows that the presence of dark energy alongside time-dependent parameter of state and baryon acoustic oscillations are shrinking reasons of radius for DM and absence of structure for BM. Due to lack of data on the absence of baryonic acoustic waves in the background, we are left unable to delineate its impact on the structures.

Finally on WCDM data, the presence of baryon acoustic oscillations plays an influential role in postponing. In turn, it causes decrease and increase to virial radius of dark and baryonic matter and the absence of BAO delays formation and abates virial radius of BM. The structure formation in a standard model is dependent on BAO. WCDM and ΛCDM have the same effect on formation if we do not consider dark energy in BG. Planck data, in

comparing with WMAP, has important role in describing standard model.

Acknowledgment

The WMAP mission is made possible by the support of the NASA Science Mission Directorate. This research has made use of NASA's Astrophysics Data System Bibliographic Services.

References

[1] Riess et al. 1998, The Astronomical, 116, 1009

[2] Perlmutter et al. 1999, The Astronomical, 517, 565

[3] Frieman J.A., Turner M.S. and Huterer D. 2008, Annual Review of Astronomy and Astrophysics, 46, 385

[4] Sami M. 2009, Current Science, 97, 887

[5] Nojiri Sh. and Odintsov S.D. 2011, Physics Reports, 505, 59

[6] Bagla J.S., Jassal H.K. and Padmanabhan T. 2003, Physical Review D, 67, 11

[7] Kamenshchik A.Yu., Tronconi A., Venturi G. and Vernov S.Yu. 2011, Physics Letters B, 702, 191

[8] Zeldovich Ya.B. 1962, SOVIET PHYSICS JETP, 14, 1609

[9] Barrow J.D. 1978, Nature, 272, 211

[10] Armendariz-Picon C., Mukhanov V. and Steinhardt P.J. 2000, Physical Review Letters, 85, 4438

[11] Garousi M.R., Sami M. and Tsujikawa Sh. 2004, Physical Review D, 70, 15

[12] Copeland J., Garousi M.R., Sami M., Tsujikawa Sh. 2005, Physical Review D, 71,

[13] Wang Yun. and Mukherjee Pia. 2006, Astrophysical Journal, 650, 1

[14] Parsons P. and Barrow J.D. 1995, Classical and Quantum Gravity, 12, 1715

[15] Akarsu O. et al. 2014, Cosmology and Astroparticle Physics, 2014, 18

[16] Malekjani M., Rahvar S. and Jassur D.M. 2009, New Astronomy, 14, 398

[17] Malekjani M., Rahvar S. and Haghi H. 2009, ApJ, 694, 1220

[18] Amendalo L. and Tsujikawa Sh. 2010, Cambridge University press, chapter 11-12

[19] Houjun Mo, Bosch F., and White S. The book" Galaxy Formation and Evolution" Cambridge University press 2010

[20] Eisenstein D.J. 2005, New Astronomy Reviews, 49, 360

[21] Ratra B. and Peebles P.J.E. 1988, Physical Review D, 37, 3406

[22] Copeland E.J., Sami M. And Tsujikawa S. 2006, International Journal of Modern Physics D, 15, 1753

[23] Li. Miao et al. 2011, Communications in Theoretical Physics, 56, 525

[24] Coley A.A. 2003, 291 Kluwer Academic Publishers

[25] Wei F. and Hui-Qing Lu. 2010, European Physical Journal C, 68, 5677

[26] Wetterich C. 1988, Nuclear Physics B, 302, 668

[27] Chimento L.P., Jakubi A.S., avn D. and Zimdahl PW. 2003, Physical Review D, 67, 29

[28] Amendola L., Quartin M., Tsujikawa S. and Waga I. 2006, Physical Review D, 74, 14

[29] Armendariz-Picon C., Mukhanov V. and Steinhardt P.J. 2000, Physical Review Letters, 85, 4438

[30] Gibbons G.W. 2002, Physics Letters B, 537, 1

[31] Caldwell R.R. 2002, Physics Letters B, 545, 23

[32] Planck Collaboration and Ade P.A.R., Aghanim N., Armitage-Caplan C., Arnaud M., Ashdown M., Atrio-Barandela F., Aumont J., Baccigalupi C. and Banday A.J. et al. 2014, Astronomy & Astrophysics, 571

[33] WMAP Cosmological Parameters Model, LAMBDA-Data Products , http://lambda.gsfc.nasa.gov/, NASA.

Iranian Journal of Astronomy and Astrophysics
Vol. 3, No. 2, Autumn 2016

Iranian Journal of Astronomy and Astrophysics

DASTWAR: A Tool for Completeness Estimation in Magnitude-size Plane *

*Source of DASTWAR software can be requested by sending e-mail to authors.

Ali Koohpaee[1] · Mehdi Khakian Ghomi[2]

[1] Department of Energy Engineering and Physics, Amirkabir University of Technology, Tehran, Iran
email: akoohpaee@gmail.com

[2] Department of Energy Engineering and Physics, Amirkabir University of Technology, Tehran, Iran

Abstract. Today, great observatories around the world, devote a substantial amount of observing time to sky surveys. The resulted images are inputs of source finder modules. These modules search for the target objects and provide us with source catalogues. We sought to quantify the ability of detection tools in recovering faint galaxies regularly encountered in deep surveys. Our approach was based on completeness estimation in magnitude - size plane. The adopted method was incorporating artificial galaxies. We improvised a software that estimates completeness in a given interval of magnitude and size. The software generates artificial galaxies and iteratively inserts them to the source finder modules input image. Evaluating the ratio of the number of detected to the number of inserted artificial galaxies provides us with means to estimate completeness. Completeness estimation is helpful in selecting unbiased samples.

Keywords: Galaxies: structure, galaxies: size, magnitude

1 Introduction

The past two decades have seen the growing number of imaging surveys of the extragalactic sky. Deep field optical/NIR imaging surveys such as COSMOS [19], HUDF [1], CANDELS [16] and GOODS [14] have become the frontier of astronomical studies in various topics. Moreover, within the next few years, imaging surveys with unprecedented depth and area (e.g. LSST [18] and Euclid [21]) will take place.

Any imaging survey is restricted and biased in its sampling of the galaxy population by a number of selection effects (e.g. [10, 11, 17, 4]). The visibility of a particular galaxy depends both on its intrinsic properties (e.g. brightness, light profile, apparent scale size) and the nature of the survey imaging data (e.g. exposure time and sky brightness) [4].

When CCD is used in acquisition of imaging data, outcome images will be of digital type. Acquired images, after passing the process of data reduction, will be given to source finder modules. These modules will identify the sources targeted by the survey and provide us with their photometric and structural properties.

In the case of galaxies, surface brightness is seen to be a key factor in their detectability by source finder modules. Generally, galaxies with lower surface brightness are harder to detect [14, 2, 4]. However, detection is a complex process and surface brightness is not the only factor in determining the detectability of a particular galaxy. For instance, blending with other sources, image artefacts as well as structural properties such as morphological

type and position angle can be mentioned as factors playing a role in their detectability [3]. There is no strict low surface brightness threshold, above which, the detectability of galaxies is assured. We expect that, as the surface brightness of a particular galaxy decreases, the probability of its detection also reduces. Completeness parameter has been defined to quantify the probability of detection [29, 20, 31, 7]. This parameter is defined as the ratio of the number of detected objects to the total number of objects present in the image.

The prospect of forthcoming imaging surveys with unprecedented depth and area testifies to the significance of automated and efficient modules to evaluate their completeness. In this paper, we describe a software package which is improvised to estimate completeness of galaxy detection as a function of apparent magnitude and half-light radius. This paper is organized as follows. In section 2, the methodology of the software is described. Section 3 is devoted to the study of the usage and efficiency of software. Ultimately, summary will be presented in section 4.

2 Methods

We based the completeness estimation procedure on incorporation of artificial galaxies. The core of `DASTWAR`[1] is an IRAF script written in IRAF command language. The software generates artificial galaxies and iteratively inserts them to the source finder modules input image (cf. [29, 20, 14, 4, 6]). Next, it utilizes the source finder module to detect the inserted artificial galaxies. By comparing the extracted catalog to the catalog of artificial galaxies inserted to the input image, completeness would be estimated. Completeness is defined as the ratio of the number of extracted artificial galaxies to the number of artificial galaxies present in the image. `DASTWAR` performs completeness estimation as a function of apparent magnitude and half-light radius of artificial galaxies (e.g. [14, 2, 4]). Inserting artificial galaxies to the observed image preserves any observational artifacts and sky noise when quantifying the probability of detection [6].

The software makes use of `IRAF artdada` package for generating artificial galaxies [2]. This package has been widely used to simulate galaxies in deep images (e.g. [14, 4]). Simulated galaxies are of either early-type or late-type morphology, respectively obeying de Vaucouleurs [9] and Exponential [12] surface brightness laws. The package enables the generation of artificial galaxies in a given bin of apparent magnitude and half-light radius. The software makes use of `SExtractor` [3] as source finder module. `SExtractor` is the standard detecting tool in extracting galaxies based on deep optical/NIR images. `SExtractor` isolates sources in the image given as input, and carries out photometric and structural measurements. Also, a catalogue of detected sources along with their photometric and structural parameters is returned at the end.

The workflow of the procedure is depicted in Fig. 1. The procedure starts with obtaining the values of the input parameters and the input image, which are provided by the user (see Table 1). Next, the software initiates generating the simulated images. A simulated image is a modified version of the input image. This modified version is constructed by inserting the artificial galaxies to the input image. The software utilizes `IRAF artdata` package to produce artificial galaxies according to the prescriptions of the user indicated by values of input parameters. Among the parameters which could be set by the user are the number of artificial galaxies to insert, their apparent magnitude and half-light radius tolerance, their morphological distribution and their inclination tolerance (see Table 1). It should be noted that, the software would not modify the input image before inserting artificial galaxies.

[1] Dastwar (pronounced Dastoor in present day persian) is the persian word for adviser.
[2] ftp://iraf.noao.edu/iraf/docs/glos210b.ps.Z

Figure 1: Workflow of the software is illustrated (see text).

Hence, the user has to decide whether to mask real sources or to leave them intact in the input image.

A two-dimensional point spread function, provided by the user, will be convolved with artificial galaxies before inserting them to the input image. Artificial galaxies will be uniformly distributed throughout a subregion of the input image defined by the user. Also their apparent magnitude and half-light radius will be uniformly distributed in the apparent magnitude and half-light radius tolerances indicated by the user. For subsequent referencing, properties of the inserted artificial galaxies, including their positions, apparent magnitudes and half-light radii will be saved in a catalog.

The process of generating the simulated images is iterative. The outcome of each iteration is a single simulated image (see Fig. 2). The total number of iterations will be set by giving value to the appropriate parameter. Willing to end up with an adequate completeness estimation necessitates balance between the number of artificial galaxies in each simulated image and the total number of iterations. When sufficient number of simulated images are generated, software moves forward to the next step.

As a result of complex observing strategies which are at work in deep imaging surveys (e.g. dithering [22]), yielded images are not generally associated with flat edges. Also, these images normally result from stacking a number of slide images on top of one another. In consequence, the edges of the obtained images are usually indentated and a set of pixels in the image array are seen to have zero value. In such an image, the entire area is not covered by data. If user notifies the software of the partial data-coverage in the input image, a mask image will be created. It is an image with the same width and height as the input image, in which the partial area covered by data is indicated. This mask image will be multiplied with each of the simulated images. In this way, the analogy of the data-covered area in the input image and the simulated images is assured. If user has not warned about the partial data-coverage in the input image, software leaps to the next step.

Now, all is at hand to start source detection. For this task, `DASTWAR` makes use of `SExtractor` [3]. `SExtractor` will be executed on each of the simulated images based on the input parameters set by the user. Hence, for each simulated image, we will be provided by a catalog of detected sources along with their photometric and structural properties.

Amongst the measured quantities for each detected source is the pixel position of the center. These positions will be used to crossmatch the `SExtractor` provided catalog with the catalog of artificial galaxies inserted to each simulated image. The radius of crossmatch will be set by the user. An artificial galaxy is designated as recovered if centroid of a unique detected source falls within its circle of crossmatch. For each simulated image, recovered galaxies will be listed in a new catalogue. Each line of this catalogue represents an artificial galaxy which was successfully detected by `SExtractor`.

At this point, for each of the simulated images, two catalogs are at hand. The first one is the catalog of inserted artificial galaxies and the second one is the catalog of recovered artificial galaxies. By accumulating the catalogs of inserted artificial galaxies into one catalog, we end up in the master catalog of artificial galaxies. This master catalog enlists all of the artificial galaxies inserted to the set of simulated images. In the same manner master catalog of recovered artificial galaxies is constructed. The latter catalog embraces the list of all artificial galaxies which are already detected by the source finder module. Comparing these two master catalogs enable us to quantify the degree of completeness. `DASTWAR` estimates completeness as a function of artificial galaxies' apparent magnitude and half-light radius.

Table 1: Input parameters of DASTWAR are listed in this table. IRAF artdada package parameters are marked with star.

Parameter	Data Type	Description
nrun	int	Number of iterations
ngal	int	Number of galaxies generated in each iteration
xcormin	real	Minimum X coordinate of artificial galaxies
ycormin	real	Minimum Y coordinate of artificial galaxies
xcormax	real	Maximum X coordinate of artificial galaxies
ycormax	real	Maximum Y coordinate of artificial galaxies
magmin	real	Upper magnitude limit for artificial galaxies
magmax	real	Lower magnitude limit for artificial galaxies
minrad	real	Minimum half-light ratio of artificial galaxies
maxrad	real	Maximum half-light ratio to artificial galaxies
*efrac	real	Fraction of early-type galaxies
*axisrat	real	Minimum axis ratio for early-type galaxies
*srefrac	real	Late-type/early-type radius at a given magnitude
*abs	real	Absorption in edge-on late-type galaxies
inpimage	char	Input image name
wimage	char	Weight image name
psf	char	PSF image name
*poinoi	bool	Add Poisson noise?
*rad	real	Seeing radius/scale (pixels)
*psfar	real	Star/PSF axial ratio
*psfpa	real	Star/PSF position angle
*magzp	real	Magnitude zero point
*ccdgain	real	Gain
*ccdreadnoise	real	CCD Read noise
seconfig	char	Name of Sextractor configuration file
sennw	char	Name of Sextractor Neural network/weights file
separam	char	Name of Sextractor Parameter file
seconv	char	Name of Sextractor convolution kernel
dx_gal	int	X-range for coverage tests (artificial galaxies)
dy_gal	int	Y-range for coverage tests (artificial galaxies)
dx_sex	int	X-range for coverage tests (detected sources)
dy_sex	int	Y-range for coverage tests (detected sources)
magbin	int	Number of magnitude bins for completeness estimation
sizebin	int	Number of size bins for completeness estimation
covcheck	bool	Apply coverage checks?
crop	bool	Apply cropping?
clean	int	Delete additional files made?
pixsize	real	Image pixel scale (arcsec/pix)
maxdist_arcs	real	Cross-match radius (arcsec)
compoutput	char	Completeness matrix file name
*background	real	Default background
*nxc	int	Number of PSF centers per pixel in X
*nyc	int	Number of PSF centers per pixel in Y
*nxsub	int	Number of pixel subsamples in X
*nysub	int	Number of pixel subsamples in Y
*nxgsub	int	Number of galaxy pixel subsamples in X
*nygsub	int	Number of galaxy pixel subsamples in Y
*dyrange	real	Profile intensity dynamic range
*psfrange	real	PSF convolution dynamic range

Figure 2: Five examples of simulated images are shown in this figure. In the uppermost left mosaic, we have shown the input image and the remaining mosaics illustrate examples of simulated images. The input image is a 512 × 512 pixels cutout of v2.0 images of HST/ACS in southern GOODS field which is acquired in F850LP band.

Table 2: Five lines of DASTWAR's output file are given as example.

Label 1	Label 2	Magnitude	Half-light radius	Completeness	Detected	Inserted
31	10	20.95	0.9189	0.842105	32	38
31	11	21.05	0.9189	0.932203	55	59
31	12	21.15	0.9189	0.886364	39	44
31	13	21.25	0.9189	0.903846	47	52
31	14	21.35	0.9189	0.857143	48	56

As was noted earlier, galaxies will be uniformly distributed throughout a subregion of the input image that is defined by user. Occasionally, an inserted artificial galaxy would reside in a position too close to the edge of the image or edge of the data-covered area. In such instances, the light profile of the artificial galaxy may become cropped; a phenomenon which usually results in its erroneous detection. When user warns `DASTWAR` of the possibility of existence of such sources, software attempts to identify them. This is done by defining a rectangular mask for each artificial galaxy, width and length of which is to be determined by the user. Center of this mask will be coincided to the center of each of the inserted artificial galaxies. Inspecting values of the pixels residing inside the mask would characterize the distance between the object and the edges. When an object is identified as being too close to the edges, it will be marked with edge-grazing flag.

The software proceeds to compute completeness as a function of apparent magnitude and half-light radius. Completeness is defined as the ratio of the number of detected artificial galaxies to the number of inserted galaxies not marked with edge-grazing flag. Completeness is estimated as a function of artificial galaxies apparent magnitude and half-light radius. Accordingly, inserted and recovered artificial galaxies are enumerated in bins of apparent magnitude and half-light radius. The plane of apparent magnitude and half-light radius is divided to two dimensional bins. Number of these bins will be determined by user and completeness will be assessed specifically in each bin.

The output of the software is a text file, each line of which provides the result of completeness estimation for each of the two dimensional bins. The first two columns contain two labels which uniquely designate every two dimensional bin. In the third and fourth columns magnitude and half-light radius of the center of two dimensional bin are given respectively. Completeness value for the two dimensional bin is written in the fifth column. Finally, in sixth and seventh column, the number of detected and inserted artificial galaxies for each bin are given.

3 Example

In this section, we intend to demonstrate the usage and efficiency of the software. The inspection is based on Hubble Space Telescopes data acquired during GOODS [4] survey [14].

[4]Great Observatories Origins Deep Survey

The input image given to the software for completeness estimation has been selected from southern GOODS field and covers nearly 25 square arcminutes. We have used images taken in F850LP band which is the band normally utilized for detection [8]. We based our study on version v2.0 of HST/ACS data [13].

The number of iterations was set to 165 and in each iteration 1500 artificial galaxies generated. In total, 247500 artificial galaxies were used in the procedure. Artificial galaxies uniformly populate the apparent magnitude range $20 \leq m \leq 30$ (AB magnitude system measured in F850LP band) and half-light radius range $0.01 \leq r_{50} \leq 1.5$ arcseconds. The F850LP-band magnitude zero point was set to 24.862 which is obtained from this URL [6] [30]. The apparent magnitude range was divided to 100 bins while the half-light radius range was intersected to 50 bins. The average number of inserted galaxies in each two-dimensional bin is 50.

The fraction of early-type galaxies to late-type galaxies was set to one. Also, the ratio between half-flux scale radii of late-type and early-type galaxies at a given magnitude was equal to one. For early-type galaxies the axial ratio (b/a) was randomly selected in the range $0.3 \leq b/a \leq 1.0$. For late-type galaxies, inclinations range uniformly between 0 and 90 degrees. We did not apply internal absorption correction.

As was noted in §2, before being inserted to input image, surface brightness profile of the artificial galaxy is to be convolved with appropriate point spread function. For the present study, point spread function is inferred from detailed examination of surface brightness profiles of spectroscopically confirmed stars. Using the updated version (v2) of the GOODS-MUSIC catalogue [15, 28], we selected 138 objects with spectroscopic redshift quality flag < 2 and zspec $= 0$ as stars (cf. [5]). Moreover, we included 63 stars in GOODS-South field identified by [23] based on low resolution spectra acquired in PEARS survey [24]. Of 172 unique stars thus spotted throughout the southern GOODS field, 45 stars reside within the region covered in our input image. Surface brightness profile of 42 stars of the selected sample were used to construct point spread function. For construction of point spread function, we utilized `IRAF DAOPHOT` package.

When convolved with point spread function, artificial galaxies inserted to the input image without additional Poisson noise. As a result, for bright objects, the noise is slightly underestimated while for faint objects this shortcut does not affect the results as the background completely dominates (cf. [14]). We used the `SExtractor` configuration files which were optimized for detection based on v2.0 of HST/ACS images of southern GOODS field in F850LP band and are publicly available through this URL [7]

The crossmatch radius used to isolate the recovered artificial galaxies was 0.15 arcsec. Recalling the value of 0.03 arcsec/pix for pixel scale, 0.15 arcsec is equivalent to 5 pixels in the input image. The crossmatch radius was made conservatively small to ensure that the chance of erroneous matches to existing objects is negligible (cf. [4]). The width and length of the rectangular mask defined to identify edge-grazed galaxies were equally set to 3 pixels.

The resulting distribution of completeness in the plane of apparent magnitude and half-light radius is shown in Fig. 3. Contours of constant completeness are illustrated. It is seen that an increase in apparent magnitude in constant half light radius is associated with a decrease in completeness. The same behavior is seen when half-light radius is increased in fixed apparent magnitude. Such a trend introduces surface brightness as a key factor in detectability of galaxies.

Moreover, it should be noted that constant completeness contours tend to fainter apparent magnitudes as half-light radius becomes smaller. For instance, at $r_{50} = 1.5$ arcsec,

[6] http://archive.stsci.edu/pub/hlsp/goods/v2/h_goods_v2.0_rdm.html
[7] http://archive.stsci.edu/pub/hlsp/goods/catlog_r2/h_r2.0z_readme.html

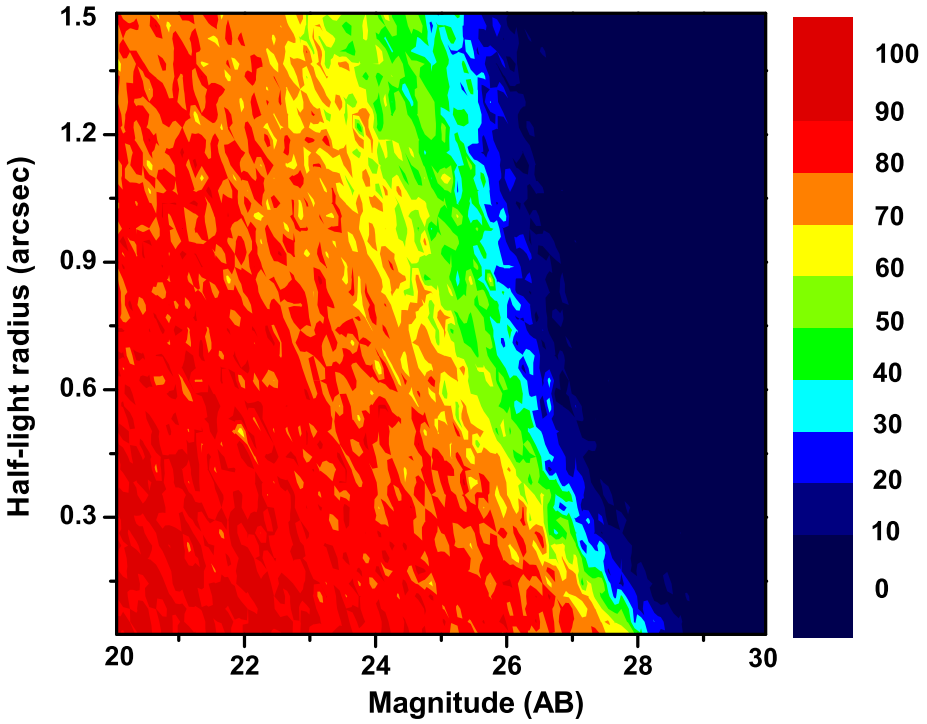

Figure 3: Contour plot representing completeness values in a plane of F850LP magnitude and half-light radius (in units of arcsec.) is shown.

the 70% completeness contour is located at $m \sim 23$ while at $r_{50} = 0.15$ arcsec the same contour is seen at $m \sim 27$. This fact also testifies to the crucial role of surface brightness in detectability of galaxies. It is also seen that the space between the adjacent contours are not uniform. In high surface brightness areas, the contours are more apart compared to low surface brightness regions. This fact reflects that, in spite of its importance, surface brightness is not the only factor that influences the detectability of galaxies.

In a similar study which dates back to 2004 [14], Giavalisco et al. assessed completeness limits based on version v0.5 of HST/ACS images acquired in southern GOODS field in F850LP band. They adopted an analogous method for estimation of completeness as a function of apparent magnitude and half-light radius (see Fig. 4 in [14]). In their study, `IRAF artdata` package was utilized for generating artificial galaxies and `SExtractor` was used as source finder module. Their artificial galaxies uniformly populated the magnitude range $20m28$ (AB magnitude system measured in F850LP band) and the range of galaxy half-light radius was $0.01 \leq r_{50} \leq 1.5$ arcseconds. Morphologically, half of their generated galaxies were of early-type morphology and the remaining half were of late-type morphology. Early-type galaxies had a uniform axial ratio distribution in the range $0.3 \leq b/a \leq 0.9$. Internal absorption was ignored and no additional Poisson noise was at work.

The methodological homology noticed between the two studies enables the comparison of

results and interpretation of the differences in terms of differences in the inputs. Comparison between the two completeness distributions reveals the shifting of completeness contours toward fainter apparent magnitudes in our distribution. Hence, our study implies a higher completeness at a given apparent magnitude in constant half-light radius.

Such a difference can be attributed to the difference in depth of the input images used for the two studies. Our study was based on version v2.0 [13], a significant improvement upon the previous v1.0 release, which is itself an improved version of v0.5 release of GOODS reduced HST/ACS images. Version v1.0 data release provided data acquired as part of the original GOODS HST/ACS program [14]. Version 2.0 augments this with additional data acquired on the two GOODS fields during the search for high redshift Type Ia supernovae carried out during Cycles 12 and 13 (Program ID 9727, P.I. Saul Perlmutter, and 9728, 10339,10340, P.I. Adam Riess [27, 26, 25]. As a result of the additional data, the v2.0 mosaics offer roughly twice the exposure time in the F850LP band compared to version v1.0 images.

4 Summary

Within the next few years, imaging surveys with unprecedented depth and area will revolutionize our vision of the extragalactic sky. Nevertheless, any imaging survey is restricted and biased in its sampling of the galaxy population. Completeness parameter, which quantifies the probability of detection, has proved to be a useful and conventional parameter in assessing the bias in sampling of galaxies. Given the prospect of forthcoming imaging surveys, automated and efficient modules to evaluate their completeness are demanded.

Throughout this paper, we described a software package, named `DASTWAR`, which was improvised to estimate completeness of galaxy detection as a function of apparent magnitude and half-light radius parameters. The software generates artificial galaxies and iteratively inserts them into the input image and then utilizes source finder module to detect them. Comparing the extracted catalog with the catalog of artificial galaxies inserted to input image, yields completeness in the magnitude-size plane (see section 2).

In order to demonstrate the efficiency of the software, we utilized it for completeness estimation on the basis of version v2.0 HST/ACS data in southern GOODS field. In total, 247500 artificial galaxies were generated and used in the procedure. Distribution of completeness values in the magnitude-size plane shows that an increase in apparent magnitude in constant half-light radius is associated with a decrease in completeness and the same trend is noticed when half-light radius is increased in fixed apparent magnitude. We interpreted the mentioned trend as an evidence of pivotal role of surface brightness in determining detectability of galaxies.

We also compared the resulted completeness distribution with the corresponding distribution given by [14]. Comparison between the two completeness distributions revealed the shifting of completeness contours toward fainter apparent magnitudes in our distribution. Such a difference was expected, given the substantially higher depth of v2.0 compared to v0.5 HST/ACS data in southern GOODS field. We envisage that the improvised software would be effective in estimating completeness and helpful in quantifying the biases in sampling of the galaxy population.

Acknowledgment

The cornerstone of the software was laid down when A. K. had been collaborating with School of Astronomy of Institute for Studies in Basic Sciences (IPM), Tehran, Iran. He would like to express his gratitude to Reza Mansouri, Bahram Mobasher, Habib Khosroshahi, Saeed Tavasoli and administrators of the school for their financial and scientific support.

References

[1] Beckwith, S. V. W., Stiavelli, M., Koekemoer, A. M., et al. 2006, AJ, 132, 1729

[2] Bouwens, R. J., Illingworth, G. D., Blakeslee, J. P., Broadhurst, T. J., & Franx, M. 2004, ApJL, 611, L1

[3] Bertin, E., & Arnouts, S. 1996, A&AS, 117, 393

[4] Cameron, E., & Driver, S. P. 2007, MNRAS, 377, 523

[5] Cameron, E., Carollo, C. M., Oesch, P. A., et al. 2011, ApJ, 743, 146

[6] Chiu, I., Desai, S., & Liu, J. 2016, Astronomy and Computing, 16, 79

[7] Chiu, I., Dietrich, J. P., Mohr, J., et al. 2016, MNRAS, 457, 3050

[8] Dahlen, T., Mobasher, B., Dickinson, M., et al. 2010, ApJ, 724, 425

[9] de Vaucouleurs, G. 1948, Annales d'Astrophysique, 11, 247

[10] Disney, M. J. 1976, Nature, 263, 573

[11] Disney, M.; Phillipps, S., 1983, MNRAS, 205, 1253

[12] Freeman, K. C. 1970, ApJ, 160, 811

[13] Giavalisco, M., and the GOODS Team, 2008, in preparation

[14] Giavalisco, M., Ferguson, H. C., Koekemoer, A. M., et al. 2004, ApJL, 600, L93

[15] Grazian, A., Fontana, A., de Santis, C., et al. 2006, A&A, 449, 951

[16] Grogin, N. A., Kocevski, D. D., Faber, S. M., et al. 2011, ApJS, 197, 35

[17] Impey, C., & Bothun, G. 1997, ARA&A, 35, 267

[18] Ivezic, Z. et al., 2008, arXiv:0805.2366

[19] Koekemoer, A. M., Aussel, H., Calzetti, D., et al. 2007, ApJS, 172, 196

[20] La Barbera, F., de Carvalho, R. R., Kohl-Moreira, J. L., et al. 2008, PASP, 120, 681

[21] Laureijs, R., Amiaux, J., Arduini, S., et al. 2011, arXiv:1110.3193

[22] Mutchler, M., Published online at http://www.stsci.edu/institute/conference/cal10/proceedings, p.69

[23] Pirzkal, N., Burgasser, A. J., Malhotra, S., et al. 2009, ApJ, 695, 1591

[24] Pirzkal, N., Xu, C., Malhotra, S., et al. 2004, ApJS, 154, 501

[25] Riess, A. G., Strolger, L.-G., Casertano, S., et al. 2007, ApJ, 659, 98

[26] Riess, A. G., Li, W., Stetson, P. B., et al. 2005, ApJ, 627, 579

[27] Riess, A. G., Strolger, L.-G., Tonry, J., et al. 2004, ApJ, 607, 665

[28] Santini, P., Fontana, A., Grazian, A., et al. 2009, A&A, 504, 751

[29] Stetson, P. B. 1987, PASP, 99, 191

[30] Windhorst, R. A., Cohen, S. H., Hathi, N. P., et al. 2011, ApJS, 193, 27

[31] Zenteno, A., Song, J., Desai, S., et al. 2011, ApJ, 734, 3

Iranian Journal of Astronomy and Astrophysics
Vol. 3, No. 2, Autumn 2016

Iranian Journal of Astronomy and Astrophysics

Spherically Symmetric Solutions in a New Braneworld Massive Gravity Theory

Amir Asaiyan[1] · Kourosh Nozari[2]

[1] Department of Physics, Faculty of Basic Sciences, University of Mazandaran, P.O.Box 47416-95447, Babolsar, Iran ;
email: a.asaiyan@umz.ac.ir (Corresponding Author)

[2] email: knozari@umz.ac.ir

Abstract. In this paper, a combination of the braneworld scenario and covariant de Rham-Gabadadze-Tolley (dRGT) massive Gravity theory is proposed. In this setup, the five-dimensional bulk graviton is considered to be massive. The five dimensional nonlinear ghost-free massive gravity theory affects the 3-brane dynamics and the gravitational potential on the brane. Following the solutions with spherical symmetry on the brane, the full field equations together with the generalized Israel-Darmois junction conditions on the brane and their weak field limits are presented in details. Generally, the theory has four Stückelberg fields along with the components of physical metric. Although analytical solutions of these equations are impossible in general, by considering some simplifying assumptions, two classes of four-dimensional spherically symmetric solutions on the brane with different background Stückelberg fields are obtained.

Keywords: Braneworld Gravity, Massive Gravity, Black Holes

1 Introduction

The accelerating expansion of the Universe has forced us to challenge with our understanding of the fundamental physics [1, 2, 3]. In the last two decades, there has been considerable interest in theories of gravitation that modify the Einstein's gravity at very large distance scales. These theories could explain the present day acceleration, without including a cosmological constant or an exotic matter content. Adding one or even many extra spatial dimensions to the 4D Einstein's theory of gravity may lead to the interesting phenomenological results. The Braneworld model is an extra dimensional theory, in which our universe is a 3-brane embedded in a five-dimensional spacetime called the bulk [4, 5]. All matter fields reside on the brane, but gravitons can travel into the extra dimension. The Dvali-Gabadadze-Porrati (DGP) model [6] is an interesting braneworld model in which the bulk is empty, the extra dimension is infinitely large. Also a 4D Einstein-Hilbert term in the braneworld action exists. The model has attractive results from cosmological viewpoint because gravity on the brane is weakened and becomes five-dimensional at large scales, $r \gg r_c$ (where r_c is the DGP crossover distance), while on small scales, gravity is effectively bounded to the brane and 4D dynamics is regained. It contains a self-accelerating branch of the solutions which can explain late time cosmic speed up [7, 8, 9]. From the 4D perspective, gravity on the brane is mediated by an infinite number of Kaluza-Klein (KK) modes that have not discontinuities. The 4D Einstein-Hilbert term on the brane will suppress the wave functions of heavier KK modes, so that they do not participate in the gravitational interactions on the brane at observable distances [10]. The 4D gravity on the brane is mediated by a massless zero mode, whereas the couplings of the heavy KK modes to ordinary matter

are suppressed.
Due to the cosmological constant problem, we should look for a technically natural way of describing cosmic acceleration. The massive gravity theories are other kinds of modified gravity theories, in which a small graviton mass may lead to an IR modification of gravity with an accelerated expansion without a small cosmological constant. The recent experiments GW150914 and GW151226 [11, 12] by LIGO, were able to detect the gravitational waves and put an upper limit on the graviton mass, i.e. $m < 1.2 \times 10^{-22}$ eV [13]. At the linearized level, the Fierz-Pauli (FP) graviton mass term is the only Lorentz-invariant mass term which after quantization does not generate ghosts in flat space [14]. However, choosing a Fierz-Pauli mass term for the graviton will lead to the well known vDVZ discontinuity [15, 16]. The coupling of the longitudinal polarization of the massive graviton to trace of the energy-momentum tensor in the limit of zero graviton mass is responsible for this discontinuity, such that the tensor structure of the gravitational interaction deviates from that of Einstein gravity. To restore the continuity of Fierz-Pauli massive gravity theory at graviton mass $m = 0$, two different approaches have been proposed. The first one, which was first pointed out by Vainshtein [17, 18], is to consider nonlinear effects. The other way is to consider a curved maximally symmetric spacetime (dS or AdS) with $\frac{m}{H} \to 0$ [19, 20]. In 1972, Vainshtein noted that there is a radius r_V, known as Vainshtein radius, around a massive source, inside of it the linear approximation breaks down and at massless limit r_V goes to infinity [17]. Therefore, the nonlinear terms are important in the limit $m \to 0$. However, Boulware and Deser argued that the non-linear terms cause a scalar field with wrong sign kinetic term, known as Boulware-Deser (BD) ghost [21]. At the classical level, this scalar may not be a problem due to non-linear effects [17, 18], but at the quantum level the theory becomes strongly coupled [22] at energy scale $\Lambda_5 \equiv (m^4 M_P)^{1/5}$. By adding higher order operators, this scale can be raised to order $\Lambda_3 \equiv (m^2 M_P)^{1/3}$.

In 2010, de Rham and Gabadadze studied generic extensions of the Fierz-Pauli Lagrangian by higher-order interactions of the massive spin-2 fluctuation $h_{\mu\nu}$ [23]. Their analysis went to quintic order in the longitudinal component of $h_{\mu\nu}$ and demonstrated that its interactions could in fact be made ghost-free in a decoupling limit. The decoupling limit analysis relies heavily on the aforementioned Goldstone boson analogously suggested by Arkani-Hamed, Georgi and Schwartz [22]. de Rham, Gabadadze and Tolley (dRGT) [24] completed their investigations by presenting a nonlinear theory of massive gravity whose decoupling limit is ghost-free for all nonlinear self-interactions of the longitudinal component [24, 25, 26, 27]. The dRGT theory is the unique ghost-free theory for massive graviton and new kinetic interactions are not consistent [28, 29]. See [30, 31, 32] for recent reviews on all aspects of massive gravity and bimetric theories. In the context of the dRGT nonlinear covariant massive gravity model [23, 24], some self-accelerating solutions have been discovered [33, 34, 35, 36, 37, 38]. Dynamics of the scalar mode of a massive graviton in four-dimensions has been studied in detail in [36], showing that a non-trivial configuration for this field leads to self-acceleration. Scalar fluctuations around these self-accelerating configurations are proved to be free of ghosts.

It is worthwhile to note that one way in which a massive graviton naturally arises is higher dimensional scenarios. A theory of gravity with compactified extra dimensions can be viewed as a four dimensional theory of multiple gravitons, i.e. KK modes. An alternative to the KK paradigm was the ADD model [39, 40] in which one (or more) extra dimension could emerge from a theory of a finite number of massive gauge fields or gravitons living in four dimensions. Their idea, named "Dimensional Deconstruction", can be viewed as taking a five dimensional gauge or gravity theory and discretizing the extra dimension(s).

It has been shown that Dimensional Deconstruction is equivalent to a truncation of the KK tower at the nonlinear level [28]. It has been shown that the DGP model is closely related to massive gravity. In this model, the 4D graviton propagator on the brane in the Gaussian normal coordinates is similar to the propagator for 4D massive gravity with graviton mass $m^2 = (\frac{1}{r_c})\sqrt{-\Box}$, where $r_c \equiv (M_p^2/2M_5^3)$ is the DGP crossover length scale and $\Box$ is the four-dimensional d'Alembertian. In other words, the graviton acquires a soft mass, or resonance effectively, in the DGP model. The induced gravity term in the brane action acts as a kinetic term for a 4D graviton while the bulk Einstein-Hilbert term acts as a gauge invariant mass term. Therefore, the vDVZ discontinuity problem is also present in the DGP model. Here, the massless limit converts to the limit $r_c \to \infty$. As argued by Vainshtein, at distances smaller than the radius r_V, the linearization breaks down and by considering nonlinear effects, we can restore the predictions of GR on the brane [17, 18, 41, 42]. However, the DGP model has some consistency problems. The normal branch of the DGP theory is free of ghosts and instabilities, but the self-accelerating branch is completely unstable [43, 44, 45]. The DGP model has strong interactions at energy scale $\Lambda \sim (M_p/r_c^2)^{1/3}$. From the 4D point of view, there is an extra scalar degree of freedom π that contributes to the extrinsic curvature of the brane as $K_{\mu\nu} \propto \partial_\mu \partial_\nu \pi$ [43, 44]. Indeed, this scalar is a brane bending mode that interacts strongly at momenta of order Λ. In the decoupling limit of the DGP model, in which Λ is kept fixed, only the π sector exists and all other degrees of freedom decouple. This limit reduces to the cubic Galileon for the helicity-0 mode π [46].

The works done by Gabadadze and de Rham before proposing the interesting dRGT theory have shown that the introduction of the spurious extra dimension provides a geometrical interpretation of massive gravity, for which non-linearities can be tracked down explicitly [47, 48]. By studying massive gravity from extra dimensional point of view, we can better understand certain aspects of the dRGT theory [23, 24] and its bigravity [49] and multigravity [50] extensions. In 2009, Gabadadze considered an extension of GR by an auxiliary non-dynamical extra dimension and showed that the obtained gravitational equations could have a self-accelerated solution, which is due to a new mass parameter m. The auxiliary dimension gives an extrinsic curvature to the 4D space-time and the extrinsic curvature is responsible for creating the mass term. The special structure $[K]^2 - [K^2]$ arose from the Gauss equation for the bulk Ricci scalar ensures the Fierz-Pauli structure which is ghost-free at the linearized level [47]. de Rham and Gabadadze [48, 51] verified that the theory in the decoupling limit is free of the Boulware-Deser ghost to cubic order. In ref [28], it was shown that the ghost-free models of massive gravity and their multi-graviton extensions can follow from considering higher dimensional extension of GR in the Einstein-Cartan form on a discrete extra dimension. Indeed, discretizing the extra dimension in the vielbein language can automatically generate the square root structure characteristic of the dRGT model, i.e. $\mathcal{K}_\mu^\nu$, [28]. Indeed, the expression for the discretized extrinsic curvature coincides with $\mathcal{K}_\mu^\nu$.

By considering the above arguments, now giving a mass to the graviton in Higher-dimensional theories and exploring the overall effects of massive gravity and extra dimension could be interesting from theoretical and phenomenological viewpoints. The final results may have some relations with the multi-metric theories and then lead to physically interesting predictions. In 2004, Chacko et al., considered a braneworld setup in warped anti-de Sitter spacetime (Randall-Sundrum (RS) two-brane model [52]) with a mass term for the graviton on the infrared brane [53]. The predictions of this theory coincide with the results of GR at distances smaller than the infrared scale but at longer distances a theory of massive gravity exists. However, in the low energy limit of the theory, there is a ghost, which corresponds to the radion field. In Ref. [54], both of the bulk and the brane mass terms were introduced

in the action of the RS two-brane model to quadratic order to modify the profile of the graviton zero-mode in the extra dimensions. It was found that for a particular choice of parameters, there is an IR-peaked zero-mode, i.e. the graviton can be localized on the IR brane. In 2014, a braneworld scenario has been investigated in which the infinite-volume bulk graviton was massive [55]. The bulk graviton can be as heavy as the bulk Planck scale which is much larger than the inverse Hubble size. The 4D induced gravity term on the brane shields the brane matter from both strong bulk gravity and large bulk graviton mass. Higher-dimensional gravity at large distances are not obtained on the brane in this setup and at distances above the bulk Planck length scale, the 4D graviton on the brane acquires a small mass. The author of [55] considered a mass potential that arose via the gravitational Higgs mechanism, such that a general quadratic potential in terms of perturbation tensor h_{AB} was introduced in the bulk action. In this extension of the DGP model, even for the case of ghost-free Fierz-Pauli bulk mass term, the 4D tensor structure on a 3-brane could be obtained [55]. Here, the key point is that the trace $h \equiv \eta^{AB} h_{AB}$ is perturbatively a ghost. However, it was shown that the non-perturbative Hamiltonian is bounded from below and there is no ghost in full nonlinear theory [56, 57, 58].

With these detailed preliminaries which are necessary for a reader to understand forthcoming arguments in this paper, we consider a combination of the DGP braneworld and dRGT massive gravity models, by introducing a five dimensional nonlinear ghost-free potential in the bulk action. In this setup, our universe is a 3-brane embedded in a 5D bulk where the extra spatial dimension is large. A 5D ghost-free massive gravity theory propagates nine degrees of freedom (DOF) and the extra four DOFs added to the five DOFs of 5D massless graviton, which is effectively equivalent to a 4D softly massive graviton, are the extra polarizations of the 5D massive graviton. We considered the induced gravity term on the brane action, because this term in the DGP setup acts as a kinetic term for the 4D graviton. The 5D extension of dRGT theory is free of ghosts and we want to explore the effects of this nonlinear theory on the brane dynamics and the effective 4D gravitational interactions on the brane. For this purpose, the full 5D field equations and their weak field limits have been studied. Our focus is on the solutions with spherical symmetry on the brane. The full nonlinear equations of motion in the presence of the unknown stückelberg fields are generally very complicated to solve for analytical solutions, unless we consider some simplifying assumptions. So, to have some intuition and to be more clarified, we have adopted step by step some reasonable and simplifying assumptions to find a class of four-dimensional spherically symmetric solutions on the brane. We considered two simplified linear theories in both unitary and non-unitary gauges and found in both cases a flat solution on the brane with different background Stückelberg fields. In non-unitary gauge we restricted ourself to special choices of the free parameters of the theory. We note that general massive braneworld solutions, resulting from the full nonlinear theory, should reduce to the massless braneworld solution in the limit of zero bulk graviton mass as has been studied in [59]. We are attempting to follow new approaches, such as solving the nonlinear field equations numerically or finding the effective 4D field equations on the brane [60, 61], to examine the Vainshtein mechanism in our model.

2 Braneworld Massive Gravity

In braneworld scenarios, we assume that our (1+3)-dimensional spacetime is a domain wall embedded in a five-dimensional spacetime called the bulk [4, 5]. All matter fields live on the

brane but only gravitons can travel into the bulk. In the DGP braneworld model, the bulk is empty, the extra dimension is infinitely large and a 4D Einstein-Hilbert term exists on the brane action [6]. In our braneworld massive gravity model, we introduce a mass potential to the bulk action, which is a 5D extension of the dRGT's 4D nonlinear ghost-free massive gravity theory [23, 24]. We consider a 3-brane Σ embedded in the five-dimensional massive bulk $\mathcal{M}$. The total action is

$$S = \frac{M_5^3}{2}\int_{\mathcal{M}} d^5X\sqrt{-g}\left({}^{(5)}R + m_g^2\,\mathcal{U}(g,\mathcal{K})\right) + S_{brane}, \tag{1}$$

where S_{brane} is the 3-brane action defined as

$$S_{brane} = \frac{M_p^2}{2}\int_{\Sigma} d^4x\sqrt{-q}\;{}^{(4)}R + \int_{\Sigma} d^4x\sqrt{-q}\,\mathcal{L}_4^{matt} + \int_{\Sigma} d^4x\sqrt{-q}\,\frac{K}{\kappa_5^2}\,. \tag{2}$$

g_{AB} is the 5D bulk metric with corresponding Ricci tensor given by ${}^{(5)}R_{AB}$. X^A, $A = 0,1,2,3,5$ are the coordinates in the bulk. The brane has induced metric $q_{\mu\nu}$ with corresponding Ricci tensor ${}^{(4)}R_{\mu\nu}$. $\mathcal{L}_4^{matt}$ is the matter Lagrangian localized on the brane. We note also that the bulk Planck mass M_5 and the 4-dimensional Planck scale M_p are defined as $\kappa_5^2 = 8\pi G_{(5)} = M_5^{-3}$ and $\kappa_4^2 = 8\pi G_{(4)} = M_p^{-2}$. $\mathcal{U}$ is a dimensionless "potential" for the metric g_{AB} that makes bulk graviton massive, where the dimension-full parameter m_g sets the graviton mass scale. This potential depends on three dimensionless arbitrary parameters α_3, α_4 and α_5 and is composed of four parts,

$$\mathcal{U}(g,\mathcal{K}) = \sum_{n=2}^{5}\alpha_n\mathcal{U}_n(\mathcal{K}) = \mathcal{U}_2 + \alpha_3\,\mathcal{U}_3 + \alpha_4\,\mathcal{U}_4 + \alpha_5\,\mathcal{U}_5, \tag{3}$$

where $\alpha_2 = 1$. The tensor $\mathcal{K}_A^B$ is

$$\mathcal{K}_A^B = \delta_A^B - \sqrt{g^{BC}(g_{CA} - H_{CA})} = \delta_A^B - \sqrt{g^{BC}f_{ab}\partial_C\phi^a\partial_A\phi^b}. \tag{4}$$

The potential (3) is unique and no further polynomial terms can be added to the action without introducing the BD ghost [23, 24, 25, 26, 27]. The sum is finite and stops at $n = 5$, since the total derivative combinations vanish for $n > D = 5$ [24, 31]. It was shown that this is the most general potential for a ghost-free theory of massive gravity [62]. f_{ab} is the fiducial (or reference) metric, which we assume to be the Minkowski metric, $\eta_{\mu\nu}$, and ϕ^a are the Stückelberg scalar fields introduced to give a manifestly diffeomorphism invariant description [22]. Under a diffeomorphism $\delta X^A = \xi^A(X)$, the Stückelberg fields ϕ^0, ϕ^i $(i = 1,2,3,5)$ transform as simple scalars. The tensor h_{AB} represents the fluctuations of bulk metric about Minkowski reference metric, $h_{AB} = g_{AB} - \eta_{AB}$, and H_{AB} corresponds to the covariantization of metric perturbations, defined as $H_{AB} = g_{AB} - \partial_A\phi^a\partial_B\phi^b\eta_{ab}$. The square root is formally understood as $\sqrt{W}_C^A\sqrt{W}_B^C = W_B^A$. The four polynomial terms $\mathcal{U}_2$, $\mathcal{U}_3$, $\mathcal{U}_4$, and $\mathcal{U}_5$ depend on the metric g and Stückelberg fields ϕ^a as

$$\mathcal{U}_2 = [\mathcal{K}]^2 - [\mathcal{K}^2], \tag{5}$$

$$\mathcal{U}_3 = \frac{1}{3}[\mathcal{K}]^3 - [\mathcal{K}^2][\mathcal{K}] + \frac{2}{3}[\mathcal{K}^3], \tag{6}$$

$$\mathcal{U}_4 = \frac{1}{12}[\mathcal{K}]^4 - \frac{1}{2}[\mathcal{K}^2][\mathcal{K}]^2 + \frac{2}{3}[\mathcal{K}^3][\mathcal{K}] + \frac{1}{4}[\mathcal{K}^2]^2 - \frac{1}{2}[\mathcal{K}^4], \tag{7}$$

$$\mathcal{U}_5 = \frac{1}{60}[\mathcal{K}]^5 - \frac{1}{3}[\mathcal{K}^3][\mathcal{K}^2] + \frac{1}{3}[\mathcal{K}^3][\mathcal{K}]^2 - \frac{1}{6}[\mathcal{K}^2][\mathcal{K}]^3 - \frac{1}{2}[\mathcal{K}][\mathcal{K}^4] + \frac{1}{4}[\mathcal{K}][\mathcal{K}^2]^2 + \frac{2}{5}[\mathcal{K}^5], \quad (8)$$

where the square brackets are defined as

$$[\mathcal{K}] \equiv \mathrm{tr}\mathcal{K}^B_A\,, \quad [\mathcal{K}]^2 \equiv \left(\mathrm{tr}\mathcal{K}^B_A\right)^2, \quad [\mathcal{K}^2] \equiv \mathrm{tr}\mathcal{K}^B_C\mathcal{K}^C_A. \quad (9)$$

We chose a coordinate y for the extra dimension so that our 3-brane is localized at $y = 0$. Variation of the action (1) with respect to the bulk metric leads to the modified 5D field equations in the bulk as [56, 57, 58]

$${}^{(5)}G_{AB} + m_g^2\,\overline{X}_{AB} = \kappa_5^2\ {}^{(loc)}T_{AB}\delta(y), \quad (10)$$

where $\overline{X}_{AB}$ is the effective energy-momentum tensor due to the graviton mass and expressed as

$$\overline{X}_{AB} = X_{AB} + \sigma Y_{AB}, \quad (11)$$

with

$$X_{AB} = -\frac{1}{2}(\alpha\,\mathcal{U}_2 + \beta\,\mathcal{U}_3)g_{AB} + \tilde{X}_{AB}, \quad (12)$$

$$\tilde{X}_{AB} = \mathcal{K}_{AB} - [\mathcal{K}]g_{AB} - \alpha\Big\{\mathcal{K}^2_{AB} - [\mathcal{K}]\mathcal{K}_{AB}\Big\} + \beta\Big\{\mathcal{K}^3_{AB} - [\mathcal{K}]\mathcal{K}^2_{AB} + \frac{\mathcal{U}_2}{2}\mathcal{K}_{AB}\Big\}, \quad (13)$$

$$Y_{AB} = -\frac{\mathcal{U}_4}{2}\,g_{AB} + \tilde{Y}_{AB}, \quad (14)$$

$$\tilde{Y}_{AB} = \frac{\mathcal{U}_3}{2}\mathcal{K}_{AB} - \frac{\mathcal{U}_2}{2}\mathcal{K}^2_{AB} + [\mathcal{K}]\mathcal{K}^3_{AB} - \mathcal{K}^4_{AB}. \quad (15)$$

The new parameters α, β, and σ are defined as $\alpha = 1 + \alpha_3$, $\beta = \alpha_3 + \alpha_4$, $\sigma = \alpha_4 + \alpha_5$, and the indices are raised and lowered by the "physical" metric g_{AB}, so that $\mathcal{K}_{AB} = g_{AC}\mathcal{K}^C_B$, $\mathcal{K}^2_{AB} = g_{AD}\mathcal{K}^D_C\mathcal{K}^C_B$, etc.

The effective localized energy-momentum tensor on the brane including the contribution from the induced 4D Einstein-Hilbert term on the brane is

$${}^{(loc)}T_{AB} = g^\mu_A g^\nu_B(-\frac{1}{\kappa_4^2})\sqrt{\frac{-q}{-g}}\Big({}^{(4)}G_{\mu\nu} - \kappa_4^2\ {}^{(4)}T_{\mu\nu}\Big). \quad (16)$$

where ${}^{(5)}G_{AB}$ and ${}^{(4)}G_{AB}$ denote the Einstein tensors constructed from the bulk and the brane metrics respectively. The tensor $q_{AB} = g_{AB} - n_A n_B$ is the induced metric on the brane Σ with n_A the normal vector on this hypersurface. The field equations in the bulk ($y \neq 0$) take the following form

$${}^{(5)}G_{AB} = {}^{(5)}R_{AB} - \frac{1}{2}\,{}^{(5)}R\,g_{AB} = -m_g^2\,\tilde{X}_{AB}. \quad (17)$$

Moreover, if the components of $\tilde{X}_{AB}$ be continuous across $y = 0$, the following modified (due to the presence of induced gravity on the brane) Israel-Darmois junction conditions, as a boundary condition for the field equations in the bulk, would be obtained

$$[K^\nu_\mu] - \delta^\nu_\mu[K] = -\kappa_5^2\ {}^{(loc)}T^\nu_\mu = \Big(\frac{\kappa_5^2}{\kappa_4^2}\Big){}^{(4)}G^\nu_\mu - \kappa_5^2\ {}^{(4)}T^\nu_\mu, \quad (18)$$

where $K_{\mu\nu} = \frac{1}{2}\partial_y(g_{\mu\nu})$ is the extrinsic curvature of the brane and brackets denote jump across the brane ($y = 0$). We assume a $\mathbf{Z}_2$-symmetry on reflection around the brane, thus the Israel-Darmois junction conditions become

$$\overline{K}_{\mu}^{\ \nu} - \overline{K}\delta_{\mu}^{\ \nu} = r_c\, {}^{(4)}G_{\mu}^{\nu} - \frac{\kappa_5^2}{2}\, {}^{(4)}T_{\mu}^{\nu}, \tag{19}$$

where $r_c = \frac{\kappa_5^2}{2\kappa_4^2} = \frac{M_p^2}{2M_5^3}$ is the well-known DGP crossover distance, and by definition $\overline{K}_{\mu}^{\ \nu} = K_{\mu}^{\nu}(y = 0^+) = -K_{\mu}^{\nu}(y = 0^-)$.

After presentation of general field equations in the proposed setup, now we seek for some spherically symmetric solutions on the brane.

3 Spherically Symmetric Solutions

Here, we consider the static spherically symmetric configurations on the brane and our concentration is on the issue of braneworld black holes, i.e. finding the bulk and the brane metric when a spherically symmetric energy-momentum distribution is localized on the brane. In our previous work [59], black hole solutions in warped DGP braneworld model with a cosmological constant term in the bulk were obtained (see [63, 64, 65, 66] for further black hole solutions in braneworld scenarios). We found a 5D black string solution for the bulk metric, which reduces to 4D Schwarzschild-AdS solution on the brane. The 4D AdS curvature radius is proportional to r_c, therefore the Schwarzschild solution is recovered on the brane in the limit $r_c \to \infty$ [59]. As we already noted, the DGP model is closely related to massive gravity and the 4D graviton propagator on the brane is similar to the propagator for 4D massive graviton. In the dRGT theory with a Minkowski reference metric, a class of non-bidiagonal Schwarzschild-dS solutions was found in [33, 34]. In this theory, for a special choice of free parameters of the action, the Schwarzschild-dS type of black hole solutions was obtained in ref [67, 35], where the mass term behaves similar to the cosmological constant term in GR. For this choice of parameters, the Bianchi identity is automatically satisfied for a certain diagonal and time-independent metrics in spherical polar coordinates, whereas the kinetic terms for both the vector and scalar fluctuations vanish in the decoupling limit. Although it was shown that the linearized solutions of GR can be reproduced below the Vainshtein radius in a certain region of parameter space, the metric here is accompanied by nontrivial backgrounds for the Stückelberg fields. The vector and scalar modes A^μ and π of massive gravitons are the nonunitary parts of the background Stückelberg fields [35], i.e. $x^\mu - \phi^\mu = (m\, A^\mu + \partial^\mu \pi)/\Lambda^3$. For reviewing the black hole solutions in massive gravity see refs. [68, 69, 70, 71].

All of these papers have focused only on the four-dimensional dRGT theory [23, 24], in which only the usual graviton terms, $\mathcal{U}_i$ ($i = 2 - 4$), are considered. For spherically symmetric solutions in extra dimensional setups, some types of black hole solutions for dRGT massive gravity with their thermodynamical properties have been investigated in d-dimensional spacetimes ($d \geq 3$) in refs. [72, 73, 74, 75, 76, 62]. The behavior of massive graviton terms for some cosmological solutions such as the FLRW, Bianchi type I, and also Schwarzschild-Tangherlini-(A)dS metrics in a specific five-dimensional nonlinear massive gravity and bigravity models have been clarified in Refs. [62, 77]. In ref. [78], it was argued that giving a space-dependent mass to the 5D graviton, which depends on the extra-dimensional coordinate, can localize Einstein gravity on a 3-brane embedded in a 5D

Minkowski space. They focused on the quadratic Fierz-Pauli Lagrangian for 5D metric perturbations and explored the linearized equations of motion for 4D scalar, vector and tensor modes. They showed that there is no ghost on the brane and conserved matter on the brane does not couple to the scalar massless mode. The nonlinear extension of the theory has not been studied yet.

We want to find a 4D spherically symmetric solution for our nonlinear massive braneworld setup and separately determine the effects of bulk graviton mass term and also the large extra dimension on the gravitational interactions on the brane. We expect that the predictions of GR and DGP model be reproduced in appropriate limits, i.e. $m \to 0$ limit for recovering the DGP results and $r_c \to \infty$ limit in addition to the previous one for recovering GR on the brane. The issues of the vDVZ discontinuity and the Vainshtein mechanism to resolve it should be carefully studied. The effects of bulk nonlinear terms and the brane bending modes play important roles in these limits. To obtain black hole solutions in a braneworld scenario, generally there are two different approaches. In the first approach, as we explained in last section, dynamics and geometry of the whole bulk spacetime are primarily considered; then the dynamics on the brane is extracted by using the Israel-Darmois matching conditions. The second approach is to obtain the effective four-dimensional field equations on the brane firstly and then try to extend these solutions into the bulk [60, 61]. Here, we will follow the first approach. Therefore, to choose an appropriate 5D line element which is spherically symmetric on the brane, we review the 4D black hole solutions of the original dRGT theory. In this case, the ansatz for the static spherically symmetric solutions is the same as in GR. The only subtlety consists in getting the correct configuration for the four scalar fields. Regarding the vacuum solution of the theory, ($\phi^a = x^\mu\, \delta^a_\mu$ and $g_{\mu\nu} = \eta_{\mu\nu}$), the spherically symmetric line element and the four scalar fields for 4D massive gravity models can be written as follows

$$ds^2 = -\alpha(r)dt^2 + 2\delta(r)dtdr + \beta(r)dr^2 + \chi(r)\Big(d\theta^2 + \sin^2(\theta)d\varphi^2\Big), \tag{20}$$

$$\phi^0 = t + h(r), \quad \phi^i = \phi(r)\frac{x^i}{r}. \tag{21}$$

In the unitary gauge, the scalar fields are $\phi^a = x^a = (t, r\sin\theta\cos\phi, r\sin\theta\sin\phi, r\cos\theta)$. Therefore, in this gauge $h(r) = 0$ and $\phi(r) = r$. The field configuration is invariant under two residual coordinate transformations. The first one is an arbitrary change of the radial coordinate $r \to \widetilde{r} = \widetilde{r}(r)$, which allows to set either $\chi(r) = r^2$ or $\phi(r) = r$. The second one is the redefinition of the time variable $t \to \widetilde{t} = t + \tau(r)$, which allows to cancel either $\delta(r)$ or $h(r)$. In our five dimensional braneworld theory, we can choose a coordinate system in which the brane is located at $y = 0$ and the 5D metric with spherical symmetry on the brane are as follows

$${ds_5}^2 = -e^{\nu(r,y)}dt^2 + e^{\lambda(r,y)}dr^2 + r^2e^{\mu(r,y)}d\Omega^2 + dy^2\,, \tag{22}$$

where the 5D Stückelberg fields are

$$\phi^0 = t,\ \phi^i = \phi(r)\frac{x^i}{r},\ \phi^5 = y. \tag{23}$$

As compared to ordinary Braneworld theories, this configuration contains an additional radial function $\phi(r)$, which should be determined. The matter content of the 3-brane universe is considered to be a localized spherically symmetric untilted perfect fluid (e.g. a star) with

$${}^{(4)}T_{\mu\nu} = (\rho + p)u_\mu u_\nu + pq_{\mu\nu}\,, \tag{24}$$

where u^μ stands for the 4-velocity of the fluid and $\rho = p = 0$ for $r > R$. Nevertheless, since we want to obtain static black hole solutions outside the star (that is, for $r > R$), in these regions the brane is empty. With the ansatz (22) and (23), the components of $\mathcal{K}_A^B$ would take the following form

$$\mathcal{K}_A^B = \mathrm{diag}\left(1-(e^{-\frac{\nu}{2}}), 1-(\phi' e^{-\frac{\lambda}{2}}), 1-(\frac{\phi}{r}e^{-\frac{\lambda}{2}}), 1-(\frac{\phi}{r}e^{-\frac{\lambda}{2}}), 0\right). \tag{25}$$

By using these components, we can obtain the total derivative combinations $\mathcal{U}_2, \mathcal{U}_3, \mathcal{U}_4$ and $\mathcal{U}_5$. We have found that the term $\mathcal{U}_5$ vanishes for this configuration. Consequently, the components of $\overline{X}_{AB}$ can be obtained analytically although their expressions are so lengthy. The Einstein tensor components are nonlinear and second order in terms of ν, λ, μ and their partial derivatives. To find some analytical solutions, firstly we consider the *weak-field regime* (i.e. far enough from the source localized on the brane). In this respect, we will find solutions in the regimes where $|\nu|$, $|\lambda|$ and $|\mu|$ are small quantities compared to unity; that is, $|\nu|, |\lambda|, |\mu| \ll 1$. By adopting this assumption, we linearize our field equations with respect to these functions. Now, by putting the metric (22) into the bulk field equations (17) and keeping only the leading-order terms, we obtain the (tt), (rr), $(\theta\theta)$, (yy), and (ry) components of the bulk field equations respectively as follows:

$$\begin{aligned}
&2(\mu-\lambda)+2r^2\mu_{rr}+6r\mu_r-2r\lambda_r+r^2(\lambda_{yy}+2\mu_{yy})\\
&+2m_g^2r^2\Bigg\{\left[3+3\alpha+\beta-(1+2\alpha+\beta)(\phi'+2\frac{\phi}{r})+(\alpha+\beta)(\frac{\phi^2}{r^2}+2\frac{\phi\phi'}{r})-\beta\frac{\phi'\phi^2}{r^2}\right](1+\nu)\\
&+\left[(1+2\alpha+\beta)\frac{\phi'}{2}-(\alpha+\beta)\frac{\phi\phi'}{r}+\beta\frac{\phi'\phi^2}{2r^2}\right]\lambda+\left[(1+2\alpha+\beta)\frac{\phi}{r}-(\alpha+\beta)(\frac{\phi\phi'}{r}+\frac{\phi^2}{r^2})+\beta\frac{\phi'\phi^2}{r^2}\right]\mu\Bigg\}=0\,,
\end{aligned} \tag{26}$$

$$\begin{aligned}
&2(\lambda-\mu)-2r\mu_r-2r\nu_r-r^2(\nu_{yy}+2\mu_{yy})+2m_g^2r^2\Bigg\{\left[-(\alpha+2)+2(\alpha+1)\frac{\phi}{r}-\alpha\frac{\phi^2}{r^2}\right](1+\lambda)\\
&+\left[-\frac{1}{2}(1+2\alpha+\beta)+(\alpha+\beta)\frac{\phi}{r}-\frac{1}{2}\beta\frac{\phi^2}{r^2}\right]\nu+\left[-(\alpha+1)\frac{\phi}{r}+\alpha\frac{\phi^2}{r^2}\right]\mu\Bigg\}=0\,,
\end{aligned} \tag{27}$$

$$\begin{aligned}
&-r^2(\nu_{rr}+\mu_{rr})-r\nu_r-2r\mu_r+r\lambda_r-r(\nu_{yy}+\lambda_{yy}+\mu_{yy})+2m_g^2r^2\Bigg\{-(\alpha+2)+(\alpha+1)(\frac{\phi}{r}+\phi')-\alpha\frac{\phi\phi'}{r}\\
&+\left[-\frac{1}{2}(1+2\alpha+\beta)+\frac{1}{2}(\alpha+\beta)(\frac{\phi}{r}+\phi')-\frac{1}{2}\beta\frac{\phi\phi'}{r}\right]\nu+\left[-\frac{1}{2}(1+\alpha)\phi'+\frac{1}{2}\alpha\frac{\phi\phi'}{r}\right]\lambda\\
&+\left[-2-\alpha+3\beta-3\sigma+(1+\alpha-5\beta+11\sigma)\frac{\phi}{2r}+(1+\alpha-\beta+\sigma)\phi'+(-\alpha+\beta-3\sigma)\frac{\phi\phi'}{2r}-\frac{5}{2}\sigma\frac{\phi^2}{r^2}+\frac{1}{2}\sigma\frac{\phi'\phi^2}{r^2}\right]\mu\Bigg\}=0\,,
\end{aligned} \tag{28}$$

$$2(\lambda-\mu)-2r^2\mu_{rr}-r^2\nu_{rr}+2r(\lambda_r-3\mu_r-\nu_r)+2m_g^2r^2\Bigg\{-(3+3\alpha+\beta)+(1+2\alpha+\beta)(\phi'+2\frac{\phi}{r})-(\alpha+\beta)(\frac{\phi^2}{r^2}+2\frac{\phi'\phi}{r})$$

$$+\beta\frac{\phi'\phi^2}{r^2}+\left[-\frac{1}{2}(1+3\alpha+3\beta+\sigma)+\frac{1}{2}(\alpha+2\beta+\sigma)(\phi'+2\frac{\phi}{r})-(\sigma+\beta)(\frac{\phi\phi'}{r}+\frac{\phi^2}{2r^2})+\frac{1}{2}\sigma\frac{\phi'\phi^2}{r^2}\right]\nu$$

$$+\left[-\frac{1}{2}(1+2\alpha+\beta)\phi'+(\alpha+\beta)\frac{\phi\phi'}{r}-\frac{1}{2}\beta\frac{\phi'\phi^2}{r^2}\right]\lambda+\left[-(1+2\alpha+\beta)\frac{\phi}{r}+(\alpha+\beta)(\frac{\phi'\phi}{r}+\frac{\phi^2}{r^2})-\beta\frac{\phi'\phi^2}{r^2}\right]\mu\Bigg\}=0\,, \tag{29}$$

$$(\lambda-\mu)=r\mu_r+\frac{1}{2}r\nu_r+f(r)\,, \tag{30}$$

where $f(r)$ is an arbitrary function of r. The subscripts y and r in these relations represent partial differentiation with respect to y and r respectively. Prime in ϕ' denotes derivative with respect to r. In addition to the generalized field equations (17), the Bianchi identities lead to the constraint:

$$m_g^2\quad\nabla^A\overline{X}_{AB}\Big)=0\,, \tag{31}$$

where ∇^A denotes the covariant derivative with respect to physical metric g_{AB}. In the cases $m_g\neq 0$, the linearized form of these constraints for $B=1$ and $B=4$ are respectively as follows

$$2\alpha(\frac{\phi^2}{r^2}-\frac{\phi\phi'}{r})+2(1+\alpha)(\phi'-\frac{\phi}{r})+\left[-\frac{1}{2}(1+2\alpha+\beta)+(\alpha+\beta)\frac{\phi}{r}-\frac{1}{2}\beta\frac{\phi^2}{r^2}\right]r\nu_r+\left[-(\alpha+1)\frac{\phi}{r}+\alpha\frac{\phi^2}{r^2}\right]r\mu_r$$

$$+\left[(\alpha+\beta)(\phi'-\frac{\phi}{r})+\beta(\frac{\phi^2}{r^2}-\frac{\phi\phi'}{r})\right]\nu+\left[(\alpha+1)(\frac{\phi}{r}-\phi')+2\alpha(\frac{\phi\phi'}{r}-\frac{\phi^2}{r^2})\right]\mu=0\,, \tag{32}$$

$$\frac{\partial}{\partial y}(\overline{X}_{44})=\left[-\frac{1}{2}(1+3\alpha+3\beta+\sigma)+\frac{1}{2}(\alpha+2\beta+\sigma)(\phi'+2\frac{\phi}{r})-(\sigma+\beta)(\frac{\phi\phi'}{r}+\frac{\phi^2}{2r^2})+\frac{1}{2}\sigma\frac{\phi'\phi^2}{r^2}\right]\nu_y$$

$$+\left[-\frac{1}{2}(1+2\alpha+\beta)\phi'+(\alpha+\beta)\frac{\phi\phi'}{r}-\frac{1}{2}\beta\frac{\phi'\phi^2}{r^2}\right]\lambda_y+\left[-(1+2\alpha+\beta)\frac{\phi}{r}+(\alpha+\beta)(\frac{\phi'\phi}{r}+\frac{\phi^2}{r^2})-\beta\frac{\phi'\phi^2}{r^2}\right]\mu_y=0\,, \tag{33}$$

where other components of the constraint (31) are satisfied automatically. Contrary to the easy DGP model, which we studied in our previous paper [59], the presence of graviton mass terms in the 5D field equations (26)-(30) makes it more difficult to find an exact solution. The linearised form of the Israel-Darmois matching conditions (19) will lead to the following boundary conditions (on the brane) for the filed equations in the bulk

$$-\frac{1}{2}\Big(2\mu_y+\lambda_y\Big)|_{y=0^+}=r_c\Big[-\frac{1}{r^2}\Big(\mu-\lambda+3r\mu_r+r^2\mu_{rr}-r\lambda_r\Big)\Big]\,, \tag{34}$$

$$-\frac{1}{2}\Big(2\mu_y+\nu_y\Big)|_{y=0^+}=r_c\Big[-\frac{1}{r^2}\Big(\mu-\lambda+r\mu_r+r\nu_r\Big)\Big]\,, \tag{35}$$

$$-\frac{1}{2}\Big(\nu_y+\lambda_y+\mu_y\Big)|_{y=0^+}=r_c\Big[-\frac{1}{2r}\Big(r\nu_{rr}+r\mu_{rr}+2\mu_r+\nu_r-\lambda_r\Big)\Big]\,. \tag{36}$$

Note that these equations are hold on the brane outside our spherical object, where ρ and p are zero. Solving the linearized bulk field equations (26)-(30) with constraints (32) and

(33) (resulting from the Bianchi identities), is a very difficult task in non-unitary gauges. Therefore, here we consider some additional simplifying assumptions for the theory. The first assumption is that we find solutions in the unitary gauge, i.e. $\phi(r) = r$. In this gauge, the linearized form of all the higher order combinations, $\mathcal{U}_2$, $\mathcal{U}_3$ and $\mathcal{U}_4$ vanish such that

$$\overline{X}_{AB} = \mathcal{K}_{AB} - [\mathcal{K}]g_{AB} = \text{diag} \quad (\frac{1}{2}\lambda + \mu), -(\frac{1}{2}\nu + \mu), -\frac{1}{2}r^2(\nu + \lambda + \mu),$$

$$-\frac{1}{2}r^2\sin^2(\theta)(\nu + \lambda + \mu), -\frac{1}{2}(\nu + \lambda + 2\mu)\Bigg). \tag{37}$$

Therefore, in the unitary gauge, the free parameters of the theory are absent in the field equations and effectively the Fierz-Pauli mass term is rebuilt. In this situation, the equations that should be solved are simplified to the following system of partial differential equations

$$2(\mu - \lambda) + 2r^2\mu_{rr} + 6r\mu_r - 2r\lambda_r + r^2(\lambda_{yy} + 2\mu_{yy}) + m_g^2 r^2(\lambda + 2\mu)) = 0\,, \tag{38}$$

$$2(\lambda - \mu) - 2r\mu_r - 2r\nu_r - r^2(\nu_{yy} + 2\mu_{yy}) - m_g^2 r^2(\nu + 2\mu) = 0\,, \tag{39}$$

$$-r^2(\nu_{rr} + \mu_{rr}) - r\nu_r - 2r\mu_r + r\lambda_r - r(\nu_{yy} + \lambda_{yy} + \mu_{yy}) - m_g^2 r^2(\nu + \lambda + \mu) = 0\,, \tag{40}$$

$$2(\lambda - \mu) - 2r^2\mu_{rr} - r^2\nu_{rr} + 2r(\lambda_r - 3\mu_r - \nu_r) - m_g^2 r^2(\nu + \lambda + 2\mu) = 0\,, \tag{41}$$

$$(\lambda - \mu) = r\mu_r + \frac{1}{2}r\nu_r + f(r)\,, \tag{42}$$

where $f(r)$ is an arbitrary function. The constraint equations (32) and (33) in the unitary gauge are represented by the following equations

$$\nu_r + 2\mu_r = 0, \tag{43}$$

$$\nu_y + \lambda_y + 2\mu_y = 0. \tag{44}$$

The Israel-Darmois junction conditions on the brane are independent of the gauge and are the same as before, that is, Eqs. (34)-(36). The three free parameters of the theory α, β and σ do not exist in the unitary gauge. The general solution of the bulk field equations with the mentioned assumptions that satisfies the constraint equations are obtained as follows

$$\lambda = \mu = a\cos(m_g y) + b\sin(m_g y), \tag{45}$$

$$\nu = -3\mu = -3\Big(a\cos(m_g y) + b\sin(m_g y)\Big), \tag{46}$$

where a and b are integration constants. By putting these solutions into the Israel-Darmois junction conditions, we see that b should be zero. Therefore, the linearized theory in the unitary gauge leads to the following line element on the brane

$${ds_4}^2 = -(1 - 3a)dt^2 + (1 + a)dr^2 + r^2(1 + a)d\Omega^2\,. \tag{47}$$

Actually, this solution after the coordinates redefinition $(t, r) \to (t', r')$, where $t' = (\sqrt{1 - 3a})\,t$ and $r' = (\sqrt{1 + a})\,r$, reduces to the 4D flat Minkowski metric. But, this coordinates transformation leads to the appearance of the temporal component of the Stückelberg fields as

$$\phi^0 = (1 - \eta)t', \qquad \eta = 1 - \frac{1}{\sqrt{1 - 3a}}, \tag{48}$$

and the scalar mode of massive graviton resulting from this Stückelberg field is $\pi = \frac{1}{2}\eta\Lambda^3 t'^2$. The final result is a flat 3-brane solution which is accompanied by the obtained scalar mode.

For the second simplifying assumption, we decided to work in non-unitary gauges. In this case, the free parameters of the theory (α, β, σ) play important roles in characterizing the properties of the solution, such as the (A)dS curvature scale. Moreover, the unknown scalar field $\phi(r)$ is coupled nonlinearly with other unknown metric components which can make the field equations more difficult to solve. We should determine a consistent scalar field $\phi(r)$ together with other unknown functions from field equations. Here, we consider three additional simplifying assumptions. The first one is to assume that the functional $\mu(r, y)$ be just a function of the extra dimension y, which in the non-unitary gauge ($\phi(r) \neq r$) it could be a reasonable assumption. In this situation, solving the field equations could be slightly more easier. Moreover, we can restrict ourself to specific choices of the free parameters. The second assumption is to consider the case $\alpha = \beta = \sigma = 0$, which is equivalent to the choices $\alpha_3 = -\alpha_4 = \alpha_5 = -1$. By this assumption, the effective energy-momentum tensor $\overline{X}_{AB}$ takes the Fierz-Pauli structure, i.e. $\overline{X}_{AB} = \mathcal{K}_{AB} - [\mathcal{K}]g_{AB}$. However, the expression of it's components are not the same as eq. (37), which resulted in the unitary gauge. For this special choices of the free parameters, the components of $\overline{X}_{AB}$ takes the following form

$$\overline{X}_{00} = 3 - \phi' - 2\frac{\phi}{r} + (3 - \phi' - 2\frac{\phi}{r})\nu + \frac{1}{2}\phi'\lambda + \frac{\phi}{r}\mu\,, \tag{49}$$

$$\overline{X}_{11} = -2 + 2\frac{\phi}{r} - \frac{1}{2}\nu - \frac{\phi}{r}\mu + (-2 + 2\frac{\phi}{r})\lambda\,, \tag{50}$$

$$\overline{X}_{22} = r^2\Big(-2 + \frac{\phi}{r} + \phi' - \frac{1}{2}\nu - \frac{1}{2}\phi'\lambda + (-2 + \frac{\phi}{2r} + \phi')\mu\Big)\,, \tag{51}$$

$$\overline{X}_{33} = \sin^2(\theta)\overline{X}_{22}\,, \tag{52}$$

$$\overline{X}_{55} = -3 + 2\frac{\phi}{r} + \phi' - \frac{1}{2}\nu - \frac{1}{2}\phi'\lambda - \frac{\phi}{r}\mu\,, \tag{53}$$

where reduce to (37) for $\phi(r) = r$. The constraint equations (32) and (33) for these special choices of the parameters are

$$2(\phi' - \frac{\phi}{r}) - \frac{1}{2}r\nu_r - \phi\mu_r + (\frac{\phi}{r} - \phi')\mu = 0\,, \tag{54}$$

$$\nu_y + \phi'\lambda_y + 2\frac{\phi}{r}\mu_y = 0. \tag{55}$$

The scalar field $\phi(r)$ is yet stayed coupled with other fields which this makes finding the solutions of the field equations difficult. The third assumption we do is to linearize the field equations with respect to the scalar field by considering $\phi(r) \ll 1$ and ignoring the nonlinear terms in the above equations. Therefore, by imposing these three assumptions we reach to the following field equations that should be solved analytically

$$2(\mu - \lambda) - 2r\lambda_r + r^2(\lambda_{yy} + 2\mu_{yy}) + 2m_g^2 r^2(3 - \phi' - 2\frac{\phi}{r} + 3\nu) = 0\,, \tag{56}$$

$$2(\lambda - \mu) - 2r\nu_r - r^2(\nu_{yy} + 2\mu_{yy}) + 2m_g^2 r^2(-2 + 2\frac{\phi}{r} - \frac{1}{2}\nu - 2\lambda) = 0\,, \tag{57}$$

$$-r^2\nu_{rr} + r(\lambda_r - \nu_r) - r^2(\nu_{yy} + \lambda_{yy} + \mu_{yy}) + 2m_g^2 r^2(-2 + \frac{\phi}{r} + \phi' - \frac{1}{2}\nu - 2\mu) = 0\,, \tag{58}$$

$$2(\lambda-\mu)-r^2\nu_{rr}+2r(\lambda_r-\nu_r)+2m_g^2r^2(-3+\phi'+2\frac{\phi}{r}-\frac{1}{2}\nu)=0\,, \tag{59}$$

$$(\lambda-\mu)=\frac{1}{2}r\nu_r+f(r)\,, \tag{60}$$

$$2(\phi'-\frac{\phi}{r})-\frac{1}{2}r\nu_r=0\,, \tag{61}$$

$$\nu_y=0. \tag{62}$$

These equations are valid in the regions where ν,μ,λ and ϕ are very small. We obtained the following solutions for these linearized field equations

$$\nu(r,y)=a,$$

$$\lambda(r,y)=\mu(r,y)=\frac{3}{4}a,$$

$$\phi(r)=(1+a)r, \tag{63}$$

where a is an integration constant. Note that these solutions are valid in the regions where the obtained $\phi(r)$ is very small, i.e $r\ll\left(\frac{1}{1+a}\right)$. However, the metric here is accompanied by a nontrivial spatial backgrounds for the Stückelberg fields, $\pi^i=x^i-\phi^i=-ax^i,(i=1,2,3)$, where $x^i=(r\sin\theta\cos\phi,r\sin\theta\sin\phi,r\cos\theta)$. The corresponding 4D line element on the 3-brane is given by

$$ds_4{}^2=-(1+a)dt^2+(1+\frac{3}{4}a)dr^2+r^2(1+\frac{3}{4}a)d\Omega^2\,. \tag{64}$$

However, in this case the solution on the brane transforms also to the 4D flat Minkowski metric, after the coordinates redefinition $(t,r)\to(t',r')$ with $t'=\sqrt{1+a}\,t$ and $r'=\sqrt{1+\frac{3}{4}a}\,r$. Due to this coordinates transformation, the temporal and spatial components of the Stückelberg fields will take the following forms

$$\phi'^0=\frac{1}{\sqrt{1+a}}\,t', \tag{65}$$

$$\phi'^i=\frac{1+a}{\sqrt{1+\frac{3}{4}a}}\,x'^i. \tag{66}$$

Finaly, the scalar mode of massive graviton resulting from these Stückelberg fields is

$$\pi=\frac{\Lambda^3}{2}(\delta\,t'^2+\gamma\,x'^2), \tag{67}$$

where the constants δ and γ are related to a via $\delta=1-\frac{1}{\sqrt{1+a}}$ and $\gamma=1-\frac{1+a}{\sqrt{1+\frac{3}{4}a}}$.

In this paper, we considered two simplified linear theories in both unitary and non-unitary gauges and found in both cases a flat solution on the brane with different background Stückelberg fields (after a coordinates redefinition). In non-unitary gauge, we restricted ourself to special choices of the free parameters of the theory. Finding a general analytical solution for the linear theory with arbitrary α, β and σ together with the unknown scalar field $\phi(r)$ and then screening the solution on the brane to be consistent with junction conditions is a very difficult and complicated procedure. However, in the regions where we should

keep nonlinear terms in the field equations, solving them will be more intricate. In this situation, we can pursue alternative approaches, such as solving the equations numerically or finding the effective 4D field equations on the brane for the new braneworld massive gravity theory and then solving them analytically [60, 61]. We are working on these subjects and the outcomes after completion will be presented in another paper.

4 Summary

We know that a way in which a massive graviton can naturally arise is from higher dimensional scenarios, such as KK, ADD and DGP theories. It has been shown that there is a deep connection between the DGP braneworld gravity and massive gravity theories. The graviton in the DGP setup acquires effectively a soft mass and the induced gravity term in the brane action acts as a kinetic term for a 4D graviton, while the bulk Einstein-Hilbert term acts as a gauge invariant mass term. Studying massive gravity from extra dimensional point of view can be useful for better understanding of certain aspects of the dRGT massive gravity theory and its bigravity and multi-gravity extensions. This fact was the original motivation of this paper to construct an extension of massive gravity in the spirit of braneworld scenarios. We have constructed a combination of the braneworld scenario and covariant de Rham-Gabadadze-Tolley (dRGT) massive Gravity, where we suppose that the five-dimensional bulk graviton is massive. We considered a static 5D configuration with spherical symmetry on the brane, aimed at separately determining the effects of bulk graviton mass term and also the large extra dimension on the gravitational interactions on the brane. Then, by a detailed analytical treatment, the effects of the nonlinear ghost-free massive gravity on brane dynamics and effective gravitational potential on the brane are examined. In this manner, the full field equations and their weak field limits together with the generalized Israel-Darmois junction conditions on the brane are presented. This set of equations are so complicated to be solved analytically without some simplifying assumptions. For this reason, by adopting some simplifying assumptions, we were able to find two classes of four-dimensional spherically symmetric solutions on the brane in unitary and non-uniary gauges. Both of them were flat solutions on the brane with different background Stckelberg fields (after a coordinates redefinition). We note that general massive braneworld solutions should reduce to the massless braneworld solution in the limit of zero bulk graviton mass as has been studied in [59]. To restore the GR or the original DGP model on the brane, we should consider certain nonlinear terms in the bulk field equations and the brane junction conditions, which make the solving procedure more difficult (because of the bulk mass terms). We are attempting to follow alternative approaches, such as solving the field equations numerically or finding the effective 4D field equations on the brane for the new massive braneworld theory [60, 61], to examine the Vainshtein mechanism in our model. This issue in the absence of the Boulware-Deser ghost and also the instability issue are subject of our forthcoming work.

References

[1] Riess A. G., et al., 1998, Astron. J, vol. 116, no. 3, pp. 1009-1038.

[2] Perlmutter S., et al., 1999, Astron. J, vol. 517, no. 2, pp. 565-586.

[3] Spergel D. N., et al., 2007, Astrophys. J., Suppl. Ser., vol. 170, no. 2, pp. 377-466.

[4] Csaki C., 2004, "TASI Lectures on Extra Dimensions and Branes," *Shifman, M. (ed.) et al.: *From fields to strings*, vol. 2* pp. 967-1060, [arXiv:hep-ph/0404096].

[5] Maartens R. and Koyama K., 2010, Living. Rev. Relat., vol. 13, no. 5.

[6] Dvali G., Gabadadze G., and Porrati M., 2000, Phys. Lett. B, vol. 485, no. 1-3, pp. 208-214.

[7] Deffayet C., 2001, Phys. Lett. B, vol. 502, no. 1-4, pp. 199-208.

[8] Dvali G. R. and Gabadadze G., 2001, Phys. Rev. D, vol. 63, no. 6, p. 065007.

[9] Deffayet C., Dvali G. R., and Gabadadze G., 2002, Phys. Rev. D, vol. 65, no. 4, p. 044023.

[10] Dvali G. R., Gabadadze G., Kolanovic M., and Nitti F., 2001, Phys. Rev. D, vol. 64, no. 8, p. 084004.

[11] Abbott B. P., et al. [LIGO Scientific and Virgo Collaborations], 2016, Phys. Rev. Lett., vol. 116, no. 6, p. 061102.

[12] Abbott B. P., et al. [LIGO Scientific and Virgo Collaborations], 2016, Phys. Rev. Lett., vol. 116, no. 24, p. 241103.

[13] Abbott B. P., et al., [LIGO Scientific and Virgo Collaborations], 2016, Phys. Rev. Lett., vol. 116, no. 22, p. 221101.

[14] Fierz M. and Pauli W., 1939, Proc. R. Soc. Lond. Ser. A, vol. 173, no. 953, pp. 211-232.

[15] van Dam H. and Veltman M. J. G., 1970, Nucl. Phys. B, vol. 22, no, 2, pp. 397-411.

[16] Zakharov V. I., 1970, JETP. Lett., vol. 12, pp. 312-314.

[17] Vainshtein A. I., 1972, Phys. Lett. B, vol. 39, no. 3, pp. 393-394.

[18] Deffayet C., Dvali G., Gabadadze G., and Vainshtein A., 2002, Phys. Rev. D, vol. 65, no. 4, p. 044026.

[19] Porrati M., 2001, Phys. Lett. B, vol. 498, no. 1-2, pp. 92-96.

[20] Kogan I. I., Mouslopoulos S., and Papazoglou A. 2001, Phys. Lett. B, vol. 503, no. 1-2, pp. 173-180.

[21] Boulware D. G. and Deser S., 1972, Phys. Rev. D, vol. 6, no. 12, p. 3368.

[22] Arkani-Hamed N., Georgi H., and Schwartz M. D., 2003, Ann. Phys, vol. 305, no. 2, pp. 96-118.

[23] de Rham C. and Gabadadze G., 2010, Phys. Rev. D, vol. 82, no. 04, p. 044020.

[24] de Rham C., Gabadadze G., and Tolley A. J., 2011, Phys. Rev. D, vol. 106, no. 23, p. 231101.

[25] Hassan S. and Rosen R. A., 2012, Phys. Rev. Lett., vol. 108, no. 4, p. 041101.

[26] Hassan S., Rosen R. A., and Schmidt-May A., 2012, J. High. Energy. Phys., vol. 1202, p. 026.

[27] Hassan S. and Rosen R. A., 2012, J. High. Energy. Phys., vol. 1204, p. 123.

[28] de Rham C., Matas A., and Tolley A. J., 2014, Class. Quantum. Grav., vol. 31, no. 06, p. 065004.

[29] Gao X., 2014, Phys. Rev. D, vol. 90, no. 6, p. 064024.

[30] de Rham C., 2014, Living. Rev. Relat., vol. 17, no. 7.

[31] Hinterbichler K., 2012, Rev. Mod. Phys, vol. 84, no. 2, p. 671.

[32] Schmidt-May A. and von Strauss M., 2016, J. Phys. A: Math. Theor., vol. 49, no. 18, p. 183001.

[33] Koyama K., Niz G., and Tasinato G., 2011, Phys. Rev. Lett., vol. 107, no. 13, p. 131101.

[34] Koyama K., Niz G., and Tasinato G., 2011, Phys. Rev. D, vol. 84, no. 6, p. 064033.

[35] Nieuwenhuizen T., 2011, Phys. Rev. D, vol. 84, no. 2, p. 024038.

[36] de Rham C., Gabadadze G., Heisenberg L., and Pirtskhalava D., 2011, Phys. Rev. D, vol. 83, no. 10, p. 103516.

[37] D'Amico G., de Rham C. , Dubovsky S., Gabadadze G., Pirtskhalava D., and Tolley A. J., 2011, Phys. Rev. D, vol. 84, no. 12, p. 124046.

[38] Gumrukcuoglu A., Lin C., and Mukohyama S., 2011, J. Cosmol. Astropart., vol. 2011, p. 030.

[39] Arkani-Hamed N., Cohen A. G., and Georgi H., 2011, Phy. Rev. Lett., vol. 86, no. 21, p. 4757.

[40] Arkani-Hamed N., Cohen A. G., and Georgi H., 2001, Phy. Lett. B, vol. 513, no. 1-2, pp. 232-240.

[41] Gruzinov A., 2005, New. Astron., vol. 10, no. 4, pp. 311-314.

[42] Porrati M., 2002, Phys. Lett. B, vol. 534, no. 1-4, pp. 209-215.

[43] Luty M. A., Porrati M., and Rattazzi R., 2003, J. High. Energy. Phys., vol. 0309, p. 029.

[44] Nicolis A., and Rattazzi R., 2004, J. High. Energy. Phys., vol. 0406, p. 059.

[45] Koyama K., 2005, Phys. Rev. D, vol. 72, no. 12, p. 123511.

[46] Nicolis A., Rattazzi R., and Trincherini E., 2009, Phys. Rev. D, vol. 79, no. 6, p. 064036.

[47] Gabadadze G., 2009, Phys. Lett. B, vol. 681, no. 1, pp. 89-95.

[48] de Rham C. , 2010, Phys. Lett. B, vol. 688, no. 2-3, pp. 137-141.

[49] Hassan S. F. and Rosen R. A., 2012, J. High. Energy. Phys., vol. 1202, p. 126.

[50] Hinterbichler K. and Rosen R. A., 2012, J. High. Energy. Phys., vol. 1207, p. 047.

[51] de Rham C. and Gabadadze G., 2010, Phys. Lett. B, vol. 693, no. 3, pp. 334-338.

[52] Randall L. and Sundrum R., 1999, Phys. Rev. Lett., vol. 83, no. 17, p. 3370.

[53] Chacko Z., Graesser M. L., Grojean C., and Pilo L., 2004, Phys. Rev. D, vol. 70, no. 8, p. 084028.

[54] Gherghetta T., Peloso M., and Poppitz E., 2005, Phys. Rev. D, vol. 72, no. 10, p. 104003.

[55] Kakushadze Z., 2014, Acta. Phys. Pol. B, vol. 45, pp. 1671-1699.

[56] Kluson J., 2011, Class. Quantum. Grav., vol. 28, no. 15, p. 155014.

[57] Iglesias A. and Kakushadze Z., 2010, Phys. Rev. D, vol. 82, no. 12, p. 124001.

[58] Iglesias A. and Kakushadze Z., 2011, Phys. Rev. D, vol. 84, no. 8, p. 084005.

[59] Nozari K. and Asaiyan A., 2011, Class. Quantum. Grav., vol. 28, no. 12, p. 125017.

[60] Shiromizu T., Maeda K., and Sasaki M., 2000, Phys. Rev. D, vol. 62, no. 2, p. 024012.

[61] Maeda K-i., Mizuno Sh., and Torii T., 2003, Phys. Rev. D, vol. 68, no. 2, p. 024033.

[62] Do T. Q., 2016, Phys. Rev. D, vol. 93, no. 10, p. 104003.

[63] Dadhich N., Maartens R., Papadopoulos P., and Rezania V., 2000, Phys. Lett. B, vol. 487, no. 1-2, pp. 1-6.

[64] Kofinas G., Papantonopoulos E., and Zamarias V., 2002, Phys. Rev. D, vol. 66, no. 10, p. 104028.

[65] Middleton C. and Siopsis G., 2004, Mod. Phys. Lett. A, vol. 19, no. 30, p. 2259.

[66] Gregory R., 2009, Lect. Notes. Phys., vol. 769. pp. 259-298.

[67] Berezhiani L., Chkareuli G., de Rham C., Gabadadze G., and Tolley A. J., 2012, Phys. Rev. D, vol. 85, no. 4, p. 044024.

[68] Babichev E. and Brito R., 2015, Class. Quantum. Grav., vol. 32, no. 15, p. 154001.

[69] Tasinato G., Koyama K., and Niz G., 2013, Class. Quantum. Grav., vol. 30, no. 18, p. 184002.

[70] Babichev E. and Fabbri A., 2014, J. High. Energy. Phys., vol. 1407, p. 016.

[71] Babichev E. and Fabbri A. , 2014, Phys. Rev. D, vol. 90, no. 8, p. 084019.

[72] Cai R. G., Hu Y. P., Pan Q. Y., and Zhang Y. L., 2015, Phys. Rev. D, vol. 91, no. 2, p. 024032.

[73] Xu J., Cao L. M., and Hu Y. P., 2015, Phys. Rev. D, vol. 91, no. 12, p. 124033.

[74] Zhou Z., Wu J. P., and Ling Y., 2015, J. High. Energy. Phys., vol. 1508, p. 067.

[75] Hendi S. H., Eslam Panah B., and Panahiyan S., 2015, J. High. Energy. Phys., vol. 1511, p. 157.

[76] Ghosh S. G., Tannukij L., and Wongjun P., 2016, Eur. Phys. J. C, vol. 76, no. 3, p. 119.

[77] Do T. Q., 2016, Phys. Rev. D, vol. 94, no. 4, p. 044022.

[78] El-Menoufi B. K. and Sorbo L., 2015, Phys. Rev. D, vol. 91, no. 6, p. 064023.

Iranian Journal of Astronomy and Astrophysics
Vol. 3, No. 2, Autumn 2016

Iranian Journal of Astronomy and Astrophysics

Simulation Calibration of an Extensive Air Shower array, by a logged data set of its small prototype

M. Khakian Ghomi
Energy engineering and physics department, Amirkabir univ. of tech., 15875-4413, Tehran, Iran; email: khakian@aut.ac.ir

Abstract. Alborz observatory is an EAS array in the heights of Alborez mountain chain near Tehran. For the development of the array, more number of detectors is inevitable. The managing the financial resources and achieving the highest efficiency of the array is important for the project. Therefore, Water Cherenkov Detectors has been used for 9 months in the same way as the previous experiment with Scintillation Detectors in a 4-fold square arrangement. After a hardware calibration procedure, the experimental data set was simulated by CORSIKA code and the experimental restrictions were applied over the data set. In this work, the simulation is calibrated with the real experimental results, and it presents a comparable parameter between the experiment and the simulation. The obtained results show that the simulation is in agreement with the experimental results.

Keywords: Extensive Air Shower (EAS), Cosmic Rays, Water Cherenkov Detector(WCD)

1 Introduction

Alborz observatory[2] is an Extensive Air Shower (EAS) array of particle detectors, in the range of UHE cosmic and gamma rays, located near Tehran ($35^\circ N$, $51^\circ E$) at an altitude of 2650m a.s.l. Based on the models of EASs, the altitude is around the shower maximum of Cosmic Ray(CRs) with 10^{17} to 10^{18} eV [1, 2, 3, 4, 5]. In this energy range and with the area of the observatory ($\sim 2\times10^5$ m^2), detection rate is a very rare event [3]; but the array is able to detect lower energy CRs[3]. Lower threshold energy of a prototype array of a 4-fold square shaped NaI scintillation detectors, is about 5×10^{13} to 10^{14} eV[6, 7]. The development of the array in a larger area with more number of detectors increases the event rate and makes more accurate results due to its more rich data[8]. Many aspects of particle scintillation detector(SD) parameters and their effects on the detection efficiency have been the subject of many studies[9, 10]. To apply more detectors in the array, it is needed to have a suitable simulation for the experiment. Since large number of SDs cost too much, they are not an accessible choice for the future plan of the observatory. Water Cherenkov Detector (WCD) is a less expensive alternative. The alternative is sometimes used by other scientists for detection of charged particles via detection of cherenkov radiation inside water[11, 12, 13]. The WCD is a cylindrical water tank, which is more accessible and cheaper in comparison with the SDs. Therefore, the detector was studied with more details in some independent experiments for the WCD individually[14, 15]. In the next step, its operation investigated in an array of WCDs similar to the SD array[6] because there was a good experience with the array of SDs[15, 16, 19, 20].

[2]http://www.sina.sharif.ir/õbservatory

In fact, this work, tries to answer the question: "*Could the WCDs be as confident as SDs in the array arrangement?*".
Obtained results from the WCD experiment, showed a good agreement with the SD experiment. Of course there are some differences which are mostly due to the different geometry and different detection procedures of WCDs and SDs[6].
Detection mechanisms of charged particles by SDs and WCDs are quite different[21]. The arrangement of the two arrays (SDs and WCDs) are the same but dimensions of the WCDs are different from SDs. Target of this work, is the calibration of the simulation, by the obtained results of the prototype WCD experiment.
In the 2nd section, the experimental arrangement is briefly introduced. 3rd section studies the error estimation of the experiment. In section 4, simulation procedure of the experimental events is presented in two steps; generation of the events by CORSIKA code[24] and application of the experimental restrictions over the simulated events. The fifth section compares the results of the simulation and the experiment. And finally in the last section, some discussions about the results and future plans are presented. Also in this section, few comments been proposed to have more efficient simulations in the future.

2 Experimental arrangement

A 4-fold square array of WCDs with the side of 6.08m is located on horizontal surface of the physics department roof at Sharif University of Technology (35°43′N, 51°20′E, 1200m ≡ 890 gr/cm^2). Each detector is a cylindrical metallic reservoir painted white inside, with 64cm diameter and 120cm height, it contains about 380 liters of sealed water (Figure 1a). There is a 52mm EMI 9813B PMT (www.electronictubes.com) faced inside water[6] at the center of upper surface of the WCDs.
If at least one charged particle passes through the water, its Cherenkov blue light radiation (in the range of 470nm) is enough to turn the PMT on[14]. An investigation on a single WCD has shown that more than 90% of particles passing through the WCD are detectable[15]. The PMT output pulse height is related to:
i) direction, *ii*) number and *iii*) location of the passed particles through each WCD[15].
The used PMTs have amplification factor of 1×10^8 and its supporter electronics is a set of NIM modules and a Multi Channel Analyzer(MCA) (Figure 1b). It is used 4 fast Discriminator (CAEN N413A) operating at fixed levels around 35mV to 200mV. The thresholds are set to separate signals from background noise. The 4 Discriminator outputs fed into 3 Time to Amplitude Converters (TAC)(EG&G ORTEC 566) which are set to 200ns full scale (Maximum acceptable time differences between each two WCDs). Therefore, it is obtained 3 Δts (Δt_{31}, Δt_{32} and Δt_{34}) which are fed into 3 TACs (1 to 3 in Figure 1b). Meanwhile it was recorded true time (GMT) of each EAS event (T_{GMT}) with the accuracy of synchronized computer with the site www.timeanddate.com. TAC outputs are fed into a Multi parameter MCA (KIAN AFROUZ Inc.) via an Analogue to Digital Converter (ADC)(KIAN AFROUZ Inc.). The first triggered case is on the first parameter (Δt_{31}). When it turns on, the event will be recorded and selection of true events is postponed to off-line parts. Usually in large arrays there are some problems like memory and off-line processing ones with the recorded large date sets. Since our experimental arrangement has not the problems, therefore, it was applied a soft trigger case to record the events. Meanwhile, this condition needs a poor logic and less electronic modules too. A total of 30 experiments have recorded 1,768,195 events in 12,258,670.0 seconds for about nine months. Off-line triggering condition has eliminated any event which has any null Δt's. This step eliminated most of the useless events. Some more refinements are used to improve the accuracy of the data set. Finally it was obtained

476,675 true EAS events ($\sim 27\%$) with the rate of 0.0389 Hz. In section 4.2.2 the number of triggered cases is applied on the simulation. The number of triggered cases in the simulation is: *turn on all of the 4 detectors on a square configuration like the experiment.*

3 Error investigation

3.1 Independency of the experimental events

Primary cosmic rays with different sources miss their directions due to the magnetic field or other effects on their path. When an EAS is recorded, it is expected that the event should be quite independent from the other recorded events. To verify the in-dependency, the rate and time separation between consequent events were studied. These sequential events are between each two, three, four, five and six member sequences.
Figure 2(a) shows the distribution of time differences between each two consecutive events (Δt_1) which has a good agreement with exponential distribution function $F(\lambda_1) = Aexp(-\lambda_1 \Delta t_1)$ with $\lambda_1 = 0.0391$ Hz. Meanwhile, it is obtained $\Delta t_m = t_i - t_{i-m}$ with (m=) 2, 3, 4 and 5. Figure 2(b) shows a good agreement between the obtained results and Gamma-Function

$$G(\Delta t_m, \lambda_m, m) = \frac{\Delta t_m^{m-1}}{(m-1)!} N \lambda_m^m exp(-\lambda_m \Delta t_m) \quad (1)$$

where $\bar{\lambda} = 0.0395 \pm 0.0002$ Hz for the obtained 5 λs. Therefore, the events are quite random. CORSIKA code uses a random generator with 10^9 sequence length loop for generation of simulated events[24] which guarantees the in-dependency of the events.

3.2 Angular resolution of the experiment

Calculated errors of the array with scintillation detectors are investigated from error propagation of all of experimental parameters over the angular resolution of the experiment which is 5.0°[16]. In the WCD, error propagation procedure, causes $7.2^\circ \pm 1.0^\circ$ for the angular resolution of WCD array[6]. The different angular resolutions of the the SD and WCD arrays, are due to the different geometries and dimensions of the SDs and WCDs. In follow, it seems that it is better to use a binning with at least 6.2° intervals. Since in the SD experiment[16] it has been calculated error of the experiment by error propagation procedure equal to 5.0° and after it, in another work, but with the data set and with moon shadow effect, it has been obtained 4.5°[17] angular error. Therefore, in this investigation it is used a smaller 5° binning for the events.

4 Simulation of the experimental events

The simulation contains two parts:
The first one is generation of some CORSIKA simulated events(SEs) comparable with the number of experimental events. It should be suggested that the creation time of the data set with a normal PC was as long as the experimental duration itself.
In the second part of the simulation, the experimental constrains were applied to the created events. In this part the calculations over the simulated data set are exactly the same as calculations on the data set of the real experimental events.

4.1 Generation of the CORSIKA simulated events

A sum of 392,200 CORSIKA (V6204 code) events were simulated for a flat surface[24]. GHEISHA and QGSJET models were used for low and high energy ranges of hadronic interactions respectively. Below the knee, about 90% of primary cosmic rays are Protons, 10% are α particles (Helium nucleus) and less than 1% contains heavier elements[3, 21, 25]. Therefore, it was considered the primary cosmic ray composition $(90\%, 10\%, 0\%)$ in the simulation.
These SEs are created for the array site (University site) with 1200 m a.s.l., $B_x = 28.1$ μT and $B_z = 38.4$ μT (Figure 1), and energy distribution power is $dN/dE \propto E^{-2.7}$.
Azimuth angles of the SEs are from 0 to 360° uniformly. CORSIKA random generator considers $dN/d\theta = A \sin\theta \cos\theta$ for zenith angle distribution of the SEs[24]. Zenith angle of the SEs were considered from 0 to 60°.
Lower and higher energy thresholds of the simulation were considered as 50 TeV[16] to 5 PeV (few events per experimental duration) without thinning. Also as an input information for the simulation, it was considered energy cuts for hadrons, muons, electrons and photons 0.3, 0.3, 0.003 and 0.003 GeV, respectively.

4.2 Application of the experimental restrictions over the SEs

This part was divided into three sub-parts.
i) Calculation of effective surface of the WCD for each SE, individually.
ii) Application of experimental trigger condition over each SE.
iii) Finding a comparative parameter to compare the simulation and experimental results.

4.2.1 Calculation of effective surface of the WCDs for each SE

CORSIKA code creates SEs for a flat surface and flat detectors[24]. The generated EAS events, are recorded in a square format with the accuracy of 1cm. Therefore, it is needed to calculate the equivalent effective surface of the WCDs as a flat square detector in different angles. Since the WCDs are 3 dimensional, effective surface of the WCDs depends on zenith angle of the events (Figure1c), therefore, zenith distribution function of the events will be:

$$dN/d\theta = A \sin\theta A_{eff}(\theta) \cos^{(n-1)}\theta. \tag{2}$$

Where "A" is the proportionality constant, $\sin\theta$ is due to the FOV of the array; A_{eff} is the effective surface of the WCD, and $\cos^{n-1}\theta$ is due to the atmospheric thickness effect[6]. The effective surface $A_{eff}(\theta)$ is:

$$A_{eff} = P_0 A_0 \cos\theta + P_{90} A_{90} \sin\theta \tag{3}$$

where A_0 and A_{90} are surfaces of the WCD for 0° and 90° zenith angle events respectively. Also P_0 and P_{90} are detection probabilities in these angles where $P_0/P_{90} = 2.1$[15].

4.2.2 Application of trigger case over each SE

An EAS event (in 50 TeV to 5 PeV energy ranges) extends on a vast region on the ground (more than a few kilometers in radius) but there is a very low surface density at larger radii. A large square array composed of cells of size A_{eff} are considered as a Simulated Detector Array (SDA)(Figure 3). The center of each SE is projected on the center of the related SDA. In an independent simulation for one of the WCDs[15] it is obtained that the response of the WCD for a charged particle is more than 90%[23]. Therefore, in the SDA the response

of each virtual WCD (VWCD) is considered to be 1. It is assumed that if a charged particle passes through a VWCD, it will be detected.
Trigger condition for each SE is the same as in section 2. In the experiment, an event is accepted if all of the 4 WCDs record, passing of at least one charged particle. Now in the simulation, the condition is applied again for VWCDs. If an EAS event satisfies at least one square configuration like the experiment (Figure 3 shows 2 triggered cases) essentially it might be detected by the array, and if the number of the triggered cases increases, detection probability will be increased. From the projected data over VWCDs, it is possible to calculate zenith(θ) and azimuth(ϕ) angles of each SE, exactly the same as calculations for the experimental events[6]. In this method, it has been calculated zenith and azimuth angles (θ, ϕ) of each SE by least square method[26, 27].
Since the number of VWCDs increases with the second power of the SDA size, it is efficient to obtain a better estimation about the size of the SDA before starting the simulation. Since it should be estimated the SDA size for all of the SEs, therefore, it was calculated a weighted mean size $\bar{l}_{WCD} = \sqrt{\bar{A}_{eff}}$, which is used for mean length of each VWCD with the mean area of $\bar{A}_{eff}$ in the SDA:

$$\bar{A}_{eff} = \frac{\int_0^{\pi/3}(P_0 A_0 \cos\theta + P_{90} A_{90} \sin\theta)\sin\theta d\theta}{\int_0^{\pi/3}\sin\theta d\theta} = 0.65 \text{ m}^2. \quad (4)$$

$\bar{l}_{WCD}$ is equal to $\sqrt{0.65} = 0.81$m.
Therefore, it was calculated mean density of particles per each VWCD for 50,000 random SEs, vs. radius from shower core. Figure 4 shows density of charged particles per each VWCD. At $r = 500 \times \bar{l}_{WCD}$ the density about 0.47 particle per A_{eff}. Therefore, probability of trigger cases of the experiment (turning on four VWCDs in a square configuration) becomes less than a few percent in larger radii. Therefore, the SDA was considered 1000×1000 square shaped detectors (Figure 3).

4.2.3 A comparative parameter between the SEs and the experimental events

Thickness of EAS front at the center, is less than a meter ($\sim$ a few ns) and at the outer regions around a few meters ($\sim$ a few 10ns)[1, 3, 21, 28]. In the 4-fold WCD experiment Δts at the order of ten nanoseconds, in a TAC duration of 200ns (more details in section 2). TAC starts when the first particle of EAS front passes through the start detector and it stops when the stop detector receives its first particle. Therefore, the experiment is only able to detect the first particle passes through each WCD. So in the SDA, it will be recorded only time of the first particles hits on each VWCD.
Now the experimental trigger condition is applied for the SDA from the first VWCD (up-right corner pixel (-500,-500)) until the last one (bottom-left corner (500,500)) (Figure 3) and scans all the SDA. Number of triggered squares (N_{trig}) over each SE, could be a parameter to compare the SE and a real EAS event. The parameter seems to be related to detection probability of the SE. In each SE "the number of triggered cases", was calculated a direction. For each SE there are N_{trig} independent directions (θs and ϕs). Since detection efficiency of the charged particles is high, therefore, the edge of the front will be detected and the calculated directions of the shower by a small array is on the normal to the shower edge. Therefore, when it is averaged over all of the directions of the triggered conditions, the directions are axisymmetric and the distribution of the obtained directions around the primary direction is a symmetric peak function[30, 31] and may be there is a large error bar for the obtained direction, but the real direction of the EAS is near to the average. Since it is not well known which of the squares is matched on the experimental arrangement, therefore,

average of the directions is considered as the direction of the SE and standard deviation of the directions will be angular resolution of the SE. To calculate the angular resolution of the events in each 5° bins, it is calculated $\bar{\sigma} = \sqrt{\Sigma\sigma_i^2/N}$, where σ_i is angular resolution of each SE and N is the number of SEs in each 5° bin. This is due to the stochastic nature of the CORSIKA SEs specially by hadronic primary particles and their conic front shape.

5 Experimental and Simulation results

The first subsection is specified the N_{trig} as detection probability, then in the next subsections the parameter is used for comparisons between the simulation and the experiment. Importance of the parameter N_{trig}, depends on the compatibility of the simulation predictions and experimental results.

5.1 Specification of N_{trig} with comparison of the experiment and simulation

On each SE, all of the triggered cases over the SDA are considered one by one. From the N_{trig} conditions in each SE, N_{trig} number of θs and ϕs are obtained. Therefore, $\bar{\theta} \pm \sigma_\theta$ for zenith angle of each SE were calculated as follows:

$$\bar{\theta} = \frac{1}{N_{trig}} \Sigma_{i=1}^{N_{trig}} \theta_i, \quad \sigma_\theta = \sqrt{\frac{\Sigma_{i=1}^{N_{trig}} (\theta_i - \bar{\theta})^2}{N_{trig}}} \tag{5}$$

In 11 steps it was applied lower threshold of N_{trig} from 1 to 11 one by one. By fitting the equation 2 on the 11 distribution it was obtained 11 cosine power 'n' which were drawn in Figure 5. By fitting an arbitrary function ($y^2 = a + b \ln x$) with the best fit ($r^2 = 0.99904$) and with $n = 6.8 \pm 0.1$[6], $N_{trig} = 6.82 \pm 2.11$ was obtained. Therefore, $N_{trig} = 6.82 \approx 7$ shows the most compatible distribution of detectable SEs with the experiment; therefore, $N_{trig} \geq 7$ are considered as detectable SEs.

5.2 Estimation of energy threshold of the experiment by the detectable SEs

To check the number of triggered cases as a candidate for the detection probability in the simulation, it is better to estimate the threshold energy of the SEs with $4.71 \leq N_{trig} \leq 8.93 \equiv N_{trig} \in \{5, 6, 7, 8\}$ ($N_{trig} = 6.82 \pm 2.11$).
In the WCD experiment, threshold energy was $E_{th} \approx 95\ TeV$[6]. For estimation of the E_{th} from the simulation, it was averaged over the energy of events with $N_{trig} \in \{5, 6, 7, 8\}$, which in the 392,200 SEs, there are 11,553 events. Average energy and standard deviation of the events are $\bar{E}_{th} \pm \sigma_{th} = 108.09 \pm 117.63$ TeV. More detailed is shown in Table 1. It is seen that $\bar{E}$ has small fluctuation between 106.86 and 111.12 for $N_{trig} \in \{5, 6, 7, 8\}$. The large standard deviations are due to:
i) the stochastic nature of the simulated events;
ii) large zenith angle events ($40 \leq \theta \leq 60$) with higher energies up to 5 PeV with small N_{trig}.
Effects of zenith angle and energy will be discussed in subsection 5.3.

N_{trig}	#	$\bar{E}$	σ_E
5	3538	106.93	126.67
6	3012	111.12	122.41
7	2575	107.32	114.20
8	2428	106.86	100.14

Table 1: Number, Mean Energy and Standard deviation of energy of events(σ_E) with N_{trig}=5 to 8 individually. This results show that the threshold energy of the experiment is about 100 TeV.

	N_{tot}	$N_{(0\leq\theta\leq40^\circ)}$	$N_{(40^\circ\leq\theta\leq60^\circ)}$	$N_{(40^\circ\leq\theta\leq60^\circ)}/N_{tot}$
SE_{all}	392200	215852	176348	44.96%
$SE_{N_{sq}\geq7}$	109440	100668	8752	8.00%

Table 2: In all of SEs 45% of the events are in the zenith angles $40 \leq \theta \leq 60$ in case that in the detectable events there is only 8% of the total events in zenith angles $40 \leq \theta \leq 60$.

5.3 Zenith angle effect on the parameter N_{trig}

From the 392,200 SEs 242,308 of them are null events and have no triggered cases ($N_{trig} = 0$)! This means that about 61% of the SEs are not detectable at all. So the question is *"why is the high fraction not detected?"*. Average zenith angle of the null events is $\bar{\theta}_0 \pm \sigma_{\theta_0} = 43.55^\circ \pm 11.58^\circ$, in case that, all SEs have $\bar{\theta}_{tot} \pm \sigma_{\theta_{tot}} = 36.56^\circ \pm 14.43^\circ$. Also for 53,212 higher energy null events ($E \geq 100$ TeV), there is $\bar{\theta}_0 \pm \sigma_{\theta_0} = 47.74^\circ \pm 8.67^\circ$ but for 55,217 higher energy ($E \geq 100$TeV) detectable events with $N_{trig} \geq 7$ there is $\bar{\theta}_{det} \pm \sigma_{det} = 25.91^\circ \pm 11.18^\circ$. Figure 6 shows that higher energy events with larger zenith angles seems to be more fret, and triggered cases become harder for them.
CORSIKA selects the primary zenith angle of the events with the distribution of $\sin\theta\cos\theta$[24]. Maximum of the distribution $\sin\theta\cos\theta$ is on the 45° and contribution of the total events in the interval $40^\circ \leq \theta \leq 60^\circ$ is about 45%, in Table 2 it is seen that detectable events in the interval are only about 8%. Therefore, as a result:
i) higher energy events with higher zenith angles make a large uncertainty over the energy threshold.
ii) for more efficient simulations, it is better to simulate smaller zenith angle events ($0 \leq \theta \leq 40^\circ$).

5.4 Observation of atmospheric optical thickness for detectable events

Secondary particles of real EAS events with higher zenith angles, have longer paths in the atmosphere. So higher zenith angle EAS events have less secondary particles and fret particle densities at the ground[29, 32]. In visible astronomy there is a well known parameter as *air mass* which decreases the light intensity of astronomical sources exponentially with $\sec\theta$[33]:

$$I = I_0 e^{-\tau_0 \sec\theta}. \tag{6}$$

In the astroparticle field, slant depth ($X = \int \rho dv$) plays the role of air mass in visible astronomy. In the SEs it is expected that increase of zenith angle of the events decreases N_{trig}. Figure 7 shows mean number of triggered case (N_{trig}) for the events with $N_{trig} \geq 7$ for 5° intervals. It is seen that there is a compatibility ($r^2 = 0.93202$) of the equation 6 with $N_{trig}(\theta)$.

	N_{tot}	$N_{(50\leq E\leq 100)\text{TeV}}$	$N_{(100\leq E\leq 5000)\text{TeV}}$	$N_{(100\leq E\leq 5000)\text{TeV}}/N_{tot}$
SE_{all}	392200	271664	120536	30.73%
$SE_{N_{trig}\geq 7}$	109440	54223	55217	50.45%

Table 3: In all of SEs 70% of the events are in the energy range $50 \leq E \leq 100$ TeV it is in case that in the detectable events there is only 50% of the total events are in in the energy range $50 \leq E \leq 100$ TeV.

5.5 Effect of primary energy of SEs on N_{trig}

Figure 8 shows the distribution of the null SEs ($N_{trig} = 0$) near to the lower threshold of the simulation. It is observable that the distribution is decreasing steeply by a power law. Average and standard deviation of these events are $\bar{E}_0 \pm \sigma_0 = 90.78 \pm 78.50$ TeV. It is expected that higher energy events have more secondary particles, so they are more detectable. Figure 9 shows, N_{trig} increases with increase of energy. Higher energy particles have larger number of secondary particles, so detection probability increases with increase of energy. Of course large error bars are due to: *i*) zenith angle effect and *ii*) smaller statistics at higher energies.
Table 3 shows that if 50 TeV threshold energy is replaced by 100 TeV, the simulation will be considered more efficiently.

6 Conclusion

Simulation in experimental researches is the second wing of the experiment. The simulation should be completely harmonized and calibrated by the experiment. In this work to verify the simulation and its calibration, it was used the CORSIKA code to generate of a set of simulated events and compared the obtained results with the experimental ones. It was found a parameter which is "the number of triggered cases" in the simulation (N_{trig}). The obtained results show that the N_{trig} is proportional to detection probability of the experiment. Some results are:
Ri) Higher zenith angle events are less detectable exponentially with $\sec\theta$ similar to $air - mass$ effect.
Rii) Energy threshold of the experimental events and the SEs are near to each other.
Riii) The most important obtained result is the compatibility of the simulation with the experiment.
Of course for more accurate analysis in the future, it is better to repeat the simulation more efficiently. Since the generation of the simulated events is a time and memory consuming work, some comments are proposed for the future investigations:
*C*1) It is more efficient in time and memory to simulate lower zenith angle events ($0 \leq \theta \leq 40^\circ$).
*C*2) It is better to apply threshold energy equal to 100 TeV, lower than this amount is eliminated
Generated hadronic events by CORSIKA code, have a stochastic nature and their fluctuation is high, therefore, it is better to simulate as much as possible in the future plans for more confidence (specially in the recommended angle and energy domains).

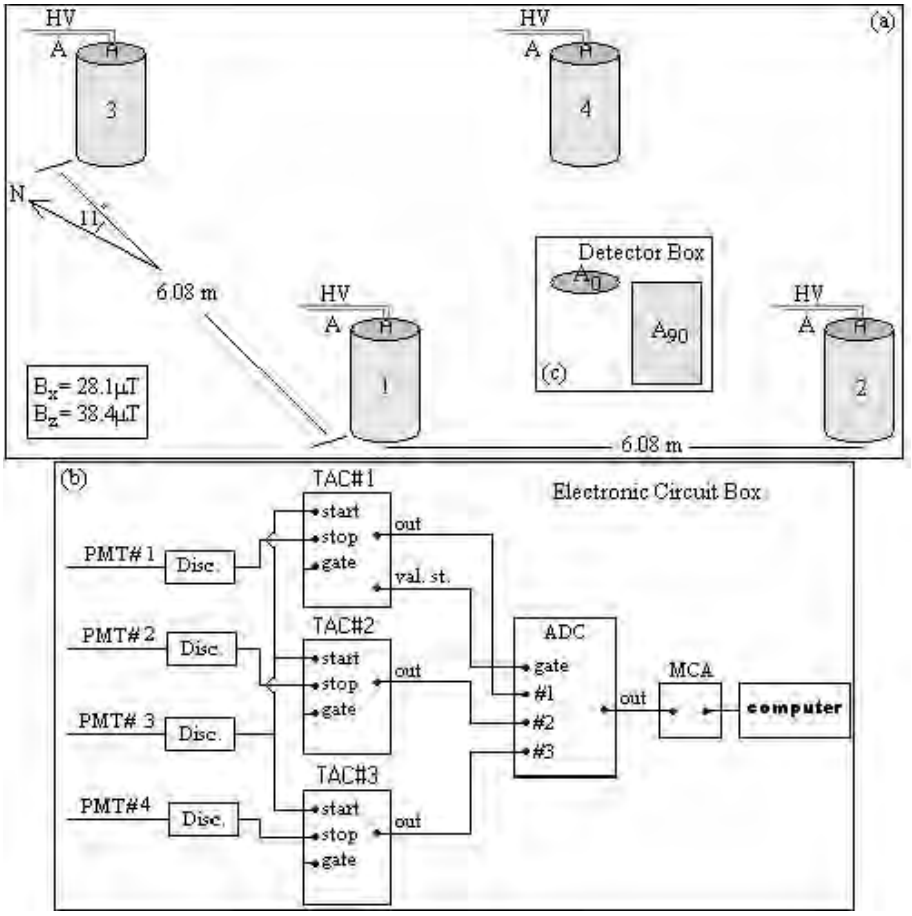

Figure 1: Different parts of the figure respectively show (a): Schematic configuration of the detector array, (b): Data acquisition system and used electronic circuits, (c)(inside a): Vertical (A_0) and horizontal (A_{90}) sections of the WCDs.

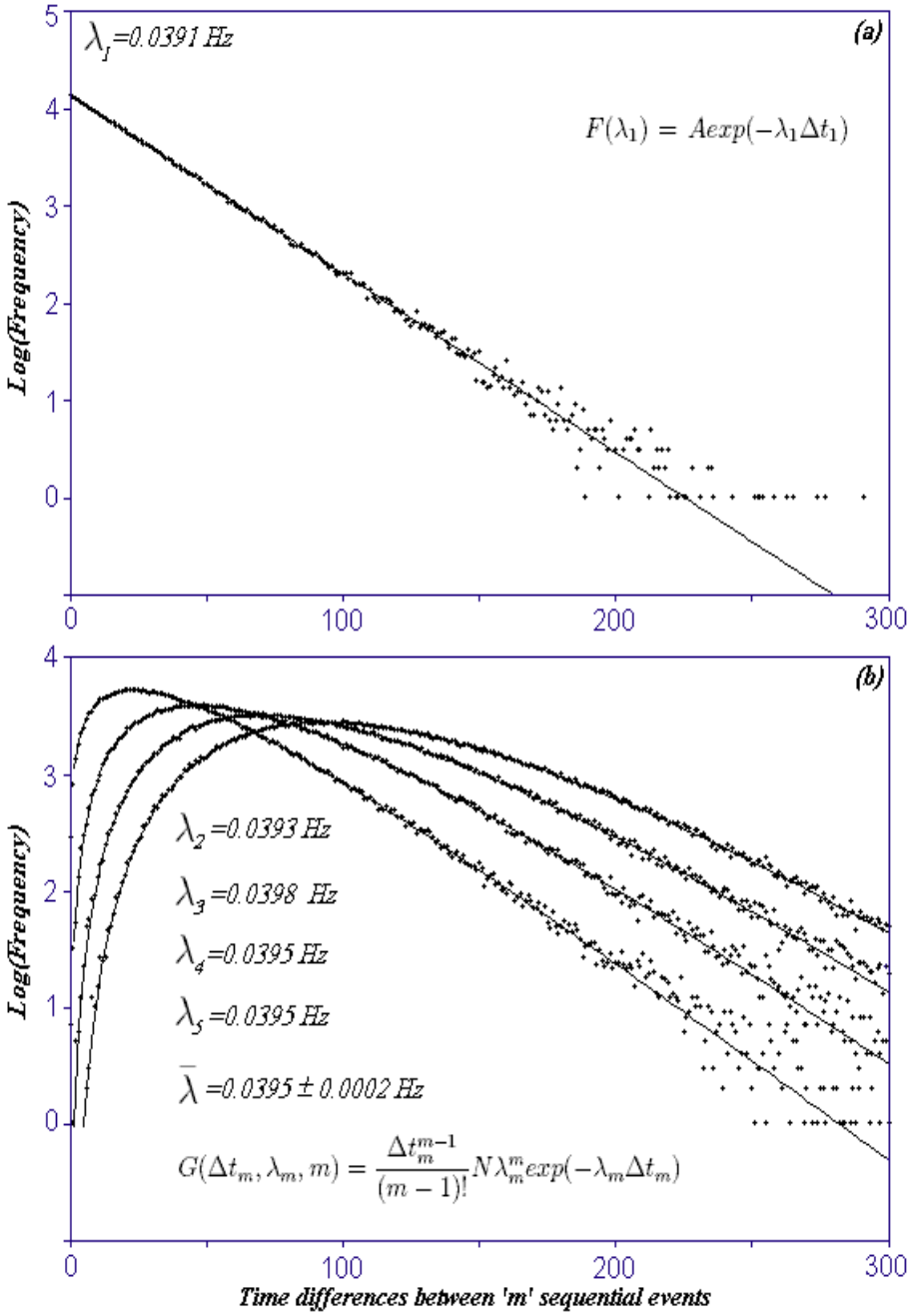

Figure 2: a) The fitted exponential function on the true time(GMT) differences of each two following events. b) Time differences between 2, 3, 4 and 5 sequential events.

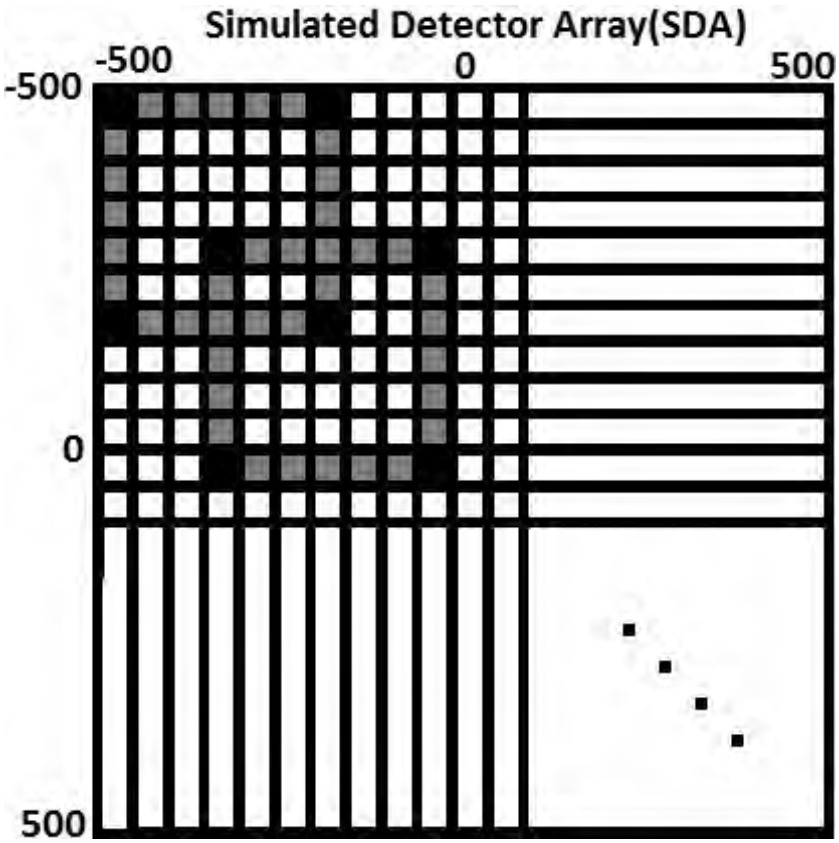

Figure 3: The SDA (-500:500×-500:500) with VWCD size $l_{WCD} = \sqrt{A_{eff}}$ meters. In this part it is shown two triggered case samples of the simulation.

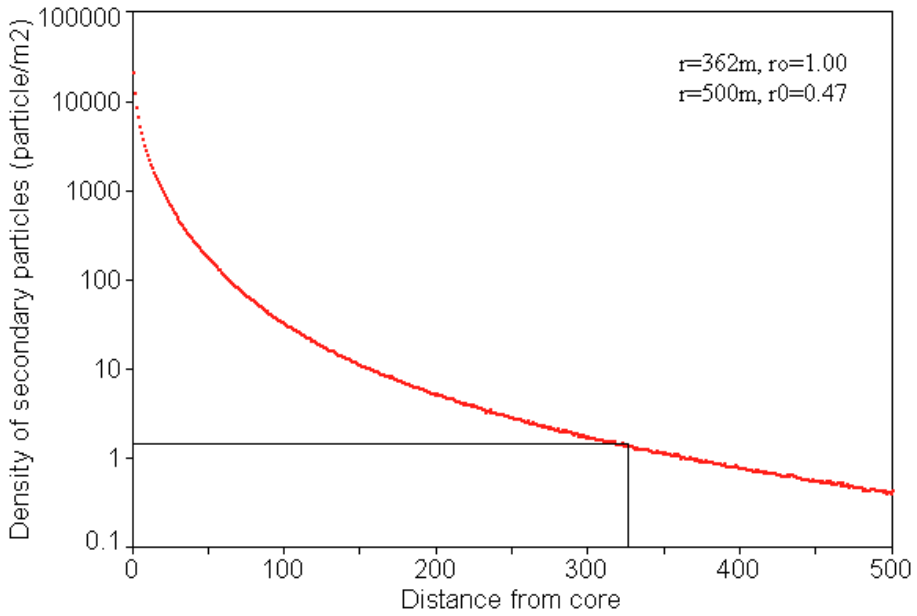

Figure 4: Secondary particle density function in particle/m^2. WCDs have mean cross section $\bar{A}_{eff} = 0.65 m^2$. Therefore the density $1/0.65 = 1.54$ particles per WCD is the least density which must be considered in our simulation. This radius is 266 m $= 328 \times \sqrt{\bar{A}_{eff}}$. In the simulation it has been considered until $500 \times \sqrt{\bar{A}_{eff}} = 0.47$ particles per each VWCD.

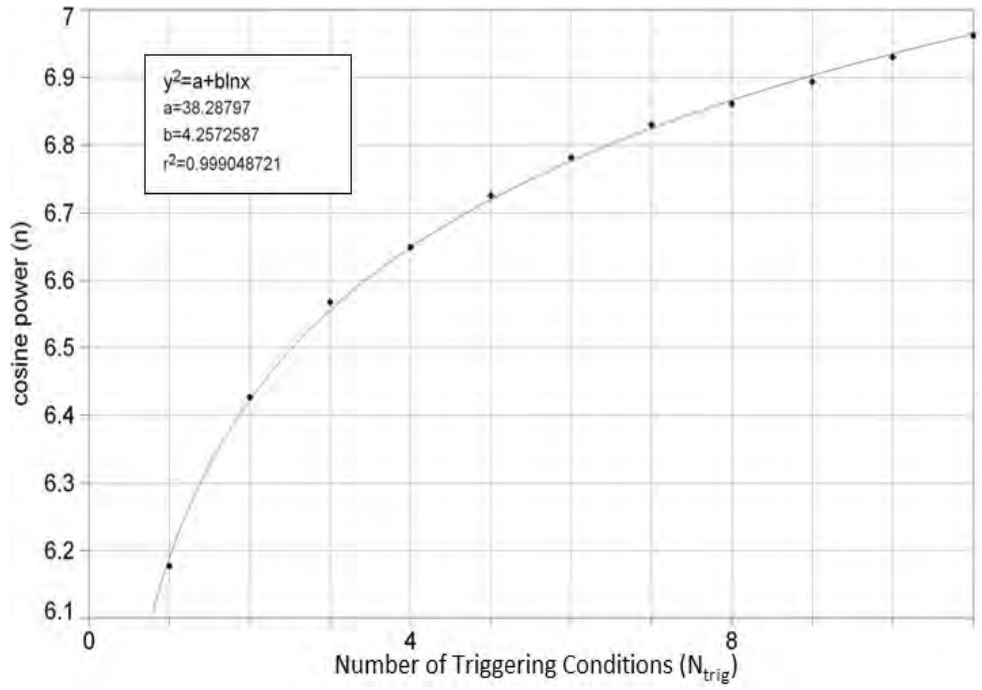

Figure 5: By variation of the lower threshold over N_{trig} and fitting $dN/d\theta$ on the obtained distributions, it is found the first 11 powers (n). Comparison of the simulated results and the experimental results ($n_{exp} = 6.8 \pm 0.1$) shows that, the nearest SE distribution to the experimental data set, is set of SEs with $4.71 \leq N_{trig} \leq 8.93 \equiv N_{trig} \approx 6.82 \pm 2.11$. Therefore detection condition is considered as $N_{trig} \geq 7$.

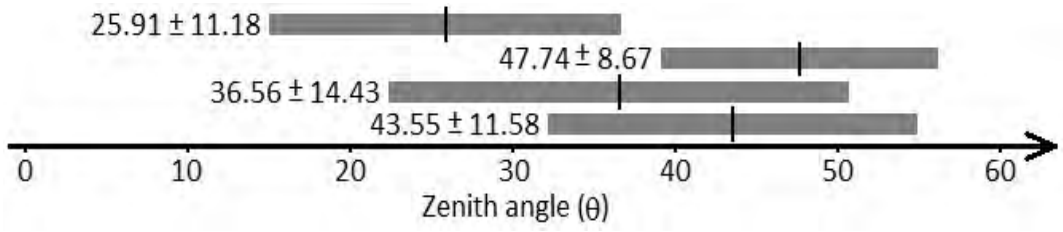

Figure 6: Average zenith angle of: the null SEs is $\bar{\theta}_0 \pm \sigma_{\theta_0} = 43.55^\circ \pm 11.58^\circ$, all SEs have $\bar{\theta}_{tot} \pm \sigma_{\theta_{tot}} = 36.56^\circ \pm 14.43^\circ$, 53,212 high energy null SEs ($E \geq 100$ TeV), $\bar{\theta}_0 \pm \sigma_{\theta_0} = 47.74^\circ \pm 8.67^\circ$, 55,217 high energy ($E \geq 100$ TeV) detectable SEs $N_{trig} \geq 7$, $\bar{\theta}_{det} \pm \sigma_{det} = 25.91^\circ \pm 11.18^\circ$.

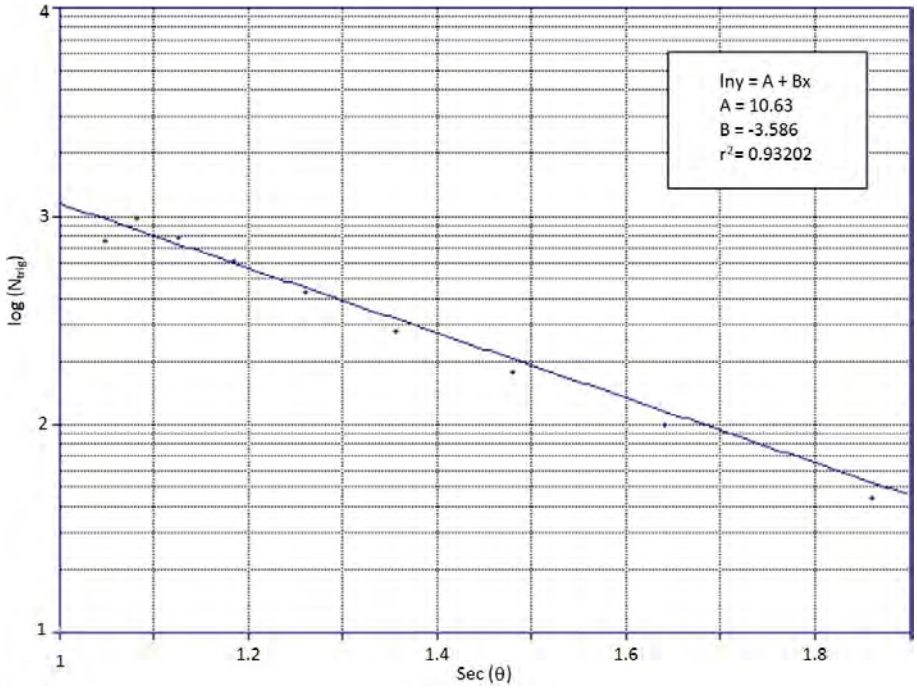

Figure 7: Mean number of N_{trig} vs. $\sec\theta$ of the events with $N_{trig} \geq 7$. The fitted curve is $N_{trig} = N_0 e^{-\tau_0 \sec\theta}$. It is similar to air mass effect on light intensity of stars, which is related to the atmosphere thickness.

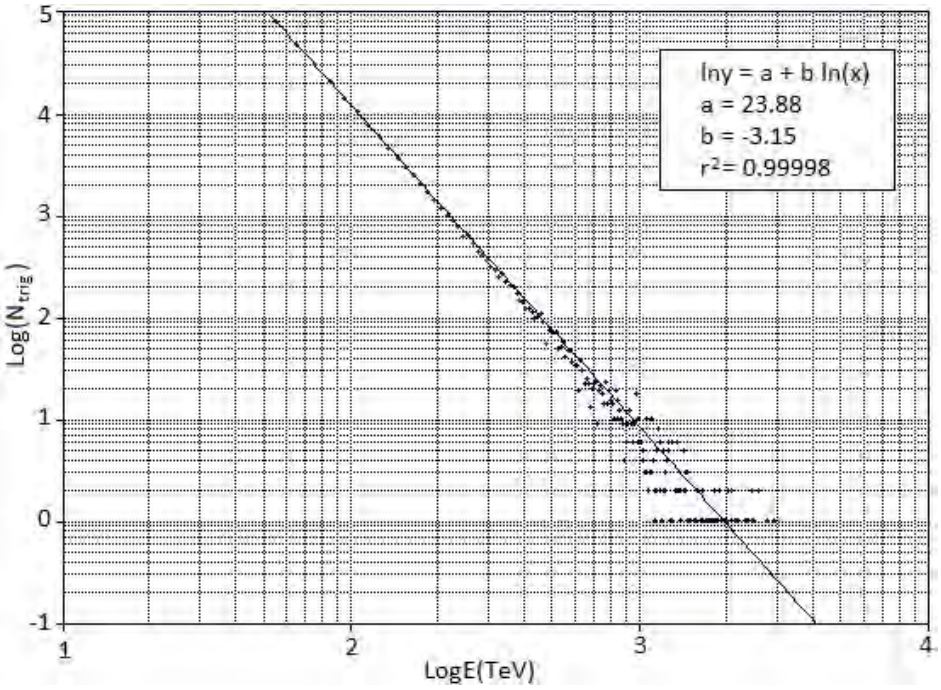

Figure 8: Number distribution of the null events with $N_{trig} = 0$ vs. energy of the simulated events.

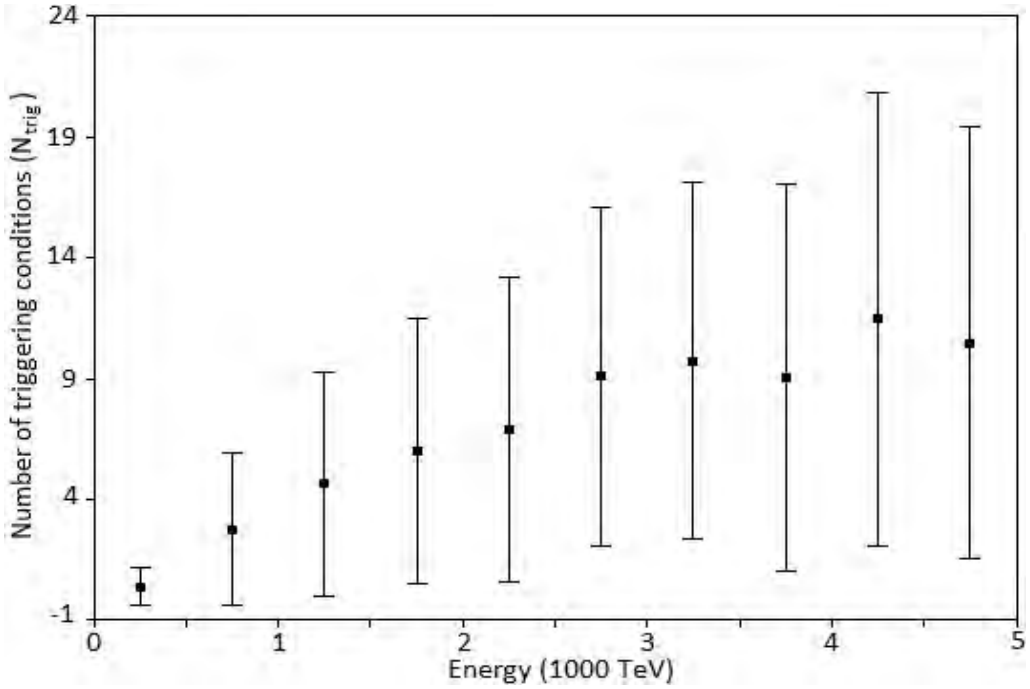

Figure 9: Mean and standard deviation ($\bar{N}_{trig} \pm \sigma_{N_{trig}}$) of the number of triggered cases vs. energy of all of the simulated events.

Acknowledgments

This research was supported by a grant from the national research console of Iran for basic sciences.
Thanks from Dr. M. Bahmanabadi for his helps in this work, and his constructive comments. I acknowledge prof. Paolo Bernardini from University of Lecce and ARGO-YBJ group for our very constructive private communications.

References

[1] A.A. Watson, *Extensive Air Showers and Ultra High Energy Cosmic Rays* (Summer school in Mexico, 2002).

[2] L.I. Dorman, *Cosmic rays in the earth's atmosphere and underground* (Cluwer Academic Publisher, 2004).

[3] T.K. Gaisser, *Cosmic Ray and particle Physics* (Cambridge University Press, 1990).

[4] K. Greisen Ann. Rev. Nuc. 10 (2005), 63.

[5] P. Sokolsky, *Introduction to Ultra High Energy Cosmic Ray Physics* (Adison-Wesley publishing company Inc, 1989)..

[6] M. Khakian Ghomi, M. Bahmanabadi, H. Hedayati Kh. IJAA, Vol.2, Issue 1 (2015), 97-107.

[7] A. Borione, M.L. Catanese, M.C. Chantel *et al.* ApJ 481 (1997), 313..

[8] F. Sheidaei, M. Bahmanabadi, M. Khakian Ghomi, F. Habibi, J. Samimi, Y. Pezeshkian and A. Anvari ICRC.5 (2009)909

[9] M. Bahmanabadi, A. Anvari, G. Rastegarzadeh, J. Samimi, and M. Lamehi Rachti, Experimental Astronomy 8/3 (1998), 211.

[10] M. Bahmanabadi, M. Khakian Ghomi and F. Sheydaei astropart. Phys. 24 (2005), 184.

[11] A. Marinelli, K. Sparks, R. Alfaro, M. Gonzlez, B. Patricelli, N. Fraija, NIMPA 742(2014), 216

[12] S. BenZvi, EPJ Web of Conferences, 105(2015), id.01003

[13] E. Fuente, T. Oceguera-Becerra, G. Garca-Torales, J. Garca-Luna, Springer-Verlag Berlin Heidelberg, 34(2013), 439

[14] F. Sheidaei, M. Bahmanabadi, M. Khakian Ghomi, et al., ICRC 5 (2008) 909.

[15] F. Sheidaei, PhD Thesis., Sharif University of Technology, Tehran, Iran.

[16] M. Khakian Ghomi, M. Bahmanabadi and J. Samimi, A&A 434 (2000), 459.

[17] F. Sheidaei, M. Bahmanabadi, and J. Samimi, Astroparticle Physics, Vol.33, Issue 5-6, 330 (2010).

[18] David A. Freedman, Statistical Models: Theory and Practice, Cambridge University Press (2005)

[19] M. Bahmanabadi, M. Khakian Ghomi, J. Samimi and D. Pourmohamma, Experimental Astronomy 15/1 (2003), 13.

[20] M. Bahmanabadi, A. Anvari, M. Khakian Ghomi, J. Samimi and M. Lamehi Rachti, Experimental Astronomy 13/1 (2004), 39.

[21] C. Grupen, *Astroparticle Physics* (Springer 2005).

[22] M. Bahmanabadi, F. Sheidaei, M. Khakian Ghomi and J. Samimi, Phys. Rev. D 74 (2006), 08.

[23] F. Sheidaei, M. Bahmanabadi, A. Keivani, M. Khakian Ghomi, A. Shadkam and J. Samimi, Phys. Rev. D 76 082002 (2007).

[24] D. Heck *et al.*, Report FZKA6019 (Forschungszentrum Karlsruhe) (1998).

[25] P.K.F. Greider, *Extensive Air Showers* (Springer 2010).

[26] K. Mitsui *et al.*, NIM A290 (1990), 565.

[27] M. Bahmanabadi, A. Anvari, M. Khakian Ghomi, *et al.*, Experimental Astronomy, 13(2002) 39.

[28] A. Chilingarian, G. Gharagyozyan, G. Hovsepyan and G. Karapetyan; Astroparticle Physics, Volume 25(2006), Issue 4, p. 269-276.

[29] T. Antoni et. al., Astroparticle Physics, 19(2003) 703.

[30] M. Ambrosio et. al., Astroparticle Physics, 11(1999) 437-450.

[31] Jochem D. Haverhoek, Ultra High Energy Cosmic Ray Extensive Air Shower simulations using CORSIKA, April 2006, Leiden University.

[32] M.T. Dova, L.N. Epele and A.G. Marazzi, Astropart. Phys. 18 (2003), 351.

[33] B.W. Caroll, D.A. Ostile, *An Introduction to Modern Astrophysics*, (Addison Wesley 2004).

IJAA

COPYRIGHT TRANSFER FORM

I confirm that the enclosed article entitled:

_____

_____

Corresponding Author

1) Has not previously been published, is not currently being considered or submitted elsewhere for publication, and, if accepted for publication in the above Journal, will not be published elsewhere in any language, without the consent of the editor and the publisher.

2) I acknowledge that it is a condition of acceptance by the editor that the publisher, Iranian Journal of Astronomy and Astrophysics acquires automatically the copyright in the manuscript throughout the world.

3) I confirm that I have obtained all the necessary permissions to include in the paper items such as quotations, figures, and the results of government sponsored research.

4) I enclose where necessary written permission of authors and publishers to use any copyright material (e.g. previously published figures and tables).

Corresponding Author

Signature: _____ Name: _____ Date:_____

Institution: _____ Dept: _____

Street: _____ City:_____ State: _____

Zip/code: _____ Country: _____Country Code:_____

Phone: _____ Fax: _____ Email: _____

IMPORTANT: Papers will not be published unless this form is signed by corresponding author (on behalf of all Authors) and return to the:

IJAA Editorial Office

Damghan University, Damghan, Iran

Iranian Journal of Astronomy and Astrophysics

Postal Code: 36716-41167

Tel-fax: +98-23-35220236

E-mail: ijaa@du.ac.ir

Instruction for Authors

Iranian Journal of Astronomy and Astrophysics peer reviewed international Journal published twice per year, devoted to the publication of original research papers from various field of astronomy and astrophysics. IJAA publishes quality original research papers, comprehensive review articles, short papers in astronomy and astrophysics and its applications in the broadest sense. It aims to disseminate knowledge; provide a learned reference in the field; and establish channels of communication between academic and research experts. Papers should contain results of original research, neither previously published nor under consideration for publication elsewhere. Papers presented at conference which, are only abstracted in the conference proceeding are also welcomed. There are no page charges except color figures. Contribution is open to researchers of all nationalities. All articles indexed and abstracted in (ISC) http://www.isc.gov.ir /

Articles will be published in the following categories:

Review Articles: (up to 25 template-based pages, including tables and figures) critically evaluate recent developments in a specific area of interest to the readership. They are normally invited; authors wishing to submit a review are requested to first contact chief editor.

Papers: (up to 12 template-based pages, including tables and figures) report original research which has not been previously published or submitted, and is not being considered for publication elsewhere. Papers are to be submitted to the Editor in Chief, who evaluates them with the aid of appropriate referees on the basis of scientific quality, originality, and general interest to the readership. The editor may also accept or reject inappropriate manuscripts without consulting referees.

Main Text

The manuscript should include Title, Abstract, Keywords, Introduction (opt.) Results and Discussion (opt.), Experimental (opt.), Acknowledgments (opt.), Conclusions (opt.) and References.

Abstract and Keyword

The abstract should briefly indicate the summary of results discussed in the paper. A list of 3-6 keywords must also be given in this page.

Manuscript Organization

For downloading the article template, please see our website:
http://ijaa.du.ac.ir/data/ijaa/news/sample-tex-IJAA-journals.zip

Copyright Transfer Agreement

Upon acceptance of an article, the corresponding author will be asked to transfer the signed copyright form (Available in http://ijaa.du.ac.ir/data/ijaa/news/sample-tex-IJAA-journals.zip) to the publisher on behalf of any and all co-authors. The authors must be warranted that are aware of and agree with all contents of the article and consent to their name appearing on it.

Open Access Policy

This journal provides immediate open access to its content on the principle that making research freely available to the public supports a greater global exchange of knowledge.

Online submission: http://journals.du.ac.ir/
E-mail: ijaa@du.ac.ir

CONTENTS